

NONLINEAR OPTICAL SPECTROSCOPY OF DIPOLE AND ELECTRON SPIN  
COHERENCES IN SEMICONDUCTOR NANOSTRUCTURES

by

PHEDON PALINGINIS

A DISSERTATION

Presented to the Department of Physics  
and the Graduate School of the University of Oregon  
in partial fulfillment of the requirements  
for the degree of  
Doctor of Philosophy

June 2004

“Nonlinear Optical Spectroscopy of Dipole and Electron Spin Coherences in Semiconductor Nanostructures,” a dissertation prepared by Phedon Palinginis in partial fulfillment of the requirements for the Doctor of Philosophy degree in the Department of Physics. This dissertation has been approved and accepted by:

---

Dr. Hailin Wang, Chair of the Examining Committee

---

Date

Committee in Charge:           Dr. Hailin Wang, Chair  
  Dr. Michael Raymer  
  Dr. Jens Nöckel  
  Dr. Heiner Linke  
  Dr. Mark Lonergan

Accepted by:

---

Dean of the Graduate School

An Abstract of the Dissertation of  
Phedon Palinginis for the degree of Doctor of Philosophy  
in the Department of Physics to be taken June 2004  
Title: NONLINEAR OPTICAL SPECTROSCOPY OF DIPOLE AND ELECTRON SPIN  
COHERENCES IN SEMICONDUCTOR NANOSTRUCTURES

Approved: \_\_\_\_\_  
Dr. Hailin Wang

In contrast to atomic systems, demonstrations of coherent optical phenomena associated with radiative and non-radiative coherences have remained elusive in semiconductor systems, due to inherent rapid decoherence and many-body effects. Recent studies, however, have raised the hopes for observations and applications of coherent optics in semiconductors, as ultralong dipole dephasing times in quantum dots (QDs), as well as a remarkable robustness of the electron spin coherence have been revealed.

In the first part of this dissertation, we present experimental studies of dipole dephasing in CdSe-QDs using a novel technique based on spectral hole burning. In contrast to previous studies, we are able to suppress effects of spectral diffusion, and therefore, to provide first time measurements of the intrinsic dipole dephasing rate. The dipole dephasing times measured exceed those of previous studies by over one order of magnitude. We thus find that despite significantly enhanced electron-phonon interactions, dipole dephasing times in II-VI based QDs can be as long as in III-V based QD-systems.

Based on the remarkable robustness of the electron spin coherence, we reveal in the second part of this dissertation nonlinear optical processes unique to extended optical excitations in semiconductors. Employing frequency- and time- domain pump-probe techniques, we find that signatures of electron spin coherence are absent in the third-order nonlinear optical response from QW-excitons subject to in-plane magnetic fields. This observation is unexpected based on considerations involving atom-like systems. Insight into our findings is gained by formally including many-body correlations in a phenomenological description of elementary optical excitations in QWs. We show that, although the electron spin coherence is created, effects thereof cancel in their respective contributions to one-exciton and two-exciton coherences. Furthermore, we reveal the emergence of quantum beats associated with electron spin coherence in an unusual fifth-order nonlinear optical process, an observation which can again be explained invoking higher-order correlations. In addition to providing fundamental insight into the role of many-body correlations on excitonic optical nonlinearities, our studies provide novel means for coherent optical control of electron spin coherence. The coherent Raman scattering study in particular presents a precursor for future observations of electromagnetically-induced-transparency (EIT) and slow-light applications based on electron spin coherence in semiconductors.

## CURRICULUM VITAE

NAME OF AUTHOR: Phedon Palinginis

PLACE OF BIRTH: Karlsruhe, Germany

DATE OF BIRTH: April 21, 1975

## GRADUATE AND UNDERGRADUATE SCHOOLS ATTENDED:

University of Oregon  
Univeristy Fridericiana of Karlsruhe  
Imperial College London

## DEGREES AWARDED:

Doctor of Philosophy in Physics, 2004, University of Oregon  
Diplom in Physics, 1999, University Fridericiana of Karlsruhe  
Imperial College International Diploma, 1997, Imperial College London

## AREAS OF SPECIAL INTEREST:

Linear and Nonlinear Optical Spectroscopy of Semiconductors  
Quantum Coherence and Quantum Interference in Semiconductor Nanostructures

## PROFESSIONAL EXPERIENCE:

Research Assistant, Hailin Wang Laboratory, Department of Physics, University of Oregon, 1998-present

Teaching Assistant, Department of Physics, University of Oregon, 1998

Intern, Fraunhofer Institute Systems and Innovation Research, 1997-1998

## GRANTS, AWARDS AND HONORS:

Fellowship of the DAAD - German Academic Exchange Service, University of Oregon, 2000/01

Ph.D. prize for highest score on Ph.D. qualifier exam, University of Oregon, 1999

Travel Grant Award from the Division of Laser Science of the American Physical Society, 2002

Travel Grant Award from the Division of Laser Science of the American Physical Society, 2003

#### PUBLICATIONS:

Xudong Fan, Phedon Palinginis, Scott Lacey, Hailin Wang, and Mark C. Lonergan, "Coupling semiconductor nanocrystals to a fused silica microsphere: a quantum dot microcavity with extremely high Q-factors," *Opt. Lett.* **25**, 1600 (2000).

Phedon Palinginis and Hailin Wang, "High-resolution spectral hole burning in CdSe/ZnS core/shell nanocrystals," *Appl. Phys. Lett.* **78**, 1541 (2001).

Phedon Palinginis, Sasha Tavenner, Mark C. Lonergan, and Hailin Wang, "Spectral hole burning and zero phonon linewidth in semiconductor nanocrystals," *Phys. Rev. B* **67**, 201307 (R) (2003).

Phedon Palinginis and Hailin Wang, "Vanishing and Emerging of Absorption Quantum Beats from Electron Spin Coherence in GaAs Quantum Wells," *Phys. Rev. Lett.* **92**, 37402 (2004).

Phedon Palinginis and Hailin Wang, "Coherent Raman scattering from electron spin coherence in GaAs quantum wells", *J. Magn. Magn. Mater.*, in press

Shu-Wei Chang, Shun-Lien Chang, Pei-Cheng Ku, Connie J. Chang Hasnain, Phedon Palinginis, and Hailin Wang, "Slow-Light Using Excitonic Population Pulsation", *Phys. Rev. B*, second review.

Phedon Palinginis, Hailin Wang, Serguei V. Goupalov, David S. Citrin, Malgorzata Dobrowolska, Jacek. K. Furdyna, "Exciton dephasing in self-assembled CdSe quantum dots", *Phys. Rev. B*, Rapid Communication, first review.

Phedon Palinginis and Hailin Wang, "Coherent Raman resonance from electron spin coherence in GaAs quantum wells", *Phys. Rev. B*, Rapid Communication, first review.

Pei-Cheng Ku, Forrest Sedgwick, Connie J. Chang Hasnain, Phedon Palinginis, Tao Li, Hailin Wang, Shu-Wei Chang and Shun-Lien Chang, "Slow-Light in Semiconductor Quantum Wells", submitted to *Optics Letters*.

## ACKNOWLEDGMENTS

First and foremost, I would like to thank my advisor Professor Hailin Wang for his guidance over the last couple of years. His enthusiasm, endurance and excitement for physics supported me throughout my time as a doctoral student and will remain exemplary to me. Given his extensive knowledge and scientific expertise, it was a privilege to grow as an experimental physicist under his supervision. My gratitude extends to the members of my doctoral committee: Professor Michael Raymer, Heiner Linke, Jens Nöckel and Mark Lonergan. Going back to my days as a masters student in Germany, I would like to acknowledge Professor Claus Klingshirn, who introduced me to the world of physics at the University of Karlsruhe. I thank Dr. Serguei Goupalov for his close collaboration on my work on dipole dephasing in quantum dots. I also thank Dr. David Alavi, Bernie Wendring and Stephen Predko, who provided excellent technical support.

My stay in Wang Lab would have been only half as much fun if it wasn't for my lab-mates: Xudong Fan, Mark Phillips, Scott Lacey, Sasha Tavenner Krüger, Susanta Sarkar, Yumin Shen and Tao Li. They all made me appreciate the importance of a warm, friendly, supportive yet work-intensive environment. Not to forget the friendly and skilled office staff of the physics department: Janine O'Guinn, Bonnie Grimm, Colleen McKillip, Sandee Thompson, Jani Calivan, Mary Crafts and Jennifer Lewis for always being available.

As there is a life after physics, I would like to acknowledge those who spent this part of my life with me during my stay at the University of Oregon. My brother and friend Kimon, who gave me the idea to come to Oregon. Karl Saunders for many good laughs. Yoram Lubianiker for being a great friend and mentor. Amy Krewedl and her family for a warm welcome to the U.S.. Andy Funk for teaching me how to light charcoals without lighter fluid and for sharing the life of

a physics graduate student. Many thanks to the Eurotrash soccer team, in particular Frank “the tank” Nakatsuma, Nik “Berlin Wall” Klakow, Conor Byrne, Mike Fink and Dave Walker.

My heartfelt appreciation goes also to the “brazilian community” of Eugene, in particular Andrea Meyer Landulpho Medrado, for making the sun shine during long Eugene winters.

Lastly, my respect for my parents for holding out for so long.

## TABLE OF CONTENTS

Chapter	Page
I. INTRODUCTION .....	1
Motivation .....	1
Background .....	3
Objective and Outline .....	9
II. BAND-EDGE EXCITONS IN SEMICONDUCTOR NANOSTRUCTURES .....	14
Electronic bandstructure in zinc-blende- and wurtzite- type semiconductors .....	15
Wannier Excitons .....	19
Effects of confinement on single particle states .....	23
Degrees of confinement and the strong confinement regime .....	27
Band-edge excitons in GaAs quantum wells .....	28
Band-edge excitons in CdSe quantum dots .....	30
Summary .....	33
III. EXCITON LOCALIZATION, COULOMB CORRELATIONS AND IN-PLANE MAGNETIC FIELDS IN QUANTUM WELLS .....	35
Interface disorder and exciton localization in GaAs quantum wells .....	35
Nonlinear optical response from excitons: the role of Coulomb correlations .....	37
Quantum wells in Voigt geometry .....	41
Summary .....	44
IV. ELECTRON-PHONON INTERACTIONS AND DIPOLE DEPHASING IN SEMICONDUCTOR QUANTUM DOTS .....	45
Energy relaxation: the role of dark excitons .....	46
Electron-phonon interactions in quantum dots .....	47
Spectral diffusion in quantum dots .....	58
Summary .....	60
V. SAMPLE DESCRIPTION AND EXPERIMENTAL PROCEDURES .....	61
Core/shell CdSe/ZnS nanocrystals .....	61
Self-assembled CdSe/ZnSe quantum dots .....	63
GaAs/Al <sub>x</sub> Ga <sub>1-x</sub> As quantum wells .....	64
High-resolution frequency-domain spectral hole burning .....	65
Coherent Raman scattering .....	72
Quantum beat experiment .....	75
Notes on low-temperature measurements .....	77

Chapter	Page
VI. DIPOLE DEPHASING IN CdSe-NANOCRYSTALS .....	78
Zero-optical-phonon line (ZOPL) and LO-phonon sidebands .....	78
Zero-phonon-line (ZPL) and confined acoustic-phonon sidebands .....	84
Dipole dephasing and spectral diffusion of the ZPL .....	87
Lifetime of the SHB-response .....	91
Summary .....	95
VII. DIPOLE DEPHASING IN SELF-ASSEMBLED CdSe-QUANTUM DOTS .....	96
Zero-optical-phonon line (ZOPL) and LO-phonon sidebands .....	96
Dipole dephasing and spectral diffusion of the ZPL .....	99
Summary .....	105
VIII. COHERENT RAMAN SCATTERING FROM ELECTRON SPIN COHERENCE IN GaAs-QUANTUM WELLS .....	107
Coherent Raman scattering from localized excitons .....	108
Coherent Raman scattering from mobile excitons .....	115
Summary .....	118
IX. QUANTUM BEATS FROM ELECTRON SPIN COHERENCE IN GaAs-QUANTUM WELLS .....	120
Quantum beats from localized excitons .....	120
Quantum beats from mobile excitons .....	123
Polarization dependence .....	128
Summary .....	130
X. SUMMARY AND FUTURE WORK .....	131
Summary .....	131
Future Work .....	133
BIBLIOGRAPHY .....	136

## LIST OF FIGURES

Figure	Page
1. Generic two- and three- level systems .....	3
2. Two factors complicating measurements of the homogeneous linewidth in quantum dots ..	6
3. Schematic of a QW and the energy level structure of the heavy-hole exciton .....	9
4. Generic bandstructure for zinc-blende type semiconductors .....	18
5. Electron/hole dispersion in the single-particle picture .....	21
6. Energy dispersion and corresponding joint DOS .....	24
7. Schematic of GaAs/Al <sub>x</sub> Ga <sub>1-x</sub> As QW-structure / core/shell CdSe/ZnS nanocrystal .....	26
8. In-plane dispersion of the $n_z^e = n_z^h = 1$ subbands in a QW .....	29
9. Effects of SX and LX part of the exchange interaction .....	32
10. Generic level structure of the band-edge exciton ( $1S_{h,3/2} 1S_e$ ) in CdSe nanocrystals .....	33
11. Level structure of the HH1-exciton .....	40
12. Effects of in-plane magnetic fields on the HH1-exciton level structure .....	42
13. Effects of in-plane magnetic fields on excitonic absorption spectrum .....	43
14. Generic phonon dispersion in a polar diatomic crystal .....	48
15. Size dependence for the first three ‘spheroidal’ ( $l = 0$ ) and ‘ellipsoidal’ ( $l = 1$ ) confined acoustic phonon modes in a CdSe nanosphere and for free-boundary conditions .....	50
16. Illustration of the effects of electron-phonon interactions .....	56
17. Effects of spectral diffusion .....	59
18. ‘Bare’ CdSe nanocrystals. Core/shell CdSe/ZnS nanocrystals .....	61
19. RT-PL spectra .....	62
20. Schematic of the sample structure for MBE grown self-assembled CdSe/ZnSe QDs .....	64
21. Absorption spectra of the QW-samples .....	65
22. Principle of SHB .....	66
23. Experimental setup for degenerate/non-degenerate pump-probe measurements .....	70
24. Schematic for three-beam FWM .....	72
25. Scenario used to illustrate coherent Raman scattering from a V-type three-level system ..	73
26. Experimental setup for quantum beat measurements .....	76
27. PL/nonlinear absorption spectrum from sample NC1 at $T = 10$ K .....	79
28. SHB-spectra from sample NC1 .....	80
29. SHB-spectrum from sample NC4 .....	82

30. Temperature dependence of the SHB-response .....	84
31. Fine structure of the ZOPL.....	85
32. Temperature dependence of the ZOPL .....	86
33. ZOPL from sample NC1 (T = 2 K) at various modulation frequencies.....	87
34. Modulation frequency dependence of the ZPL-linewidth.....	88
35. Pump-intensity dependence of the ZPL-linewidth .....	89
36. Coherent contribution to the three-beam FWM-response .....	92
37. Energy level diagram to model the bright exciton and possible effects of dark states .....	93
38. PL/nonlinear absorption.....	97
39. SHB-response .....	98
40. Temperature dependence of the ZOPL .....	99
41. Modulation frequency dependence of the ZOPL.....	100
42. Modulation frequency dependence of the ZPL.....	101
43. Temperature dependence of the ZPL .....	102
44. Calculated linear absorption spectrum for a single CdSe-QD.....	104
45. Linear absorption from sample QW1.....	107
46. SHB-response from localized HH1-excitons.....	108
47. Coherent Raman scattering from localized excitons .....	109
48. Third-order numerical solution of the OBE.....	111
49. Polarization dependence of the coherent Raman scattering response.....	113
50. Effects of excitation level on coherent Raman scattering.....	114
51. Coherent Raman scattering from mobile excitons.....	115
52. Energy-level structure of the HH1-exciton in Voigt geometry .....	117
53. Time-integrated normalized differential transmission.....	121
54. Probe intensity dependence .....	122
55. Time-integrated normalized differential transmission.....	123
56. Level structure of the HH1-exciton in Voigt geometry .....	124
57. Probe intensity dependence .....	127
58. Polarization dependence .....	129

## LIST OF TABLES

Table	Page
1. Selection of physical parameters for GaAs and CdSe .....	19

## CHAPTER I

### INTRODUCTION

#### Motivation

Spurred by the advancements made in nonlinear optical spectroscopy, the last decade has witnessed significant progress in the field of coherent optical control. Coherent control denotes the ability to manipulate the coherent evolution of a quantum mechanical system and is currently of great interest because of its potential to provide alternatives to conventional device physics by exploiting quantum coherence as the operating principle in novel optical or electronic devices. The field of quantum information in particular has benefited from, but also spurred research in coherent control. Potential applications based on coherent control are facing significant technological hurdles, which are inherently tied to decoherence<sup>1</sup>. Dephasing or decoherence denotes the loss of quantum coherence over time, and arises from inevitable coupling of quantum systems to their environment. In the context of coherent control, two time scales are of interest<sup>1,2</sup>. First, the decoherence, or dephasing time itself, i.e. the time window within which a quantum system evolves coherently. Second, the switching time, i.e. the time it takes to carry out a coherent operation on that quantum system. The mantra for practical implementations of coherent control is to maximize the ratio between decoherence and switching time, or equivalently, the number of operations, which can be carried out before the quantum system decoheres. Generally, decoherence- and switching- time are determined by fundamental properties of the quantum system and the type of energy exchange mechanism chosen to enable coherent control. The wide array of proposed quantum logic schemes reflects the spectrum of current efforts to technically overcome the limitations set by decoherence.

Within the framework of so called hybrid optical/solid-state approaches, several quantum logic schemes based on coherent optical control of elementary excitations in semiconductor systems have been proposed. These schemes draw in particular from recent observations of ultralong decoherence times associated with dipole coherences in quantum dot (QD) systems<sup>3,4</sup> and electron spin coherence in various semiconductor systems<sup>5</sup>. The robustness of these types of coherences is quite remarkable and unprecedented in semiconductors. Analogous to the classical bit, which is generally encoded in a two-state system (e.g. high/low voltage), the units of information in quantum information, the ‘qubits’, are generally encoded in quantum mechanical two-level systems. Practical implementations of qubits require therefore physical systems featuring a discrete energy level structure, two levels of which constitute a qubit. In addition, the coherence associated with that two-level system should be robust to allow for manipulation. As a result of their discrete energy level structure, QDs, similar to atoms, effectively represent two-level systems in the context of resonant interaction with optical fields. Thus, dipole transitions in QDs can be potentially used to encode qubits, whereas coherent control of these qubits can be enabled via resonant optical fields. Similarly, electron spin, which inherently constitutes a quantum mechanical two-level system is also a potential candidate for implementations of qubits. In contrast to dipole coherences, however, the electron spin coherence presents a non-radiative or Raman coherence.

In the next section we review general aspects associated with dipole coherences in QDs and electron spin coherence in semiconductor systems. To study their fundamental properties as well as their potential use in applications of coherent optical control, both of these coherences have been carefully investigated in this dissertation using techniques based on nonlinear optical spectroscopy.

### Background

In the following, we introduce the concepts relevant for a discussion of the relaxation dynamics of optical excitations by means of a resonantly excited two-level system. A phenomenological model describing the relaxation dynamics of a collection of two-level systems was first introduced by Bloch in the context of magnetic resonance of spin-1/2 particles<sup>6</sup>, and was later applied to resonant dipole optical interaction of electromagnetic fields with atoms (Optical Bloch Equations (OBE))<sup>7</sup>.

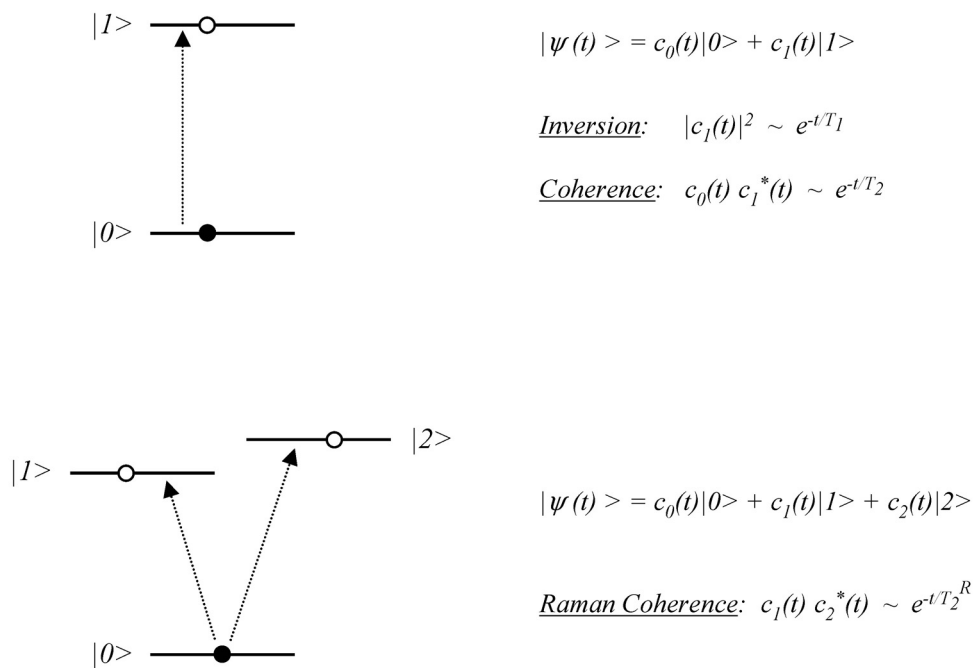


FIGURE 1. Generic two- and three- level systems. The arrows indicate dipole allowed optical transitions. Resonant optical interaction can generate a dipole coherence in the two-level system. The coupling of the two upper states to a common ground state in the three-level system allows for optical control of the non-radiative coherence between states  $|I\rangle$  and  $|2\rangle$ .

Two observables characterize the evolution and hence the relaxation dynamics of a quantum mechanical two-level system: 1. the population imbalance, i.e. the difference between the upper and the lower state population (inversion) and 2. the phase relationship or coherence between the two states. Generally, the two-level system is in a linear superposition state with a finite inversion and coherence. Once excited, the upper state population decays eventually due to coupling of the two-level system to one or more reservoirs (radiation field, lattice vibrations etc.). Assuming a single exponential decay, this energy or population relaxation is characterized by the longitudinal decay time  $T_1$  or population relaxation time. Likewise, coherence between the two states is lost according to the transversal decay time  $T_2$  or dephasing time. Energy relaxation leads necessarily to dephasing. In addition, pure dephasing processes (i.e. elastic processes) can contribute to the loss of phase coherence without affecting the population imbalance. The population relaxation time presents therefore an upper limit for the dephasing time, which is maximized in the lifetime limit characterized by the absence of pure dephasing ( $T_2 = 2T_1$ ). Applied successfully to atomic systems, the concepts of energy relaxation and pure dephasing are also being used to describe the more complex relaxation dynamics of optical excitations in semiconductors. Note that in the context of coherent control,  $T_2$  is the time scale of interest, since it sets the time window within which coherence is preserved. For a statistical description of an ensemble of quantum mechanical systems relaxation dynamics are typically discussed within a density matrix formalism.

In addition to their discrete electronic energy level structure, QDs exhibit characteristics such as photon anti-bunching, which are typically associated with atomic systems. One question, which has attracted particular interest in recent years is whether excitonic dipole transitions in QDs exhibit similarly narrow homogeneous linewidths, or equivalently, similarly long dipole dephasing times as dipole optical transitions in atoms. Although commonly referred to as

‘artificial atoms’ due to their discrete energy level structure, note that QDs are made up of a few thousand atoms and represent thus a condensed matter system in which electrons can couple to the lattice vibrational modes of the crystal. Just as in bulk, electron-phonon interactions can therefore significantly contribute to dipole dephasing in QDs. In contrast to the bulk, however, electron-hole pairs are strongly localized in QDs, a situation which is likened to impurity centers in doped crystals<sup>8</sup>. In addition to confinement induced modifications of the electron- and phonon-density of states (DOS), localization of electrons and holes leads to strong modifications of electron/hole-phonon interactions in QDs. While providing ideal laboratory systems to study the effects of confinement on electron-phonon interactions in zero-dimensional systems, QDs, potentially featuring long-lived dipole coherences, are highly attractive for applications of coherent optical control.

Generally, two factors complicate measurements of dipole dephasing, or equivalently the homogeneous linewidth in QDs: inhomogeneous broadening, which is present in virtually all QD-systems, and spectral diffusion, which has been observed in a wide variety of QD-systems. Inhomogeneous broadening results from static non-uniformities of e.g. dot size, dot shape, alloy composition or strain, all of which affect the electronic confinement energy. In a measurement of the homogeneous linewidth, effects of inhomogeneous broadening have to be eliminated experimentally. Therefore, previous studies have resorted to single-dot measurements such as single-dot photoluminescence (PL), or site selective measurements based on nonlinear optical techniques such as spectral hole burning (SHB), photon echo, accumulated photon echo or transient four-wave-mixing carried out on ensembles of QDs. In addition to inhomogeneous broadening, QDs exhibit characteristically high surface to volume ratios, which inevitably expose QDs to surface-related effects and effects of the surrounding matrix. One phenomenon in particular, spectral diffusion, is exemplary in demonstrating the sensitivity of QDs to dynamic

variations in their surroundings. Spectral diffusion, also known from molecular systems, denotes fluctuations of the transition energy of an optical transition due to fluctuations in the local environment of the dipole emitter. Note that in the presence of spectral diffusion, measured linewidths of the optical transition of interest become dependent on the measurement time scale as shown in Figure 2. Effects of spectral diffusion can thus mask the *intrinsic* linewidth in measurements of the homogeneous linewidth.

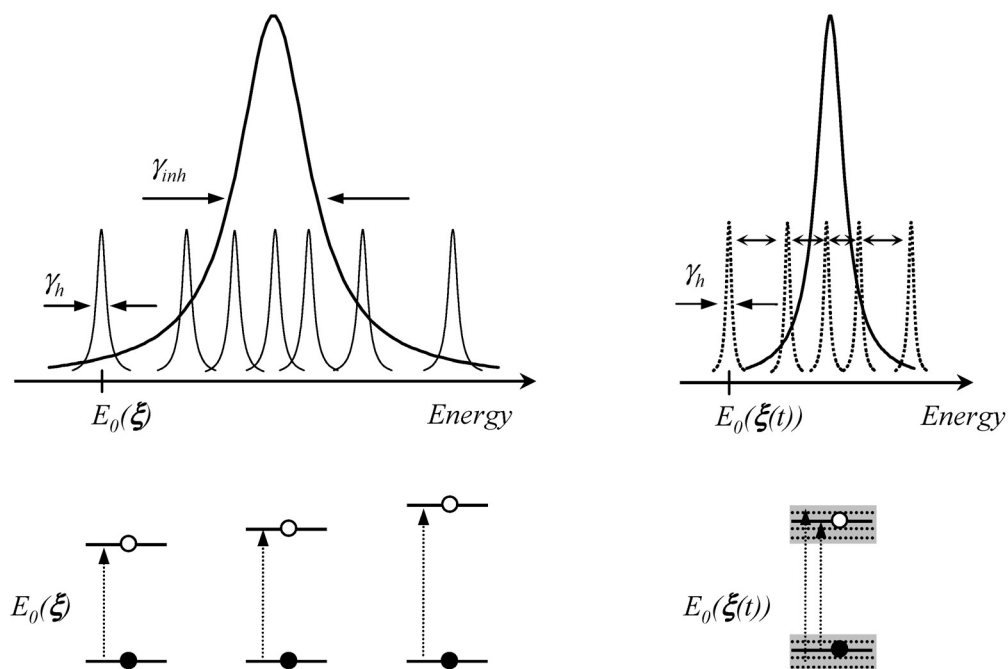


**FIGURE 2.** Two factors complicating measurements of the homogeneous linewidth in QDs. Inhomogeneous broadening, which is illustrated on the left is due to static non-uniformities ( $\xi$ ). Spectral diffusion, effects of which are illustrated on the right, arises from dynamic variations in the dot environment ( $\xi(t)$ ). The ‘instantaneous’ spectrum indicated by the dotted lines exhibit ‘spectral jitter’. The time average is shown by the solid curve.

In this dissertation, we investigate two types of QD-systems: colloidal CdSe-nanocrystals grown by high-temperature organometallic synthesis, and epitaxially grown self-assembled CdSe-QDs. In both cases, we are interested in dephasing of the first bright exciton. Using single-dot PL<sup>9</sup> and accumulated photon echo<sup>10</sup>, recent measurements on dipole dephasing in CdSe-nanocrystals have revealed homogeneous linewidths exceeding 100  $\mu\text{eV}$ . Note, that due to the long integration times used in these measurements, effects of spectral diffusion are potentially masking the intrinsic homogeneous linewidth. The dephasing times inferred from these measurements ( $\sim 10$  ps) present thus only a lower limit to the *intrinsic* dipole dephasing time. Note furthermore, that linewidths obtained from the single-dot PL study are resolution limited. Similarly, resolution limited linewidths on the order of 70  $\mu\text{eV}$  have been measured in self-assembled CdSe-QDs<sup>11</sup>. In contrast, ultralong dephasing times on the order of several hundred picoseconds have been revealed in III-V based QD systems<sup>3,4</sup>. The obvious discrepancy raises the question whether dot intrinsic properties, such as stronger polar interaction in II-VI materials, do in fact enhance dipole dephasing in II-VI based QD-systems, or whether deficiencies in the experimental techniques employed have been preventing measurements of the intrinsic homogeneous linewidth in II-VI based QD-systems.

Leading up to a general discussion of electron spin coherence in semiconductors, note first of all that in contrast to the hole- and exciton- spin, which exhibit decoherence times on the order of picoseconds, electron spin decoherence times are on the order of the recombination time and thus on the order of nanoseconds<sup>12</sup>. Electron spin decoherence times reaching up to 100 ns have been observed in n-doped systems<sup>13</sup>. The exceptional robustness of the electron spin coherence results from the fact that the electron spin, in contrast to the hole spin, is largely decoupled from the orbital degrees of freedom as spin-orbit coupling is weak for conduction band (CB) electrons in

most zinc-blende type semiconductors<sup>14</sup>. The electron spin coherence is a non-radiative coherence and as such can not be optically excited directly. The key to optically address spin coherences in semiconductors is by means of optical selection rules in conjunction with externally applied magnetic fields to generate appropriate modifications of the energy level structure<sup>15</sup>. Semiconductor quantum wells (QWs) are particularly well-suited in this regard, since the valence band (VB) degeneracy is lifted by the one-dimensional confinement. Furthermore, the growth direction defines a preferred axis in QW-systems. Modifications of the energy-level structure by applying external magnetic fields depend therefore on the orientation of the magnetic field with respect to the growth direction, allowing the study of different kinds of spin coherences. To probe exciton spin coherences in QWs, an external magnetic field is applied along the growth direction. In contrast, to probe electron spin coherence, a magnetic field is applied in the plane of the QW. In this case, the bandstructure is modified such that both CB-electrons are optically coupled to the same VB state. As a result, the non-radiative electron spin coherence between the two CB states can be induced optically in a V-type energy level scheme as shown in Figure 3.

So far, optical studies of electron spin coherence have been carried out using time-resolved PL and time-resolved Faraday pump-probe spectroscopy. Both techniques provide the necessary means to optically measure electron spin coherence in semiconductors, i.e. initially preparing the spin system optically, then interrogating its evolution either using appropriate detection schemes (PL) or a weak probe field which is sensitive to the orientation of the electron spin (Faraday spectroscopy). Although powerful for a variety of measurements, neither technique could yet provide fundamental insight into many-body correlations underlying the coherent optical response from electron spin coherence. In this dissertation, we expand the means of coherent optical control of electron spin coherence by employing, for the first time, coherent Raman

scattering and time-domain pump-probe spectroscopy to study signatures of electron spin coherence and associated many-body effects thereof in the nonlinear optical response.

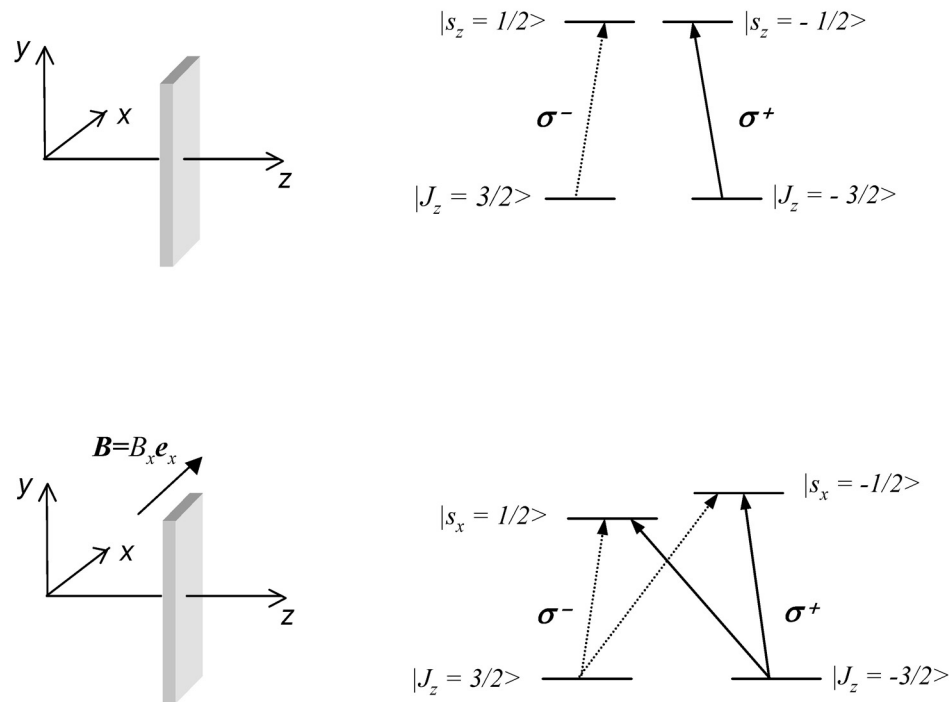


**FIGURE 3.** Top: Schematic of a QW and the energy level structure of the heavy-hole exciton. Bottom: Effects of in-plane magnetic fields on the energy level structure. Two V-type systems result suitable for optical control of the non-radiative electron spin coherence..

### Objective and Outline

We present in this dissertation a careful study of dipole dephasing in CdSe-QDs and manifestations of electron spin coherence in GaAs-QWs using techniques based on nonlinear optical spectroscopy. While elucidating fundamental aspects of collective excitations in many-

body systems, such as electron-phonon interactions in QDs or the role of higher order Coulomb correlations in QWs, the studies provide novel means to optically control dipole and electron spin coherences in semiconductor systems. The work presented constitutes thus another stepping stone towards coherent optical control in semiconductor systems, and more specifically, implementations of hybrid optical/solid-state quantum logic schemes. As many of these schemes are based on cavity-QED effects, the work at hand is also of interest for demonstrations of cavity-QED related phenomena in semiconductor systems. While successfully observed in atomic systems, cavity-QED effects have remained elusive in semiconductor systems mainly due to rapid decoherence and many-body effects inherent in semiconductors. Similarly, while well established for atomic systems, studies of coherent optical phenomena associated with non-radiative coherences, such as electromagnetically-induced-transparency (EIT) and related effects thereof<sup>16</sup> remain to be investigated in semiconductor systems. Very recently, EIT has been observed in semiconductor QWs by exploiting higher-order excitonic coherences<sup>17,18</sup>. While proving extremely useful to probe the nonlinear optical response from extended optical excitations in semiconductors, rapid decoherence in these semiconductor based EIT-schemes prevents their use for practical applications. Tremendous interest exists currently to harvest slow-light in semiconductors for implementations of optical buffers, which present the last missing piece in the realization of all-optical networks<sup>19</sup>. Among the multitude of EIT-related effects, slow-light results from a steep dispersion, which typically accompanies EIT. The nonlinear optical studies on electron spin coherence deserve thus particular attention, since the robustness of the electron spin coherence could allow for extremely narrow transparency windows and thus for feasible slow-light applications based on electron spin coherence in semiconductors. Clearly, solid-state systems are much preferred over atomic systems because of their low-cost and the possibility of integration with currently existing technologies.

The first part of the dissertation presents our studies on the homogeneous linewidth in high-quality colloidal CdSe/ZnS core/shell nanocrystals grown by high-temperature organometallic synthesis and self-assembled CdSe/ZnSe QDs grown by molecular-beam-epitaxy (MBE). Having developed a novel spectroscopic technique based on frequency-domain SHB, we are able to probe with high spectral resolution the dynamics of spectral diffusion, effects of which are observed in both systems, and to measure the relaxation dynamics of the SHB-response. In contrast to previous studies, we are able to suppress effects of spectral diffusion experimentally. We are thus capable of providing first time measurements of the intrinsic homogeneous linewidth in CdSe-nanocrystals and CdSe-QDs. Exceeding previously measured values by over one order of magnitude, we reveal dephasing times of  $T_2 \sim 200$  ps for the zero-phonon-transition CdSe-nanocrystals<sup>20</sup>. In addition to the zero-phonon-line (ZPL) associated with the zero-phonon-transition, the SHB-response from CdSe-nanocrystals reveals directly in the frequency domain acoustic-phonon- as well as longitudinal-optic (LO) phonon- assisted transitions. The SHB-response provides thus crucial insight into electron-phonon interactions underlying dipole dephasing in CdSe-nanocrystals. The features observed in the SHB-response from self-assembled CdSe-QDs are similar to those obtained for CdSe-nanocrystals. The zero-phonon-transition and phonon-assisted optical transitions are observed. As for CdSe-nanocrystals, measured dephasing times of the zero-phonon-transition are on the order of  $T_2 = 200$  ps<sup>21</sup>, again demonstrating that previous single-dot PL studies are inept for homogeneous linewidth measurements of the QD-systems considered here. Effects of the dot environment manifest in the experimentally observed acoustic phonon assisted transitions. Whereas effects of acoustic-phonon confinement are observed for ‘free-standing’ colloidal CdSe-nanocrystals in the form of discrete acoustic phonon sidebands<sup>22</sup>, self-assembled CdSe-QDs exhibit a continuum of acoustic-phonon modes. The good agreement between the dipole dephasing times in both QD-systems demonstrates that dephasing

of the purely electronic transition is unaffected by the details associated with the DOS of acoustic-phonon modes as well as the fine structure of the band-edge exciton. Comparison with III-V based QD-systems reveals that despite significantly enhanced coupling to acoustic-phonons, dephasing times in CdSe-QDs are on the same order as the ultralong dipole dephasing times observed in InGaAs-QDs. Our results stimulate thus further theoretical studies on the role of electron-phonon interactions on dephasing of the zero-phonon-transition.

Two complementary measurement techniques, time-domain pump-probe spectroscopy and frequency-domain coherent Raman scattering were employed to study manifestations of the electron spin coherence in the nonlinear optical response from GaAs-QWs subject to in-plane magnetic fields. Both experiments reveal that effects of exciton localization, well known to occur in GaAs-QW-systems, greatly influence the nonlinear optical response associated with electron spin coherence. While coherent Raman sidebands as well as quantum beats associated with electron spin coherence emerge for localized excitons in the respective measurements, neither feature is present in the third order nonlinear optical response from mobile excitons<sup>23,24</sup>. A qualitative analysis based on N-exciton eigenstates<sup>25</sup> illustrates how exciton-exciton interactions, especially the absence of these interactions, profoundly affect the manifestation of electron spin coherence in the coherent nonlinear optical response. We argue that as a result of strong on-site Coulomb repulsion, strongly localized excitons in a QW behave essentially like atomic systems, since formation of higher-order correlations, i.e. two-exciton states is prohibited. In contrast, the involvement of higher-order correlations leads to a cancellation of the effects associated with electron spin coherence in the third order nonlinear optical response from mobile excitons. Although the electron spin coherence is created optically, signatures thereof are absent in the third order nonlinear optical response from these extended optical excitations. We further show,

that in order to observe electron spin coherence associated with mobile excitons, strongly interacting two-exciton states need to be involved in the nonlinear optical process. The experimental results confirm this expectation as quantum beats from the electron spin coherence associated with mobile excitons emerge in an unusual fifth-order nonlinearity. In a comparison between the frequency- and time- domain measurement, we point out how the nonlinear mechanism generating the electron spin coherence differs fundamentally for the two measurements. While the electron spin coherence is created to second order in the pump field alone in the time-domain measurement, joint action of pump and probe is required to generate electron spin coherence in the frequency-domain measurement. The different nonlinear mechanisms involved give rise to distinctively different polarization selection rules in the time-domain and the frequency domain pump-probe measurements respectively.

The dissertation is organized as follows. Chapter II reviews band-edge excitons in GaAs-QWs, colloidal and self-assembled CdSe QDs. Chapter III reviews the effects of interface fluctuations on exciton localization and exciton relaxation in GaAs-QWs. A phenomenological approach based on N-exciton eigenstates is introduced for a discussion of excitonic optical nonlinearities. A description of the heavy-hole exciton level structure for GaAs-QWs in Voigt geometry is also provided. Effects of confinement on electron-phonon interactions and dipole dephasing in QDs are discussed in chapter IV within the framework of the independent Boson model. Effects of spectral diffusion are also considered. The experimental techniques used in the nonlinear optical studies are explained in Chapter V. Chapter VI/VII present the results of the SHB-study on dipole dephasing in colloidal/self-assembled CdSe QDs. Chapters VIII and IX present the results of the coherent Raman scattering and the quantum beat experiment on electron spin coherence in GaAs-QWs respectively. The dissertation closes with a summary.

## CHAPTER II

## BAND-EDGE EXCITONS IN SEMICONDUCTOR NANOSTRUCTURES

This chapter provides a general discussion of band-edge excitons in low-dimensional semiconductor systems. Band-edge excitons constitute the elementary optical excitations near the fundamental band-gap of semiconductor nanostructures and are central to the work presented here as they host the coherences of interest. Given the complexity of band-edge exciton fine structure calculations, the review presented here is only qualitative. The discussion on band-edge excitons in GaAs-QWs, CdSe-nanocrystals and self-assembled CdSe-QDs is based on references 26, 27 and 28 respectively. For a general discussion of exciton fine structures in QDs, the reader is referred to 29.

The electronic level structure in low-dimensional semiconductor systems is determined by the joint effects of crystal potential, confinement potential and Coulomb interaction. Their respective contributions are introduced here by successive approximation. Starting point is a review of the bulk bandstructure in GaAs and CdSe within the effective mass approximation (EMA), appropriate for a discussion of optical excitations near the band-edge. Subsequent treatment of confinement as well as many-body effects mediated via Coulomb interaction is greatly simplified within the EMA. Note that a unified mathematical treatment of confinement and many-body effects presents a challenging theoretical problem. The combined effect of crystal potential, confinement potential, and Coulomb interaction are therefore discussed qualitatively for each nanostructure of interest. The Coulomb interaction between electrons plays a particularly important role in determining the fine structure of band-edge excitons in low-dimensional semiconductor systems. In a quantum mechanical description of interacting electrons, the

Coulomb potential gives rise to direct Coulomb interaction between the charge clouds associated with the electronic states, as well as exchange interaction, which results from the anti-symmetry built into the many-electron wavefunction. Due to the strong dependence of the exchange interaction on the overlap of the electron and hole wavefunctions, effects of electron-hole exchange are generally enhanced as the dimensionality of the system decreases. Whereas effects of direct Coulomb interaction dominate in the bulk and QWs, effects of electron-hole exchange govern the band-edge exciton fine structure in QDs subject to strong confinement.

#### Electronic bandstructure in zinc-blende- and wurtzite- type semiconductors

Semiconductors with zinc-blende/wurtzite crystal structure such as GaAs (zinc-blende) or CdSe (zinc-blende or wurtzite) generally feature p-like VBs and s-like CBs. Taking electron spin into account, VB and CB are thus typically six-fold and two-fold degenerate in a first approximation. The single-particle eigen-states of the CB and the VB denoted here by  $|e, \mathbf{k}_e\rangle$  and  $|h, \mathbf{k}_h\rangle$  respectively, correspond to Bloch functions  $\psi_{\alpha, \mathbf{k}}(\mathbf{r})$  in real space representation, i.e. plane waves characterized by crystal momentum  $\mathbf{k}$  modulated by a lattice periodic part according to  $\psi_{\alpha, \mathbf{k}}(\mathbf{r}) = u_{\alpha, \mathbf{k}}(\mathbf{r})e^{i\mathbf{k}\cdot\mathbf{r}}$  ( $\alpha = e$ : electron,  $h$ : hole). In the single-particle picture, CB and VB dispersion  $E_{\alpha}(\mathbf{k})$  are determined by an effective potential  $V(\mathbf{r})$ , which accounts for the effects of the crystal lattice and the mean-field produced by the valence electrons in the crystal (Hartree-Fock approximation). In its ground state, a semiconductor is characterized by fully occupied VBs and empty CBs. Absorption of light corresponds to a pair creation process, in which a photon with energy larger than the band-gap  $E_g$  excites an electron from the VB into the CB, leaving a hole behind in the VB.

Both GaAs and CdSe are direct-gap semiconductors. Thus, for a discussion of optical excitations near the band-edge, which is of interest here, only the CB and VB dispersion near the center of

the Brillouin zone ( $\Gamma$ -point) is of importance. Calculations of the CB dispersion near the  $\Gamma$ -point are typically carried out using the  $\mathbf{k}\cdot\mathbf{p}$ -method and group theoretical arguments to exploit the symmetry properties of the crystal<sup>30</sup>. To second order in  $\mathbf{k}$ , the energy dispersion of the CB near the  $\Gamma$ -point in zinc-blende and wurtzite type crystals is parabolic and isotropic (zero energy defined at the top of the VB):

$$E_e(\mathbf{k}) = E_g + \frac{\hbar^2}{2m_e^*} k^2 \quad (2.1)$$

$$m_e^* \approx \frac{m_0^2 E_g}{2P^2}$$

The energy dispersion for crystal electrons is formally equivalent to that of electrons with mass  $m_0$  in free space. The effective mass  $m_e^*$  accounts for the effects of the mean-field potential  $V(\mathbf{r})$ . Neglecting mixing with higher lying bands,  $P$  is given by the momentum operator matrix element between the CB- and the VB- Bloch-states at the  $\Gamma$ -point according to  $P = |\langle \mathbf{h}, \mathbf{0} | \mathbf{p} | \mathbf{e}, \mathbf{0} \rangle|$  ( $2P^2/m_0 \sim 20\text{eV}$  for most group-IV, III-V and II-VI semiconductors).

Calculation of the energy dispersion for the p-like VB is more complicated, due to spin-orbit coupling. In analogy to atomic systems, the effects of spin-orbit coupling are readily accommodated in a description based on total angular momentum eigenstates  $|J, J_z\rangle$ . The total angular momentum operator  $\mathbf{J}$  is the sum of the orbital angular momentum operator  $\mathbf{L}$  and the electron spin operator  $\mathbf{s}_e$  ( $\mathbf{J} = \mathbf{L} + \mathbf{s}_e$ ). Since the VB is p-like, only the subspace  $l = 1$  is of interest. The six degenerate states  $|J, J_z\rangle = |3/2, \pm 3/2\rangle, |3/2, \pm 1/2\rangle, \text{ and } |1/2, \pm 1/2\rangle$  characterize thus the VB at the  $\Gamma$ -point. Spin-orbit interaction suppresses the two states with zero orbital angular momentum  $|1/2, \pm 1/2\rangle$ , which give rise to the split-off (so)-band. The size of the spin-orbit splitting usually allows to neglect the split-off band in a discussion of the band-edge. The fourfold

degenerate  $J = 3/2$  manifold defines thus the top of the VB<sup>30</sup>. The dispersion of the VB is obtained from the Kohn-Luttinger Hamiltonian<sup>31</sup>:

$$\hat{H} = \frac{1}{2m_0} \left[ (\gamma_1 + 5\gamma_2/2)k^2 - 2\gamma_2(k_x^2\hat{J}_x^2 + k_y^2\hat{J}_y^2 + k_z^2\hat{J}_z^2) - 4\gamma_3(k_xk_y + k_yk_x)(\hat{J}_x\hat{J}_y + \hat{J}_y\hat{J}_x) + \dots \right] \quad (2.2)$$

The z-axis is chosen along one of the crystal axis, i.e.  $z \parallel [001]$ . The diagonal matrix elements of the Kohn-Luttinger Hamiltonian in the basis  $\{|3/2, \pm 3/2\rangle, |3/2, \pm 1/2\rangle\}$  readily provide the dispersion of the  $J = 3/2$  four-dimensional manifold:

$$E_{HH}(J_z = \pm 3/2) = -\frac{\hbar^2}{2m_0}(\gamma_1 + \gamma_2)(k_x^2 + k_y^2) - \frac{\hbar^2}{2m_0}(\gamma_1 - 2\gamma_2)k_z^2 \quad (2.3)$$

$$E_{LH}(J_z = \pm 1/2) = -\frac{\hbar^2}{2m_0}(\gamma_1 - \gamma_2)(k_x^2 + k_y^2) - \frac{\hbar^2}{2m_0}(\gamma_1 + 2\gamma_2)k_z^2$$

In contrast to the CB, the dispersion of the VB is anisotropic. The VB-dispersion is characterized by the Luttinger parameters  $\gamma_1$  and  $\gamma_2$ . The effective masses along the  $k_z$ -axis are used to denote  $|3/2, \pm 3/2\rangle$  as the heavy-hole (HH) states with mass  $m_{HH,\parallel} = m_0/(\gamma_1 - 2\gamma_2)$ . States  $|3/2, \pm 1/2\rangle$  correspond to the light-hole (LH) states, with mass  $m_{LH,\parallel} = m_0/(\gamma_1 + 2\gamma_2)$ . Note that along the  $k_x$  ( $k_y$ )-direction, the effective mass of the LH,  $m_{LH,\perp} = m_0/(\gamma_1 - \gamma_2)$ , can be larger than the effective mass of the HH,  $m_{HH,\perp} = m_0/(\gamma_1 + \gamma_2)$  as is the case e.g. in GaAs (reversal of curvature).

The results of the above discussion are summarized graphically in Figure 4. Bulk CdSe occurs in wurtzite phase under the conditions considered here. In contrast to zinc-blende type crystals, the VB degeneracy at the  $\Gamma$ -point is lifted by crystal field splitting  $\Delta_{cf}$ , due to the reduced symmetry in the hexagonal lattice. Following conventional notation, A, B and C are used to denote the VB sub-structure.

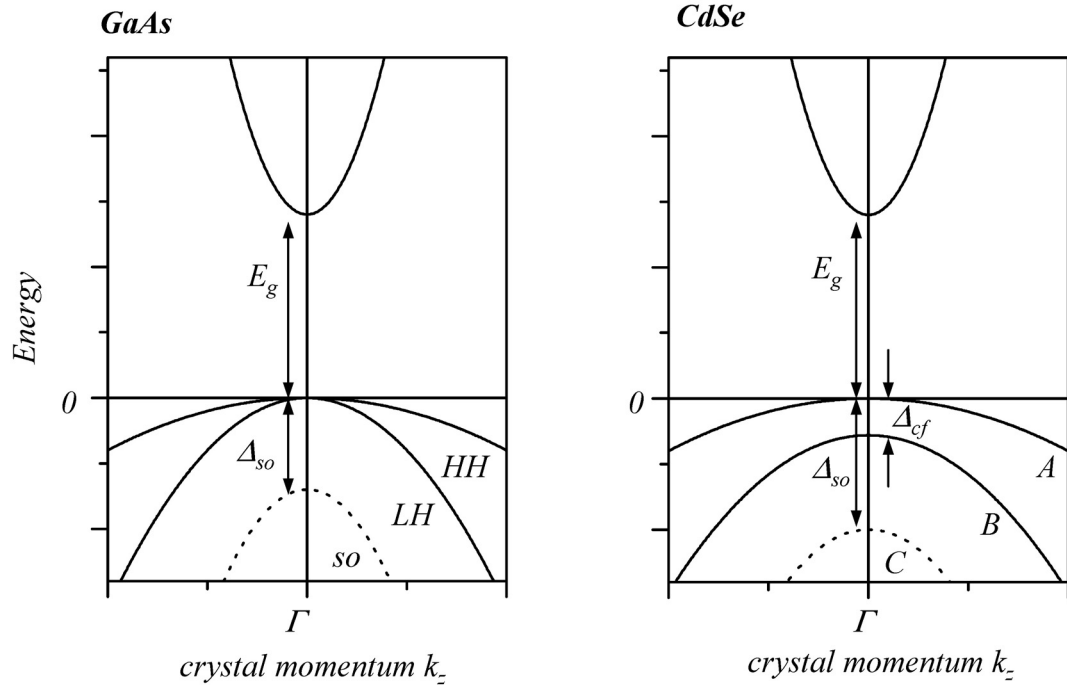


*FIGURE 4. Left: generic bandstructure for zinc-blende type semiconductors such as GaAs. Each band is two-fold degenerate. The spin-orbit interaction partially lifts the six-fold degeneracy of the VB. The top of the VB is four-fold degenerate at the  $\Gamma$ -point and characterized by heavy-hole (HH) and light-hole (LH) states away from it. Right: generic band-structure for wurtzite type semiconductors such as CdSe. The crystal field of the hexagonal lattice splits the four-fold degeneracy at the  $\Gamma$ -point.*

A selection of physical parameters for GaAs and CdSe relevant for our discussion is summarized in Table 1. Effects of confinement as well as Coulomb interaction are introduced separately within the EMA in the next two sections in a discussion of Coulomb interaction in the absence of confinement, followed by a discussion of confinement in the absence of Coulomb interaction.

Physical Property	GaAs	CdSe	Ref. GaAs/CdSe
Lattice Parameter [ $\text{\AA}$ ]	$a = 5.65$ (300K)	$a = 4.30 / c = 7.01$ (300K)	a / b
Direct Gap [eV]	$E_g = 1.52$ (4.2K)	$E_g(A) = 1.83 / E_g(B) = 1.86$ (80K)	a / b
Spin-orbit splitting [eV]	$\Delta_{so} = 0.34$ (4.2K)	$\Delta_{so} = 0.42$ (77K)	a / b
$e$ - effective mass [ $m_0$ ]	$m_e = 0.063$ (300K)	$m_e = 0.12$ (293K)	a / b
Luttinger Parameters, $\gamma_1/\gamma_2$	6.85 / 2.1	2.04 / 0.58	c / d
Exciton binding energy [meV]	$E_B = 4.2$	$E_B(A) = 15 / E_B(B) = 16$	e / b
Exciton Bohr radius [ $\text{\AA}$ ]	$a_B \sim 140$	$a_B \sim 56$	e / f
Dielectric constant	$\epsilon(0) = 12.4$	$\epsilon(0)_   = 10.2$	a / b

Refs.:

- a: Semiconductors: group IV elements and III-V compounds / editor O. Madelung (Springer, Berlin, 1991)  
b: Semiconductors: Other than group IV elements and III-V compounds / editor O. Madelung (Springer, Berlin, 1992)  
c: Y. Chen et al., Phys. Rev. B **37**, 6429 (1987)  
d: D.J. Norris, M.G. Bawendi, Phys. Rev. B **53**, 16338 (1996)  
e: D.S. Chemla, Helv. Phys. Acta **56**, 607 (1983)  
f: M. Nirmal, L. Brus, Acc. Chem. Res. **32**, 407 (1999)

**TABLE 1.** Selection of physical parameters for gallium-arsenide (GaAs) and cadmium-selenide (CdSe).

### Wannier excitons

In the preceding discussion of the electronic bandstructure many-body interactions between crystal electrons have been neglected. Coulomb interaction between electrons gives yet rise to correlated electron-hole pairs, and profoundly affects the linear and nonlinear optical properties of semiconductors. It is well known, that the absorption in bulk and QWs features a series of peaks below the band-gap and enhancement in the continuum above it. The series of discrete peaks originates from hydrogen-like bound electron-hole pairs or excitons. The enhancement above the band-gap is due to the continuum of unbound scattering states of correlated electron

hole pairs<sup>32</sup>. Excitons in semiconductors feature relatively weak binding energies (few meV) and are classified as Wannier excitons, in contrast to the strongly bound Frenkel excitons in insulators. To briefly sketch a mathematical treatment of Wannier excitons in direct-gap semiconductors, we express the exciton wavefunction as a linear superposition of pair states. Note that a discussion based on the EMA is justified, as Wannier excitons, due to their weak binding, are made up of electron-hole pair states near the  $\Gamma$ -point. For simplicity we further assume that CB and VB are non-degenerate and isotropic. The state  $|p\rangle$  is defined as an electron-hole pair state created out of the crystal ground state  $|g\rangle$ :

$$|p\rangle = c_e^+(\mathbf{k}_e) c_h^+(\mathbf{k}_h) |g\rangle \quad (2.4)$$

The operators  $c_e^+(\mathbf{k})$  and  $c_h^+(\mathbf{k})$  denote the creation operators for electrons and holes with crystal momentum  $\mathbf{k}$  respectively. In the center of mass (CM) system, the overall motion of the electron-hole pair is split into the translational CM motion of a particle with mass  $M = m_h + m_e$  and CM momentum  $\mathbf{K} = \mathbf{k}_e + \mathbf{k}_h$ , and the rotational motion of a particle with reduced mass  $\mu$  given by  $1/\mu = 1/m_e + 1/m_h$  and reduced momentum  $\mathbf{k} = (m_e \mathbf{k}_e - m_h \mathbf{k}_h)/(m_e + m_h)$ . For optical excitations, momentum conservation requires  $\mathbf{K} = \mathbf{0}$ , since photon momentum at optical frequencies is negligible. For photo-generated excitons, the exciton wavenfunction  $|X_{nlm}\rangle$  is thus a superposition of pair states with zero center of mass momentum:

$$|X_{nlm}\rangle = \sum_{\mathbf{k}} \phi_{nlm}(\mathbf{k}) c_e^+(\mathbf{k}) c_h^+(-\mathbf{k}) |g\rangle \quad (2.5)$$

The exciton wavefunction in real space  $\phi_{nlm}(\mathbf{r})$  is defined as the Fourier transform of the expansion coefficients  $\phi_{nlm}(\mathbf{k})$  in Eq.(2.5). It obeys the hydrogenic Schrödinger equation for a particle with reduced mass  $\mu$  in a dielectric medium.

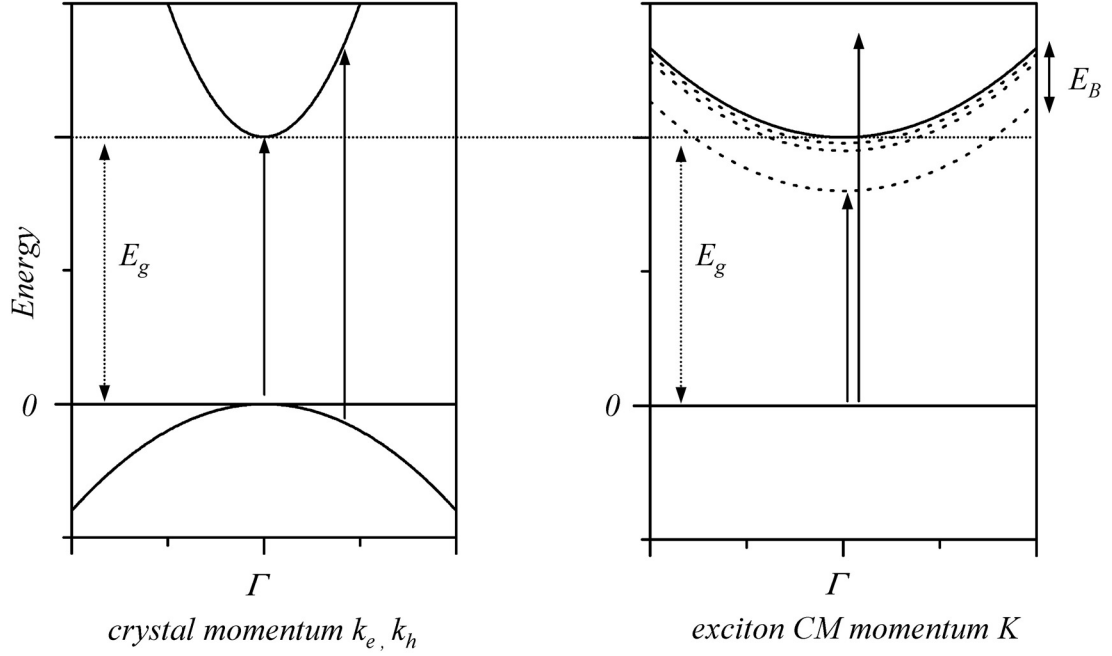


*FIGURE 5. Left: electron/hole dispersion in the single-particle picture for parabolic and non-degenerate CB/VB. Right: exciton dispersion. Coulomb interaction gives rise to bound and unbound but correlated electron-hole pairs (excitons). Arrows indicate optical excitation at the band-edge/in the continuum.*

The set of indices  $(n, l, m)$  is used in accordance with general nomenclature for hydrogenic orbitals. Employing the well known results for the hydrogen atom, we replace the free electron mass by the reduced mass of the electron-hole pair and introduce dielectric screening to obtain the exciton binding energy  $E_B$  and the exciton Bohr radius  $a_B$  of the 1s-exciton ( $n = 1, l = 0$ ) in terms of the corresponding values in a hydrogen atom ( $E_B^H = 13.6\text{eV}$  and  $a_B^H = 0.53\text{\AA}$ ):

$$E_B = \left( \frac{1}{\epsilon_r^2} \frac{\mu}{m_0} \right) E_B^H$$

$$a_B = \left( \epsilon_r \frac{m_0}{\mu} \right) a_B^H$$
(2.6)

The small effective masses, in combination with dielectric screening give rise to exciton binding energies three orders of magnitude smaller than the Rydberg energy, and exciton Bohr radii two orders of magnitude larger than the Bohr radius. As for the hydrogen atom, binding energies of higher excited excitons decrease as  $1/n^2$  ( $n$ : principal quantum number). The continuum (scattering) states are approached as  $n \rightarrow \infty$ . Including the CM-motion as well as exciton binding, the exciton dispersion is given by:

$$E_{exc}(\vec{K}, n) = E_g + \frac{\hbar^2 K^2}{2M} - \frac{E_B}{n^2} \quad (2.7)$$

Parabolic CB and VB have been assumed. Figure 5 contrasts the energy dispersion in a single- and a many- particle picture. The linear optical properties of excitons are given by Elliott's formula<sup>33</sup>:

$$\chi(\omega) \propto |P|^2 \sum_{nlm} \frac{|\phi_{nlm}(r=0)|^2}{E_n - \omega - i\gamma} \quad (2.8)$$

Only hydrogenic s-states are optically active. Evaluation of the probability density  $|\phi_{nlm}(r=0)|^2$  in Eq.(2.8) of the hydrogenic s-states shows that exciton oscillator strengths scale as  $1/n^3$ .

While we exploited the analogy with hydrogenic orbitals in order to introduce Wannier excitons in semiconductors, note that resonant optical excitations differ fundamentally for atomic systems and excitons. Resonant optical excitation of atomic systems, such as hydrogen, corresponds to lifting an electron from its initial, e.g. the 1s-orbital, into a higher lying orbital. In contrast, excitons are created into, e.g. the 1s- or higher lying states, via resonant optical excitation of the exciton out of the crystal ground state (vacuum). In a description of resonant light-matter interaction, dilute atomic systems can be treated as ensembles of independent two-level systems in which optical nonlinearities arise exclusively from state filling<sup>7</sup>. In contrast, many-body effects

scaling with the density of photoexcited excitons, such as Coulomb screening or excitation induced dephasing (EID), genuinely determine excitonic nonlinearities. Although present, state-filling (more precisely, band-filling in semiconductors), presents only one of many conspiring mechanisms, which generates the overall nonlinear optical response from semiconductors<sup>34</sup>. The relative contribution from these various mechanisms depends sensitively on the dimensionality of the system. For example, state filling becomes increasingly important in QDs, which feature discrete atom-like energy level structures<sup>8</sup>. In this sense, not only the linear but also the nonlinear optical properties can be engineered to some extent in low-dimensional semiconductor nanostructures. This flexibility explains the interest in low-dimensional semiconductors as promising candidates for applications of coherent optical control.

#### Effects of confinement on single particle states

Effects of confinement are well known from quantum mechanics text books and typically discussed for particles subject to a cuboidal confinement potential ( $L_x = L_y = L_z = L$ ) with infinitely high potential barriers. The regime of interest is one in which at least one of the dimensions  $L_i$  ( $i = x, y, z$ ) of the sample becomes comparable to the de Broglie wavelength of the crystal electrons, thus introducing effects of confinement. Ignoring for the moment complications tied to confinement induced mixing of the VB-states, text book results can be carried over to discuss the effects of confinement on electrons/holes in a semiconductor nanostructure within the EMA. The most important characteristic of confinement is the splitting of CB and VB into CB and VB sub-bands labelled by  $\{n_i\}$ , the set of quantum numbers used to classify the eigen-states for a cuboidal confinement potential. As electron effective masses are typically smaller than effective hole mass, sub-bands associated with the CB exhibit generally larger intra-band spacing than corresponding sub-bands emerging from the VB.

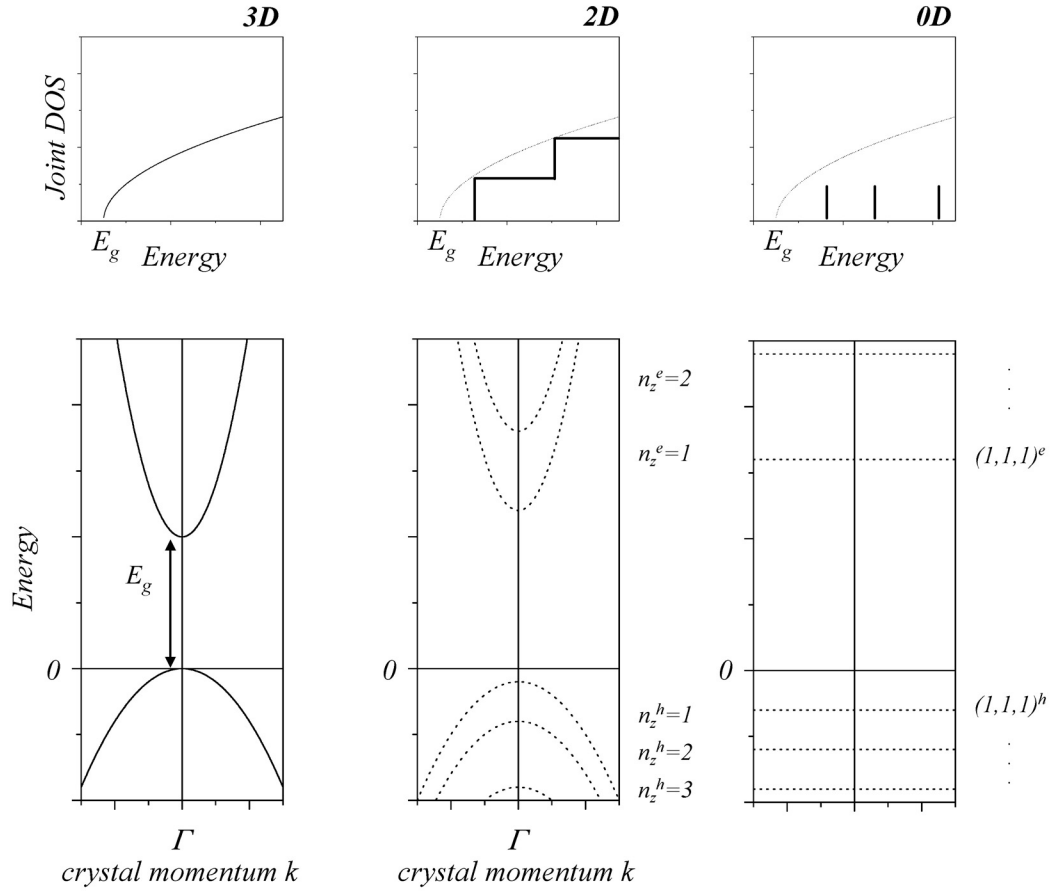


**FIGURE 6.** Energy dispersion (bottom row) and corresponding joint DOS (top row) for ideal three-, two- and zero- dimensional systems.

The confinement energy  $E(n_x, n_y, n_z)$  exhibits a generic  $1/L_i^2$  dependence. Low-dimensional semiconductor structures exhibit thus a characteristic, size-tuneable blue shift with respect to the bulk absorption, which has been exploited for device applications (bandgap engineering). The energy level structures along with the joint DOS  $\rho^{\alpha D}(E)$  in  $\alpha=3,2,0$  dimensions are shown in Figure 6. Only optically allowed transitions have been included in the joint DOS (selection rule:  $(n_x, n_y, n_z)^e = (n_x, n_y, n_z)^h$ ). Given the proportionality between the linear optical absorption  $\alpha$  and

the joint DOS (Fermi's Golden Rule), Figure 6 reveals the characteristic square-root, step-like, and  $\delta$ -function like behaviour for the linear absorption from inter-band transitions in three-, two-, and zero- dimensional systems. The collapse of the continuous band-to-band transitions in bulk into discrete atom-like transitions in QDs, leads to a high concentration of the oscillator strength in QDs.

In a discussion of real semiconductor QW-systems, eigen-states and eigen-energies have to be calculated for finite electron/hole potential barriers, as determined by the CB and VB offsets ( $\Delta E_{CB}$ ,  $\Delta E_{VB}$ ) in the heterostructure<sup>26</sup>. As a result of finite band-offsets, electrons/holes can penetrate into the barrier, and the number of confined states is finite. Similar to ideal two-dimensional systems, sub-bands are still labelled by  $n_z$ , which determines the number ( $n_z-1$ ) of nodes of the sinusoidal envelope functions  $\psi^{e/h}[n_z]$  inside the well (see Figure 7).

The schematic on the right in Figure 7 shows the generic structure of a CdSe/ZnS core/shell nanocrystal. Typical aspect ratios for these colloidal QDs are on the order of 1.1-1.3; calculations of confined electronic states in nanocrystals are thus generally based on the assumption of a spherical confinement potential. As a result, electron/hole envelope functions are labelled by  $(n, l, m)$ , using standard convention for the eigen-states of a spherically symmetric potential. Including the CB- and VB- degeneracy as discussed for the bulk band-structure, the lowest energy confined electronic state in spherical CdSe-QDs is labelled  $1S_e$  ( $n = 1$ , and S for  $l = m = 0$  to denote the envelope function, e denoting electron spin). It is two-fold degenerate with respect to electron spin. Similarly, the lowest energy confined hole state is labelled  $1S_{h,3/2}$  ( $n = 1$ , S for  $l = m = 0$ , and 3/2 to denote the  $J = 3/2$  total angular momentum sub-space). It is four-fold degenerate, if mixing of the VB states is not taken into account. In a first approximation, the band-edge exciton ( $1S_{h,3/2}1S_e$ ) in CdSe-nanocrystals is thus eight-fold degenerate.

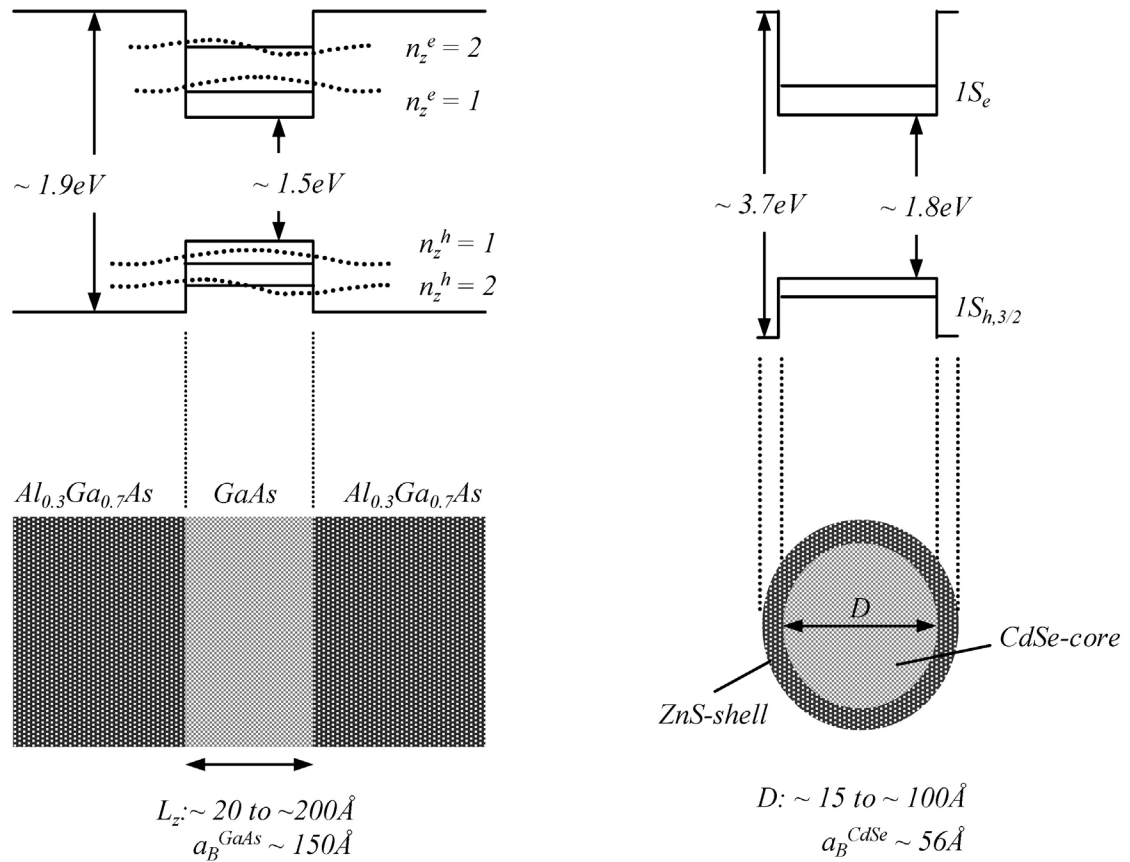


**FIGURE 7.** Left/right: schematic of a GaAs/Al<sub>x</sub>Ga<sub>1-x</sub>As QW-structure / core/shell CdSe /ZnS nanocrystal. Both nanostructures are of type-I, i.e. electrons and holes are confined within the same region.

In contrast to the spheroidal nanocrystals, epitaxially grown dots exhibit disk-like shapes. The confinement potential in epitaxially grown dots is typically determined by a square well potential in the growth direction as defined by the wetting layer. Additional lateral confinement, details of which are governed by the morphology of the particular QD-system, gives rise to zero-dimensional confinement. If the lateral confinement is weaker than the confinement in the growth direction, the ground-state exciton is determined by the HH-exciton of the QW (i.e. the wetting layer). As we will see, electron-hole exchange in QDs depends sensitively on the dot shape.

### Degrees of confinement and the strong confinement regime

The central question in a unified theoretical treatment of confinement and many-body effects is how many sub-bands of the confined structure need to be included in an accurate description of the ground-state exciton. To answer this question, an estimate of the ratio between electron/hole intra-sub-band spacings, which are on the order of  $\hbar^2 D / 2m_{e/h} L^2$  ( $D \sim \pi^2$ ) and the exciton binding energy in bulk given by  $\hbar^2 / 2\mu a_B^2$  provides important insight. The ratio between the two energy scales defines a weak, intermediate and strong confinement regime, depending on whether the confinement energy is much smaller, on the same order, or much larger than the Coulomb binding energy. Re-stating this condition in terms of the characteristic length scales involved, we obtain the following condition for e.g. the strong confinement regime ( $m_e < m_h$ ,  $\mu \sim m_e$ ):

$$\frac{\hbar^2 D}{2m_h L^2} \gg \frac{\hbar^2}{2m_e a_B^2} \Leftrightarrow \left( \frac{L}{a_B} \right)^2 \ll \frac{m_e}{m_h} D \quad (2.9)$$

The inequality in Eq.(2.9) shows that strong confinement is achieved, if the bulk exciton Bohr radius exceeds the dimensions of the confined structure. In the strong confinement regime, the ground-state exciton is mainly composed of the lowest energy electron/hole sub-bands of the confined structure, e.g. characterized by  $n_z^e = n_z^h = 1$  in QWs, or  $1S_{h,3/2}$  and  $1S_e$  in spherical QDs. Due to the relatively large sub-band spacing in the strong confinement regime, mixing with higher sub-bands due to Coulomb interaction is negligible. Strong confinement applies to all semiconductor nanostructures considered here (in QWs, strong confinement applies to the growth direction only). Effects of dielectric confinement, which are caused by discontinuities of the dielectric constant at the hetero-interfaces are not of importance here, as the mismatch of the dielectric constants in the semiconductor nanostructures considered is small.

### Band-edge exciton in GaAs quantum wells

For simplicity, we previously assumed non-degenerate CBs and VBs to illustrate the generic effects of confinement in two-dimensional systems. The results obtained can be carried over to CB-electrons in QWs, since the electron spin is unaffected by effects of confinement. A discussion of confinement effects on the VB however requires treatment of the  $\mathbf{k}\cdot\mathbf{p}$ -perturbation and confinement potential on an equal footing. Physical insight is readily obtained by ignoring in a first approximation mixing of HH and LH by the confinement potential. Then, due to its smaller effective mass, the LH experiences stronger confinement than the HH. As a result, the HH-LH degeneracy at the  $\Gamma$ -point is lifted. In fact, effects of HH-LH mixing become important only away from the  $\Gamma$ -point. At the  $\Gamma$ -point, HH and LH character are preserved and the VB splits into two sets of sub-bands for the HH and the LH respectively. Figure 8 shows the generic in-plane dispersion for the lowest energy sub-bands ( $n_z^e = n_z^h = 1$ ) of the CB and the VB. The LH1 is energetically suppressed with respect to the HH1 and exhibits a smaller in-plane curvature than the HH1. As a result of this reversal of curvature, HH1 and LH1 would cross. Band mixing gives rise to a camel back shape in the in-plane VB-dispersion (level repulsion). The diagram to the right shows the level structure at the  $\Gamma$ -point in the single particle picture including HH1 only. The states are labelled using the  $z$ -projection of the electron spin to denote the CB electrons and the  $z$ -projection of the total angular momentum to denote the hole states. Also shown are the dipole allowed inter-band transitions. Following general convention,  $\sigma^+$  and  $\sigma^-$  denote right- and left- circularly polarized light respectively.

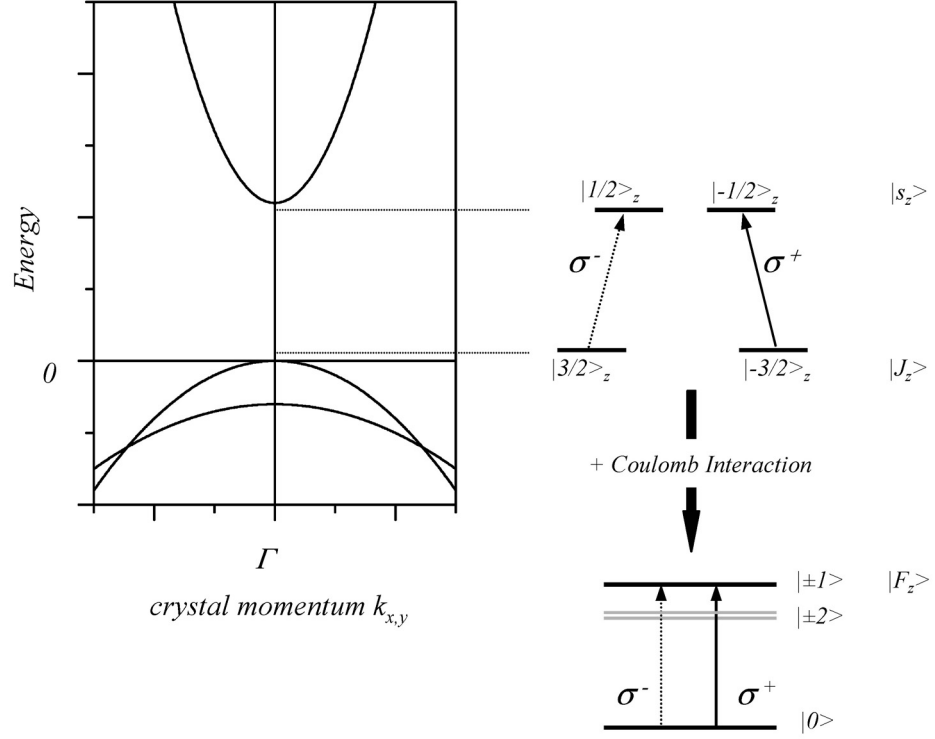


**FIGURE 8.** Left: in-plane dispersion of the  $n_z^e = n_z^h = 1$  subbands in a QW. Confinement induced band-mixing leads to level repulsion and thus anti-crossing of the HH1/LH1 dispersion (not shown). Right: single-particle level structure at the  $\Gamma$ -point including HH1 only and selection rules. Right bottom: HH1-exciton in a many-body level diagram. Exchange gives rise to a bright-dark splitting.

To discuss the effects of Coulomb interactions, we simply note that a treatment of Wannier excitons in 2D and 3D is formally similar and present the most important results for our purposes<sup>26</sup>:

$$\begin{aligned}
 E_n^{3D} &= -\frac{E_B}{n^2} & E_n^{2D} &= -\frac{E_B}{(n-1/2)^2} \\
 f_n^{3D} &\sim \frac{P^2}{n^3} & f_n^{2D} &\sim \frac{P^2}{(n-1/2)^3}
 \end{aligned}
 \tag{2.10}$$

$E_n^{\alpha D}$  and  $f_n^{\alpha D}$  ( $\alpha = 2,3$ ) denote exciton energy and oscillator strength respectively. Eq.(2.10) shows that the binding energy of the ground-state exciton in the pure two-dimensional case is four times larger than in the bulk. The enhancement of the exciton binding energy and the oscillator strength for the 1s-exciton result from the larger overlap of the electron and hole wavefunction in two-dimensions. Despite penetration of the electron/hole wavefunction into the barrier, the exciton binding energy in real semiconductor QWs is enhanced over the bulk. For an alloy composition of  $x = 0.3$  in the  $Al_xGa_{1-x}As$  barrier, the binding energy reaches its maximum at  $\sim 2E_B \sim 9\text{meV}$  for  $L_z/a_B \sim 0.4$  ( $L_z \sim 50\text{\AA}$ ) and enhancement of QW-exciton binding is predicted for  $1/4 < L_z/a_B < 1$ <sup>26</sup>. A level structure diagram including the effects of Coulomb interaction is also shown in Figure 8 for the HH1-exciton. To account for exchange induced mixing of electron and hole states, the exciton states are conveniently expressed in terms of total angular momentum operator eigen-states:  $|F, F_z\rangle$  ( $F_z = J_z + s_z^e = \pm 1, \pm 2$ ). In the absence of exchange interaction, all four electron-HH1 pair states are degenerate. As shown, exchange interaction leads to a splitting of the bright  $|\pm 1\rangle$  and dark  $|\pm 2\rangle$  states<sup>35</sup>. The HH1-exciton level structure will be discussed in more detail in Chapter III in the context of N-exciton states.

#### Band-edge excitons in CdSe quantum dots

As a result of the increased overlap of electron and hole wavefunctions in zero-dimensional structures, effects of electron-hole exchange can be significantly enhanced over the bulk. Exchange interaction plays therefore a crucial role in determining the exciton fine structure in QD-systems, while the effects of direct Coulomb interaction are secondary in QDs subject to strong confinement. Due to the sensitivity of the exchange interaction to the overlap of electron and hole wavefunction, the band-edge exciton fine structure in QDs depends critically on the dot size and shape<sup>29</sup>. The exchange interaction is generally divided into a short-range (SX) or

analytical-, and a long-range (LX) or non-analytical- part. For spherical QDs in the strong confinement regime, such as colloidal CdSe-nanocrystals, the SX scales generally as  $1/R^3$  (R: dot radius) whereas the LX is negligible (a non-vanishing LX requires asymmetry of some sort, e.g. dot shape or strain induced). For disk-shaped QDs, such as self-assembled CdSe-QDs, the SX scales generally as  $1/R^2$ ; LX is finite and scales as  $1/R^3$  (R: disk radius). As a result of the distinct shape and size dependence of the SX and the LX, the exciton band-edge has been discussed separately for spheroidal CdSe-nanocrystals and disk-shaped self-assembled CdSe-QDs. One characteristic of bulk CdSe is the crystal field splitting ( $\sim 25\text{meV}$ ), which lifts the VB degeneracy at the  $\Gamma$ -point giving rise to the A and B band. Due to coupling of electrons and holes via the exchange interaction, electron-hole pair states are characterized by the z-projection  $F_z$  of the total angular momentum operator  $F$  ( $F_z = J_z + s_z$ ). In a calculation of the band-edge exciton in CdSe-nanocrystals, both A and B bands are generally included, since the strong size dependence of the SX in spherical dots can lead to exchange splittings on the order of the crystal field. The band-edge CdSe-nanocrystals is thus typically discussed in terms of the eight-fold degenerate manifold ( $1S_{h,3/2}1S_e$ ). Exchange splittings observed in self-assembled CdSe-QDs are one order of magnitude smaller than the crystal field splitting in bulk CdSe. Previous calculations of the ground-state exciton in self-assembled CdSe-QDs have only included the A band, i.e. the HH1-exciton<sup>36</sup>.

Figure 9 presents schematically the effects of electron-hole exchange on the band-edge exciton in self-assembled CdSe-QDs. The four, initially degenerate, HH1-exciton states are split into doublets of bright  $|\pm 1\rangle$  and dark  $|\pm 2\rangle$  states by the SX. In addition, the LX gives rise to a splitting of both bright and dark doublets and to suppression of the bright states<sup>28,36</sup>. In self-assembled CdSe-QDs, the dark exciton  $|\pm 2\rangle$  lies energetically below the bright exciton  $|\pm 1\rangle$ .

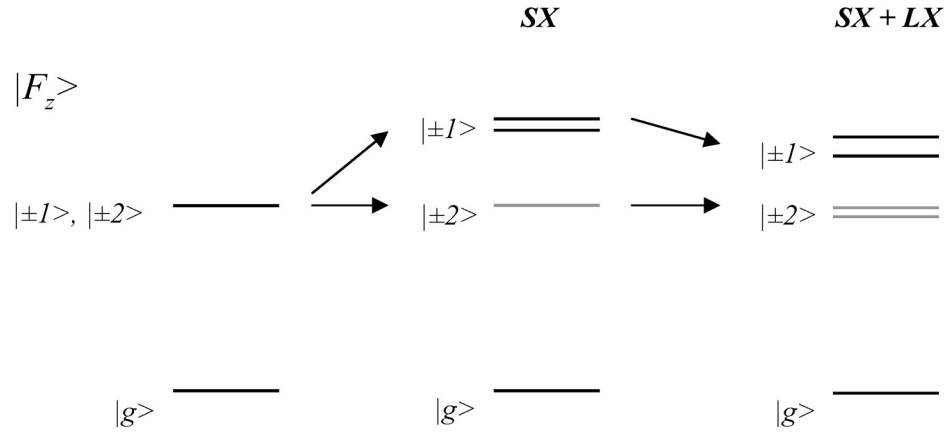


**FIGURE 9.** Effects of  $SX$  and  $LX$  part of the exchange interaction in self-assembled CdSe-QDs. In the absence of  $SX$  and  $LX$  the HHI-exciton is fourfold degenerate. The  $SX$  gives rise to splitting into bright and dark states. The effect of the  $LX$  is to split the dark doublet and suppress the bright doublet.

Note that in interface fluctuation GaAs-QDs, the  $LX$  pushes the bright doublet below the optically dark states<sup>29</sup>. Previously measured values of the bright-dark splitting, bright doublet splitting, dark doublet splitting in self-assembled CdSe-QDs are on the order of 2meV, 200 $\mu$ eV and 20 $\mu$ eV respectively<sup>28</sup>. As the  $LX$  arises from dot asymmetries (shape, strain profile etc.), the magnitude of the bright-dark is sensitive to aspect ratios or strain, and can thus vary between individual QD-dots.

Due to the near-spherical shape of nanocrystals, effects of  $LX$  have been neglected previous calculations of the band-edge exciton fine structure in CdSe-nanocrystals<sup>27</sup>. Both bands, A and B however, are included in  $SX$  induced mixing within the  $(1S_{h,3/2}1S_e)$  manifold. The combined effects of crystal field splitting and the  $SX$ , leads to a splitting of the exciton manifold into five levels according to  $F_z = \pm 2, \pm 1^L, \pm 0^L, \pm 1^U, \pm 0^U$  in ascending order in energy. The resulting level

structure is depicted in Figure 10. As for self-assembled CdSe-QDs, the lowest energy exciton of the band-edge manifold is an optically dark doublet ( $|\pm 2\rangle$ ). The next higher exciton forms an optically bright doublet ( $|\pm 1\rangle^L$ ). Of interest in the measurements on dipole dephasing in CdSe-QDs is the homogeneous linewidth associated with the lowest bright exciton, i.e.  $|\pm 1\rangle$  in CdSe-QDs and  $|\pm 1\rangle^L$  in CdSe-nanocrystals.

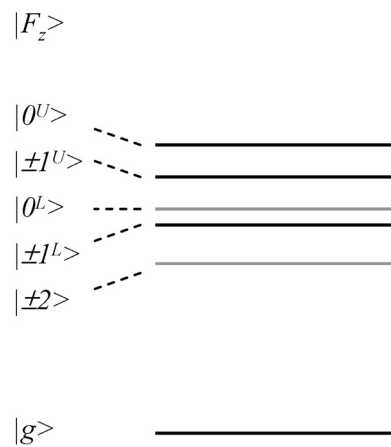


**FIGURE 10.** Generic level structure of the band-edge exciton ( $1S_{h,3/2} 1S_e$ ) in CdSe nanocrystals including the effects of exchange interaction ( $SX$  only).

### Summary

We have presented the general concepts applying to a discussion of the band-edge exciton fine structure in semiconductor nanostructures. Starting point is the EMA appropriate for a description of the bulk electron/hole dispersion near the band-edge. In contrast to the simple case of a ‘particle in a box’, a description of the effects of confinement on electrons and holes in semiconductor nanostructures is complicated by the VB-degeneracy. In GaAs-QWs, the discussion is simplified for the dispersion near the  $\Gamma$ -point, where HH- and LH- character are

preserved despite the presence of confinement. Confinement induced mixing of HH and LH states occurs only away from the Brillouin zone center. The CB splits into a series of sub-bands as do HH and LH bands. Effects of the direct Coulomb interaction give rise to bound electron hole pairs with binding energies that are enhanced over the bulk.

In the QD-systems considered, exchange interaction gives rise to a distinct fine structure of the band-edge exciton. Energy splittings between the states within the band-edge exciton manifold depend sensitively on dot size and shape. As a general feature, note that for both CdSe-QD-systems considered, the lowest energy exciton constitutes a dark state.

## CHAPTER III

EXCITON LOCALIZATION, COULOMB CORRELATIONS  
AND IN-PLANE MAGNETIC FIELDS IN QUANTUM WELLS

Three topics are discussed in this chapter, all of which are essential for an understanding of our nonlinear optical studies of electron spin coherence in GaAs-QW-systems: localization of excitons, the relation between Coulomb correlations and excitonic optical nonlinearities, and modifications of the exciton level structure due to in-plane magnetic fields.

Interface disorder and exciton localization in GaAs-quantum wells

The desired effects of confinement in semiconductor nanostructures are generally accompanied by surface- and interface- related phenomena. In GaAs/Al<sub>x</sub>Ga<sub>1-x</sub>As QW-systems in particular, monolayer fluctuations form at the interfaces between the Al<sub>x</sub>Ga<sub>1-x</sub>As-barriers and the GaAs-wells. Due to the well-width dependence of the confinement energy, monolayer fluctuations, if present, result in inhomogeneous broadening of the excitonic absorption spectra<sup>37</sup>. A simple estimate of the inhomogeneous linewidth is obtained from the generic  $1/L^2$  dependence of the confinement energy, which relates well-width fluctuations  $\Delta L$  to variations  $\Delta E_{HH}$  of the HH1 exciton energy, i.e. the inhomogeneous linewidth, according to (well-width dependence of the exciton binding energy is negligible)<sup>38</sup>:

$$\Delta E_{HH} = 2 \frac{\Delta L}{L} E_{HH} \quad (3.1)$$

Eq.(3.1) shows that monolayer fluctuations give rise to inhomogeneous linewidths on the order of a few meV and that effects thereof are more pronounced for narrow wells. Direct evidence for

interface fluctuations in quantum wells has been obtained using imaging techniques such as chemical mapping. Capable of near-atomic resolution, chemical mapping can resolve interfacial atomic configurations and has revealed that transitions between the GaAs-wells and the  $\text{Al}_x\text{Ga}_{1-x}\text{As}$  barrier layers in GaAs/ $\text{Al}_x\text{Ga}_{1-x}\text{As}$  quantum well systems occur over 2-4 unit cells<sup>39</sup>. Interfaces exhibit thus significant atomic roughness with lateral spacings between interfacial steps on the order of the exciton Bohr radius.

Interfacial roughness gives effectively rise to random lateral variations of the QW-potential, which can crucially affect the in-plane motion of excitons in QWs. In analogy to amorphous materials as prototype examples for localization by disorder, well-width fluctuations give rise to localization of excitons in GaAs/ $\text{Al}_x\text{Ga}_{1-x}\text{As}$  QWs<sup>40</sup>. Potential steps induced by monolayer fluctuations are on the order of a few meV. Consequently, effects of exciton localization are only of importance for the HH1-exciton and at low temperatures since thermal activation of localized excitons to delocalized states can occur for temperatures as low as  $\sim 10$  K. Evidence for exciton localization is obtained from measurements of the exciton diffusion coefficient. Transient grating<sup>40,41</sup> and four-wave-mixing<sup>42</sup> experiments at low temperatures show a sharp increase of the exciton diffusion coefficient across the HH1-absorption profile from  $< 2\text{cm}^2/\text{s}$  below the line center to  $20\text{cm}^2/\text{s}$  above the line center. These observations have led to a distinction between localized/mobile excitons, which are spectrally separated below/above the HH1-absorption line center. Whereas localized excitons are laterally confined by an exponentially decaying envelope function, delocalized or mobile excitons are free to move across the island-like structures created by the monolayer fluctuations. In addition to the sharp increase of the exciton diffusion coefficient, measurements of the dephasing rate as a function of the HH1-exciton energy exhibit also a sharp increase with increasing exciton energy at the HH1-absorption line center<sup>41,43</sup>. Thus,

exciton localization affects also dephasing and, as shown in additional time- and spectrally resolved PL studies<sup>38</sup>, energy relaxation of HH1-excitons. For localized excitons, thermal activation to delocalized states dominates dipole dephasing at temperatures above 10 K, whereas acoustic phonon assisted migration (tunnelling) between islands governs dephasing at temperatures below  $\sim 10$  K. Dephasing of mobile excitons has been attributed to scattering with acoustic phonons as well as scattering from the potential fluctuations associated with interface disorder<sup>44</sup>. As revealed in this dissertation, exciton localization does also crucially affect the nonlinear optical response from electron spin coherence as exciton-exciton interactions underlying the nonlinear optical response are profoundly different for localized and mobile excitons. The intricate relation between exciton-exciton interactions and the nonlinear optical response from excitons is established in the next section.

#### Nonlinear optical response from excitons: the role of Coulomb correlations

The nonlinear optical properties of QW-excitons have been extensively studied and the reader is referred to review papers and references therein<sup>34,45</sup>. The goal of this section is to point out how the effects of many-body correlations can be incorporated in a phenomenological few-level approach based on N-exciton eigenstates. In this approach, the nonlinear optical properties of QW-excitons can then be discussed by applying the OBE to level structures, which formally account for many-body effects.

In a mathematical description of resonant light-matter interaction, the OBE have been quite successful in explaining the linear and nonlinear optical properties of atomic systems, which behave essentially like ensembles of non-interacting dipole emitters<sup>7</sup>. Semiconductors as many-body systems consisting of  $10^{22}$ - $10^{23}$  particles per cubic centimetre, are fundamentally different from atomic systems. Accurate descriptions of the linear and nonlinear optical properties of

semiconductors require many-body formalisms, which extend the density matrix formalism beyond the OBE by including the effects of Coulomb interactions. The relevant observables in a description of the optical properties of semiconductors are the expectation values of the electron occupation  $n_{e,k}$ , hole occupation  $n_{h,k}$  and electron-hole coherence  $p_k$  according to:  $n_{e,k} = \langle a_k^\dagger a_k \rangle$ ,  $n_{h,k} = \langle b_{-k}^\dagger b_{-k} \rangle$  and  $p_k^* = \langle a_k^\dagger b_{-k} \rangle$ . The operators  $a_k^\dagger$  and  $a_k$  ( $b_{-k}^\dagger$  and  $b_{-k}$ ) are the electron (hole) creation and annihilation operator respectively for electron (hole) with crystal momentum  $\mathbf{k}$  (photon momentum is neglected;  $n_{e,k} = n_{h,k}$  for intrinsic semiconductors). The observables  $n_{e,k}$  and  $p_k^*$ , which form the diagonal and off-diagonal elements of the density matrix respectively, are expectation values of a product of two operators and represent thus two-point correlation functions. In contrast to the OBE, in which diagonal (population) and off-diagonal (coherence) density matrix elements form a closed set of equations, the equations of motion for  $n_{e,k}$  and  $p_k^*$  include coupling to four-point correlation functions, which are introduced via Coulomb interaction. The coupling of two-point to four-point correlation functions results ultimately in an infinite hierarchy of coupled differential equations including two-point, four point and higher order correlations. In order to cope with the complexities associated with this many-body hierarchy, truncation schemes are generally applied. In a first approximation, the many-body hierarchy is truncated at the two-point level in a mean-field (Hartree-Fock) approach, i.e. four-point correlations are factorised into products of two-point correlations. This leads to the semiconductor Bloch equations (SBE)<sup>46</sup>, which form a closed set of differential equations for  $n_{e,k}$  and  $p_k^*$ . The SBE are formally equivalent to the OBE in certain limiting cases in which the effects of two-point correlations lead to band-gap renormalization and renormalization of the Rabi-frequency. The SBE have been very effective in a description of optical phenomena in an intermediate and high-excitation regime in which mean-field conditions are actually met. At low excitation levels however, effects of higher-order correlations become important and truncation

beyond the two-point level is necessary. This has been addressed in microscopic theories, which have employed dynamics-controlled truncation schemes<sup>47,48</sup>. Truncation schemes are motivated by the fact that the nonlinear optical polarization is usually expressed in terms of a Taylor-series in the applied electric field. Thus, if the analysis is restricted to a finite order in the nonlinear optical polarization, the hierarchy of correlations can be truncated at a given point, beyond which higher-order Coulomb correlations have no effect on the chosen order of the nonlinear polarization. Solutions to a given order in the optical response are thus exact.

Appropriate for our purposes, we follow here a phenomenological approach, in which the OBE are applied to a level scheme, which inherently includes the effects of many-body correlations. Rigorous theoretical foundations for this approach have been provided<sup>49,50</sup>. The central idea consists in separating the static problem of the excitonic eigen-states from the dynamical optical processes. In the absence of light-matter interactions, the true eigen-states of the semiconductor are eigen-states of an exciton number operator<sup>51</sup>. Eigen-states are accordingly labelled by the number  $N$  of excitons present in the system and generally expressed in this  $N$ -exciton basis.

The level diagram on the right in Figure 11 shows the level structure of the HH1-exciton, in which effects of Coulomb correlations have been formally included. Only the one-exciton and the two-exciton subspace are considered. The level diagram on the left shows the corresponding level structure in the single-particle picture. The role of Coulomb correlations in the nonlinear optical response from excitons becomes evident in the limiting case in which the effects of Coulomb interactions vanish, while the eigen-states are expressed in terms of  $N$ -exciton states. This scenario is illustrated in the level diagram shown in the center of Figure 11. In the absence of excitation-exciton interactions, the excitonic system represents essentially a quantum mechanical harmonic oscillator with equally spaced energy-levels of the exciton number states. As for the classical Lorentz-oscillator, the system response is linear irrespective of the excitation level. In

particular, saturation of the system does not occur as the ladder of energy levels associated with the N-exciton states is infinite (states with  $N > 2$  are not shown in Figure 11).



*FIGURE 11. Level structure of the HH1-exciton. Left: single-particle picture. Center: many-particle picture in the limit of vanishing Coulomb interaction. Right: many-particle picture including the effects of Coulomb interaction; 0,1, and 2-exciton states are shown.*

Effects of Coulomb interaction are formally included in the level diagram on the right in Figure 11. The one-exciton states feature a finite exciton binding energy. Effects of exciton-exciton interactions lead to bound and unbound two-exciton states; the energy of the bound exciton (biexciton) is smaller than the sum of the two one-exciton energies by an amount given by the biexciton binding energy. Previous studies have successfully addressed excitonic optical nonlinearities by applying the OBE to this level diagram<sup>52,53</sup>. Here, we will follow this approach to gain insight into the nonlinear optical response from electron spin coherence in QWs and its interconnection with Coulomb correlations.

### Quantum wells in Voigt geometry

In order to optically manipulate the non-radiative electron spin coherence, both CB electron spin states need to be coupled to a common VB-state via dipole allowed transitions. Given the selection rules, this is clearly not the case for the HH1-exciton in GaAs-QWs as shown Figure 12 (left); optical manipulation of the electron spin is thus not possible without appropriate modifications of the HH1-exciton energy level structure. An appropriate level structure is achieved by applying external magnetic fields in the plane of the QW (Voigt geometry). The diagram on the right in Figure 12 shows the resulting energy level diagram along with the modified selection rules, revealing that both electron spin states are coupled to a common VB state.

The theoretical framework for a discussion of the effects of magnetic fields on the bandstructure in semiconductors was first developed by Luttinger<sup>31</sup>. In an extension of this framework to semiconductor QW-systems, note that the growth direction defines a preferred axis in QWs; effects of magnetic fields depend thus sensitively on the relative orientation of the magnetic field with respect to the growth axis. For magnetic fields applied along the growth direction, Landau levels result due to the formation of discrete cyclotron orbits. In contrast, for in-plane magnetic fields, the formation of Landau levels is hindered as cyclotron orbits lie in a plane intersecting the well and the barrier material<sup>54</sup>. Due to the absence of spin-orbit coupling for the CB, electron spins simply align with externally applied magnetic fields irrespective of the orientation of the field. For fields applied in the x-direction, electron spin states are thus characterized by  $|\pm 1/2\rangle_x$ . In GaAs-QWs, the electron spin states exhibit a Zeeman splitting, which scales linearly with the applied field<sup>12</sup>. The electron g-factor  $g_e$  depends sensitively on the degree of confinement and thus on the well-width and the Al-concentration in the barriers<sup>55</sup>.

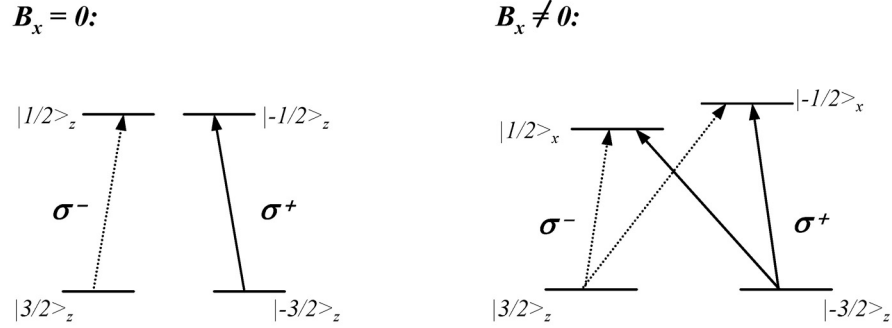


**FIGURE 12:** Effects of in-plane magnetic fields on the HH1-exciton level structure (single-particle picture). The zero-field case is shown on the left. In Voigt geometry, the CB electron spins line up with the externally applied field giving rise to a Zeeman splitting. For weak enough fields, the hole spins remain pinned along the growth direction as effects of spin-orbit coupling dominate.  $J_z$  remains a good quantum number and Zeeman splitting of the heavy-hole states is negligible.

Effects of in-plane magnetic fields on the VB-states are more subtle as the perturbation introduced by the magnetic fields can lead to mixing of HH1 and LH1 states, if the applied fields are strong enough to overcome effects of spin-orbit coupling<sup>56</sup>. For the field strengths and QW-samples considered here, mixing of HH1 and LH1 states can be neglected. Spin-orbit coupling pins the hole spin along the growth direction and the HH1-states are given by the angular momentum states  $|\pm 3/2\rangle_z$  as for the zero-field case<sup>57</sup>. The HH1-states exhibit almost no Zeeman splitting. In contrast, the Zeeman splitting of the LH1-states far exceeds the Zeeman splitting of the CB-electrons<sup>56</sup>. As a result, the Zeeman splitting of the HH1-exciton in the presence of in-plane magnetic fields is determined by the electron g-factor. The HH1-exciton exhibits in addition a diamagnetic shift. The LH1-exciton shows a Zeeman splitting, which is determined by the splitting of the LH1-states.

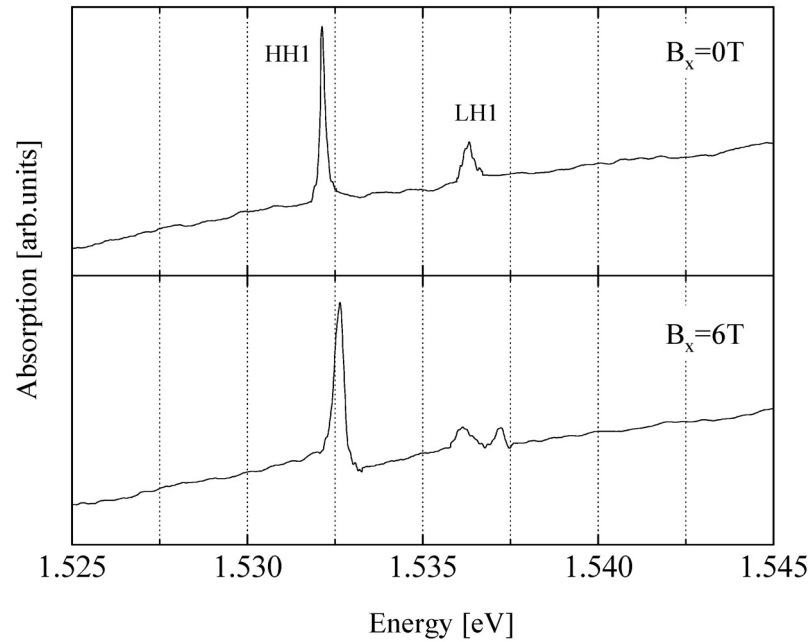


*FIGURE 13: Effects of in-plane magnetic fields on excitonic absorption spectrum. Spectra were obtained from a high-quality single QW-sample (QW2, see Chapter V) exhibiting almost no inhomogeneous broadening..*

Figure 13 shows linear absorption spectra of a high-quality single-QW (QW2 as discussed in Chapter V) for  $B_x = 0$  T and  $B_x = 6$  T. The particular sample was chosen, since inhomogeneous broadening is almost absent in this sample. Zeeman splitting of the excitonic resonances can thus be resolved. As expected, a splitting is revealed for the LH1-exciton resonance. Splitting of the HH1-exciton due to the Zeeman splitting of the electronic states is not resolved but inferred from the broadening of the HH1-resonance. The diamagnetic shift of the HH1-exciton is also revealed. Note that the modifications of the bandstructure lead also to modified optical selection rules as shown in Figure 12. The results can be easily confirmed by expanding the  $|\pm 1/2\rangle_x$  CB-electron spin states in the basis states  $|\pm 1/2\rangle_z$  and by exploiting the known selection rules for the zero-field case. Both CB-spin states are coupled to the same VB-state for co-circular polarized fields.

### Summary

In this chapter, we have provided the background knowledge relevant for an understanding of the nonlinear optical studies on electron spin coherence presented in this dissertation. First, we pointed out that two species of excitons co-exist in GaAs/Al<sub>x</sub>Ga<sub>1-x</sub>As QW-systems as a result of interface fluctuations. Localized excitons form at low temperatures below the HH1-exciton line center, whereas mobile excitons dominate the optical response at and above the HH1-line center. It is well established that relaxation dynamics differ fundamentally for these two types of excitons. In order to discuss the nonlinear optical properties of excitons, we introduced the concept of N-exciton states to include higher-order many-body correlations. The results obtained prepare for a discussion of the nonlinear optical response from excitons within a phenomenological model in which the OBE are applied to N-exciton level schemes. Finally, we discussed the effects of in-plane magnetic fields on the excitonic level structure. Due to the absence of spin-orbit coupling for the CB, electron spins line up with externally applied fields giving rise to a Zeeman splitting between the CB-electron spin states. In contrast, spin-orbit coupling governs the hole states for weak enough magnetic fields, and  $J_z$  remains a good quantum number. The resulting modifications of the selection rules give rise to two V-type systems within the HH1-exciton, in which both electron spin states can be coupled to a common VB state via dipole optical transitions. The HH1-exciton level structure in Voigt geometry is thus appropriate for optical manipulation of the non-radiative electron spin coherence and hence for possible demonstrations of EIT.

## CHAPTER IV

ELECTRON-PHONON INTERACTIONS AND DIPOLE DEPHASING IN  
SEMICONDUCTOR QUANTUM DOTS

Resonant optical excitations give rise to an upper state population as well as a quantum mechanical coherence in the resonant dipole transition of the excited medium. Relaxation of optical excitations is generally described in terms of energy relaxation and pure dephasing processes, two concepts which have proven extremely useful in atomic and molecular physics. A clear distinction exists between the two mechanisms: whereas real transitions are involved in energy relaxation, occupation of the relevant states is unaffected by pure dephasing. Decay of the excited state population is thus solely caused by energy relaxation. In contrast, energy relaxation and pure dephasing processes both contribute to the loss of quantum mechanical coherence. In semiconductors, electron-phonon interactions, which couple the electronic system to the lattice vibrational modes of the crystal, play a dominant role for both of these relaxation mechanisms. For resonant optical excitation of band-edge excitons, the optical polarization is intricately related to excitonic coherences. Dephasing of the macroscopic optical polarization, i.e. the loss of a well defined phase relationship between the external electromagnetic field and the optical polarization it induces, reflects thus fundamental microscopic processes associated with excitonic decoherence. QDs provide a new and exciting laboratory system, which allows to explore the effects of confinement on electron-phonon interactions and thus on the coherent optical properties.

Relaxation of optical excitations in QDs differs fundamentally from that in the bulk. First, as a result of the discrete electron- and in some cases phonon- DOS in QDs, energy relaxation via

electron-phonon scattering is expected to be suppressed (phonon bottleneck)<sup>58</sup>. The observation of efficient band-edge luminescence in most QD-systems, however, has shown that the phonon bottleneck is virtually inoperative. Second, the constraint of crystal momentum conservation is relaxed as the translational symmetry is broken in QDs. In contrast to the bulk case, pure dephasing processes are thus expected to be of increased importance. Finally, photo-excited electron-hole pairs are strongly localized within the confines of a QD. The increased spatial overlap of electron and hole wavefunctions could thus lead to effective charge neutrality of electron-hole pairs. It has been argued that as a result, polar coupling mechanisms, such as Fröhlich coupling to optical-phonons are significantly reduced in QDs<sup>8</sup>. The confinement induced modifications of electron-phonon interactions, which can in principle lead to suppression of dipole dephasing via electron-phonon interactions and thus ultralong decoherence times, are at the heart of the current interest to use QDs for applications in quantum information.

In this chapter, we review results of experimental and theoretical studies pertinent to a discussion of the homogeneous linewidth in CdSe-QDs. Three topics are emphasized: energy relaxation and the role of dark excitons, confinement induced modifications of electron-phonon interactions, and spectral diffusion.

#### Energy relaxation: the role of dark excitons

As a result of the confinement induced enhancement of the exchange interaction, semiconductor QDs are ideal candidates for investigations of the intrinsic dark exciton. As shown in Chapter II, the dark exciton constitutes the lowest energy state within the manifold of the band-edge exciton in CdSe-nanocrystals. Smaller species of CdSe-nanocrystals can feature bright-dark splittings  $\Delta$  as large as 10meV exceeding that in bulk by two orders of magnitude. Evidence for the intrinsic dark exciton in CdSe nanocrystals has been found in time-resolved photoluminescence

(TR-PL)<sup>59</sup>. Note first, that in bulk CdSe, the band-edge luminescence shows decay times on the order of 1 ns<sup>60</sup>. Emission occurs from the bright exciton, which is thermally populated even at temperatures < 10 K as a result of the small exchange splitting in the bulk. In contrast, the low-temperature PL from CdSe-nanocrystals feature a highly non-exponential decay in TR-PL with a long-tail in the  $\mu$ s-range<sup>61</sup>. More recent magneto-PL studies infer that the long-lived component in TR-PL is due to radiative recombination from the intrinsic dark exciton<sup>27,59</sup>. Furthermore, measurements of the resonant Stokes shift using fluorescence line narrowing (FLN) strongly infer that the first bright exciton state  $|1\rangle^L$  acts as the absorbing transition, whereas emission occurs from the intrinsic dark state  $|2\rangle^{27,59}$ . In addition, calculations of the band-edge exciton within a tight-binding approach yield  $\mu$ s-lifetimes for the intrinsic dark state in good agreement with experimental results obtained<sup>62</sup>. Note that in addition to the intrinsic dark exciton, which affects the band-edge luminescence from CdSe-nanocrystals as discussed, extrinsic effects associated with surface traps can determine the photo-physical behaviours of QDs<sup>63</sup>. Surface traps are responsible e.g. for fluorescence blinking observed in CdSe-nanocrystals. Surface traps as extrinsic dark states can significantly alter the relaxation dynamics of optical excitations in QD-systems. Therefore, effects of intrinsic as well as extrinsic dark states, if present, have to be taken into account in a discussion of the relaxation dynamics of optical excitations in QD-systems.

#### Electron-phonon interactions in quantum dots

As a result of the confinement induced modifications of electronic and lattice vibrational wavefunctions, electron-phonon interactions in QDs are modified with respect to the bulk. The electronic level structure in QDs has been discussed in Chapter II. Here, we are concerned with the confinement induced modifications of lattice vibrational modes and the combined effects of electron- and phonon- confinement on electron-phonon interactions in QD-systems.

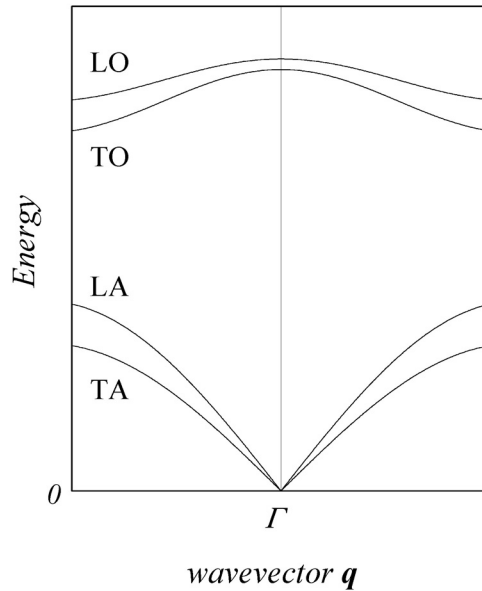


**FIGURE 14.** *Generic phonon dispersion in a polar diatomic crystal such as GaAs or CdSe.*

In diatomic crystals such as GaAs or CdSe, lattice vibrational modes are characterized by three acoustic- and three optical- phonon branches as shown in a generic phonon dispersion in Figure 14. Depending on whether the lattice displacement is parallel/orthogonal with respect to the propagation vector of the lattice distortion, phonons are further specified as longitudinal or transverse modes (longitudinal/transverse acoustic phonons (LA/TA) or longitudinal/transverse optical phonons (LO/TO)). Acoustic phonons correspond to relative displacements  $\mathbf{u}_{ac}(\mathbf{r})$  of entire crystal unit cells with respect to each other; optical phonons are associated with relative displacements  $\mathbf{u}_{op}(\mathbf{r})$  of the cation (Ga/Cd) with respect to the anion (As/Se) within a unit cell. In QDs, both acoustic- and optical- phonons can be subject to effects of zero-dimensional confinement. Confined acoustic phonons form typically in ‘free-standing’ QDs such as semiconductor nanocrystals, which are embedded in matrices (glass/polymers/solution, etc.) with significantly different elastic constants. In this case, discrete acoustic phonon modes can result

due to resonant reflections of acoustic waves at the mismatched dot/matrix interface. In contrast, most epitaxially grown dots are embedded in host materials with similar elastic constants. Carriers confined in epitaxially grown QDs couple thus typically to the continuum of lattice vibrational modes defined by the entire structure.

Calculations of the spectrum of confined acoustic phonon modes in nanocrystals generally follow Lamb's theory on the vibrational modes of a continuous sphere<sup>64</sup>. Effects of confinement are introduced via boundary conditions. Two illustrative cases, 'free' and 'rigid' boundary conditions, corresponding to vanishing normal force and vanishing displacement on the nanoparticle's surface respectively, are typically considered. Examples for free/rigid boundary conditions are nanocrystals embedded in polymer/glass. In a continuum model, the acoustic phonon displacement obeys the Navier equation. Introducing a scalar field  $\phi$  and a vector field  $\vec{\Phi}$ , and separating the harmonic time dependence, allows to write the spatial part of the displacement field as<sup>65</sup>:

$$\vec{u}_{ac}(\vec{r}) = -\left(\frac{v_t}{\omega}\right)^2 \vec{\nabla} \phi + \left(\frac{v_l}{\omega}\right)^2 \vec{\nabla} \times \vec{\Phi} \quad (4.1)$$

with  $\phi$  and  $\vec{\Phi}$  respectively obeying the Helmholtz equation:

$$\Delta \vec{\Phi} + \left(\frac{\omega}{v_t}\right)^2 \vec{\Phi} = \vec{0} \quad (4.2)$$

$$\Delta \phi + \left(\frac{\omega}{v_l}\right)^2 \phi = 0$$

The acoustic phonon spectrum  $\omega_{ln}$  is given by the eigen-values of Eq.(4.2) and appropriate boundary conditions. As a result of the spherical symmetry assumed in the model, acoustic phonon eigen-modes and eigen-frequencies are labelled by an angular momentum  $l$ , angular momentum projection  $m$ , and a radial quantum number  $n$  ( $l,m,n$ ) (eigen-frequencies  $\omega_{ln}$  are

degenerate with respect to  $m$ , which is hence omitted in the notation). As expected from a simple standing-wave type argument, the resonant frequencies of confined acoustic phonon modes exhibit a generic  $1/R$ -dependence, where  $R$  denotes the dot radius.

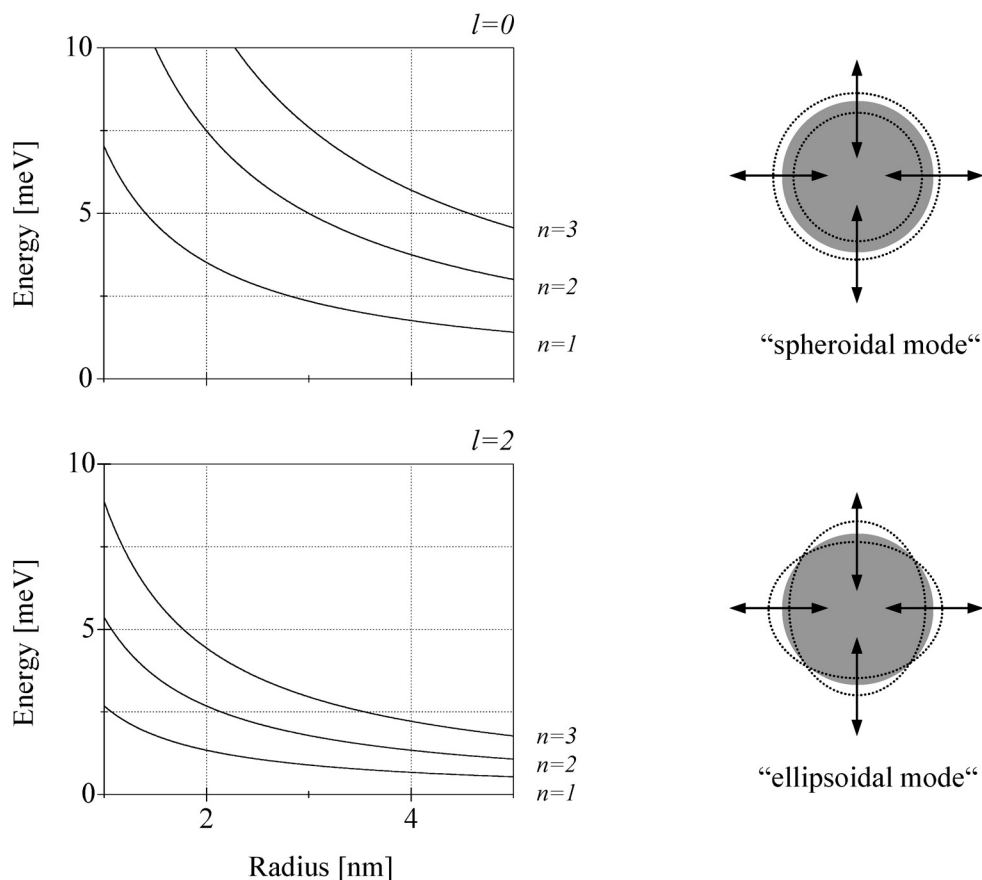


**FIGURE 15.** Size dependence for the first three 'spheroidal' ( $l=0$ ) and 'ellipsoidal' ( $l=2$ ) confined acoustic phonon modes in a CdSe-nanosphere and for free-boundary conditions.

Material specific properties enter the expression for the resonant frequencies via the transverse  $v_t$  and longitudinal  $v_l$  speed of sound in the dot material. Here, we provide explicit results for spherical CdSe QDs and 'free' boundary conditions for the first three 'spheroidal'  $l=0$  and 'ellipsoidal'  $l=2$  modes<sup>65</sup>:

$$\begin{aligned}
E_{n,l=0} [meV] &= S_{n,l=0} v_l / 2R [nm] & S_{n,l=0} \times 10^3 &= 3.81, 8.11, 12.32 \quad (n=1,2,3) \\
E_{n,l=2} [meV] &= S_{n,l=2} v_l / 2R [nm] & S_{n,l=2} \times 10^3 &= 3.48, 6.96, 11.51 \quad (n=1,2,3)
\end{aligned} \tag{4.3}$$

The averaged sound speeds  $v_l=1.54 \times 10^3$  m/s and  $v_l=3.7 \times 10^3$  m/s are used. Note that the  $l = 0, 2$  modes are the only Raman active modes. The results of Eq.(4.3) are plotted in Figure 15. A treatment similar to the one discussed here for acoustic phonons can be carried out to account for effects of confinement on optical phonons<sup>66</sup>. Once electron and lattice vibrational wavefunctions are known, electron-phonon coupling strengths can be calculated for the particular coupling mechanisms, which are now discussed.

Electron-phonon interaction mechanisms are generally divided into deformation potential coupling (DP) and polar coupling mechanisms. DP coupling results from lattice distortions associated with acoustic vibrations, which are adiabatically changing the crystal potential, and thus the electronic band-gap. The dominant term in DP coupling is directly proportional to the strain tensor<sup>67</sup>:

$$H_{DP} \sim D_{e/h} \vec{\nabla} \cdot \vec{u}_{ac}(\vec{r}) \tag{4.4}$$

The electron/hole deformation potential coupling constants  $D_{e/h}$  define the strength of the interaction. Note that the expression in Eq.(4.4) gives rise only to coupling with LA phonons. In contrast to DP coupling, polar coupling mechanisms are based on electrostatic interaction and as a result occur only in polar crystals as GaAs or CdSe. In polar crystals, lattice strains associated with acoustic vibrations are generally accompanied by a macroscopic polarization. This polarization can interact with the electric field produced by an electron and leads to piezoelectric (PZ) coupling. Similarly, the polarization associated with optical phonons gives rise to coupling

of electrons to longitudinal optical (LO) phonons via Fröhlich interaction. Both polar interaction mechanisms are described by the same generic expression<sup>67</sup>,

$$H_{polar} \sim \int d^3r \nabla_r \left( \frac{1}{|\vec{r} - \vec{r}_e|} \right) \vec{P}(\vec{r}) \quad (4.5)$$

The polarization  $\mathbf{P}(\mathbf{r})$  in Eq.(4.5) is associated with LA/TA phonons in the case of PZ coupling and LO phonons in the case of Fröhlich interaction. Given the underlying coupling mechanism, PZ coupling and Fröhlich interaction are expected to increase with increasing ionicity of the crystal. Based on this simple argument one may ask whether dipole dephasing in II-VI based QDs is enhanced over dephasing in III-V based QD-systems as a result of increased polar electron-phonon interactions in II-VI materials. The results of our study on dipole dephasing in CdSe-QD-systems will provide an answer to this question.

Due to the localized nature of their electronic states, QDs are very similar to F-centers in solids with regard to electron-phonon interactions<sup>68,69</sup>. As a result, discussions of electron-phonon interactions in QD-systems have been carried out within the framework and generalizations of models introduced in the context of F-centers<sup>8</sup>. Accounting for the main features, we follow a recent approach based on the independent boson model to discuss electron-phonon interactions and dipole dephasing in QDs<sup>70</sup>. The reader is referred to references 29 and 71 for more general discussions. To model the optical properties and the relaxation dynamics of the ground-state exciton coupled to the lattice vibrational modes of the crystal lattice, the electronic level structure is effectively reduced to a two-level system. Adding resonant electromagnetic fields to the independent boson model, the Hamiltonian describing the dynamics of a QD-exciton coupled to a continuum of phonon modes as well as resonant optical fields is given by<sup>70</sup>:

$$\begin{aligned}
H = & \hbar\Omega a^\dagger a + \sum_{j,\vec{q}} \hbar \left( (g_j^e(\vec{q}) p_{j,\vec{q}} + H.c.) a^\dagger a - (g_j^h(\vec{q}) p_{j,\vec{q}} + H.c.) b^\dagger b \right) \\
& + \sum_{j,\vec{q}} \hbar \omega_j(\vec{q}) p_{j,\vec{q}}^\dagger p_{j,\vec{q}} - (\vec{M} \cdot \vec{E} a^\dagger b^\dagger + H.c)
\end{aligned} \tag{4.6}$$

The operators  $a$ ,  $b$ ,  $p_{j,\mathbf{q}}$  are the electron, hole and phonon annihilation operator respectively. The first term is the Hamiltonian for the electronic system, which in our case is the first bright exciton in CdSe-QDs. The energy  $\hbar\Omega$  denotes the exciton transition energy in the absence of electron-phonon coupling. The second term accounts for electron-phonon interactions in a linear coupling mechanism. Electron-phonon interactions enter via  $g_j^{e/h}(\mathbf{q})$ , which denotes the electron/hole coupling constant for coupling to a particular phonon mode characterized by the phonon branch  $j$  and wavevector  $\mathbf{q}$ . The third term represents the energy of the lattice vibrations. The last term accounts for resonant interaction with optical fields in the dipole approximation. Note that the electron-phonon interaction in Eq.(4.6) is diagonal in the electronic states. Energy relaxation via lattice vibrations is thus not included and the model accounts for pure dephasing of the excitonic transition only. More general calculations taking into account several excitonic states and energy relaxation within these states due to electron-phonon interactions have been carried out using a Green's function approach<sup>71</sup>. The advantage of the Hamiltonian given in Eq.(4.6) is that it can be solved analytically for a number of linear and nonlinear signals<sup>72</sup>. Of interest here is the linear optical polarization  $P(t)$ , which is given by the two-point correlation function defining the excitonic coherence according to  $P(t) = M \langle ba \rangle(t)$ , where  $M$  is the projection of the dipole moment along the applied field. The linear optical polarization induced by a  $\delta$ -like excitation ( $E(t)=E_0\delta(t)$ ) is given by ( $\chi(t)$  is the linear susceptibility)<sup>70</sup>:

$$\begin{aligned} \bar{P}(t) = i\Theta(t) \frac{|M|^2 \vec{E}_0}{\hbar} e^{-(i\Omega' + 1/T_1)t} \times \\ \exp \left[ \sum_{j, \vec{q}} |\gamma_{j, \vec{q}}|^2 \left( e^{-i\omega_j(\vec{q})t} - 1 - 4n_j(q) \sin^2 \left( \frac{\omega_j(\vec{q})}{2} t \right) \right) \right] =: \varepsilon_0 \chi(t) \vec{E}_0 \end{aligned} \quad (4.7)$$

A finite excited state lifetime  $T_1$  has been added by hand in Eq.(4.7). The linear absorption spectrum  $\alpha(\omega) \sim \text{Im}[\chi(\omega)]$ , is obtained from the Fourier transform  $\chi(\omega)$  of  $\chi(t)$ . Electron-phonon interactions lead to a polaron shift in the transition energy:

$$\Omega' = \Omega - \sum_{j, \vec{q}} \omega_j(\vec{q}) |\gamma_{j, \vec{q}}|^2 \quad (4.8)$$

The dimensionless coupling strength is given by:

$$\gamma_{j, \vec{q}} = \frac{g_{j, \vec{q}}^e - g_{j, \vec{q}}^h}{\omega_j(\vec{q})} \quad (4.9)$$

To investigate the effects of electron-phonon interactions on the linear optical response as described by Eq.(4.7) we assume that electron-phonon interactions are absent ( $\gamma_{j, \vec{q}} = 0 \forall j, \vec{q}$ ). Then, Eq.(4.7) gives rise to an exponential decay of the optical polarization, or equivalently a Lorentzian absorption profile with homogeneous linewidth determined by the inverse of the excited state lifetime  $T_1$ . Adding coupling to one particular phonon mode with angular frequency  $\omega_0$ , gives rise to coherent oscillations with period  $\tau = 2\pi / \omega_0$  superimposed onto the temporal decay of the optical polarization ( $\tau < T_1$  is assumed). Note that coherent oscillations due to coupling to optical- as well as acoustic- phonons have indeed been observed in the transient response of QD-systems<sup>73,74</sup>. In the frequency domain, coupling to a discrete set of phonon modes, manifests in the form of discrete sidebands in the optical spectrum. These sidebands arise from phonon-assisted transitions, which in contrast to the zero-phonon-line (ZPL), involve emission or absorption of phonons in the optical process. Phonon sidebands are separated from the zero-

phonon line by integers of the energy of the relevant phonon mode. The connection between electron-phonon interactions and pure dephasing can now be understood by making the transition from a discrete set of phonons to a continuum of phonon modes. As is evident from Eq.(4.7), coupling to a continuum of phonon modes gives rise to an infinite number of phonon sidebands, each at different energy. Spectral integration over the continuum of sidebands arising from acoustic phonons gives rise to a broad resonance, the zero-optical phonon line (ZOPL). In contrast, interaction with LO-phonons gives rise to replicas of the ZOPL. In the time-domain, pure dephasing can be understood as destructive interference arising from the various oscillating terms in Eq.(4.7). As can be seen from Eq.(4.7), the contribution from pure dephasing is determined by three factors: the magnitude of the effective coupling constants  $\gamma_{j,\mathbf{q}}$ , the temperature (via the mean number  $n_j(\mathbf{q})$  of phonons in mode  $(j,\mathbf{q})$  as determined by the Bose-Einstein distribution), and the DOS of phonon modes which enters via the summation in Eq.(4.7).

The results of the independent Boson model are graphically illustrated in Figure16 in terms of a shifted oscillator model. Only one phonon mode is included. In the presence of electron-phonon interactions the true eigen-states of the system are product states of the electronic wavefunctions and the Fock-number states of the harmonic lattice vibrations. Due to the localized nature of the electronic states, the lattice vibrational wavefunctions depend sensitively on the state of the electronic system. In particular, excitation of the electronic system leads to strong distortion of the surrounding lattice, which manifest in a shift of the equilibrium position of the lattice vibrations. As a result phonon-assisted optical transitions become possible as phonon number states associated with the excited electronic state and phonon number states associated with the electronic ground state are no longer orthogonal.

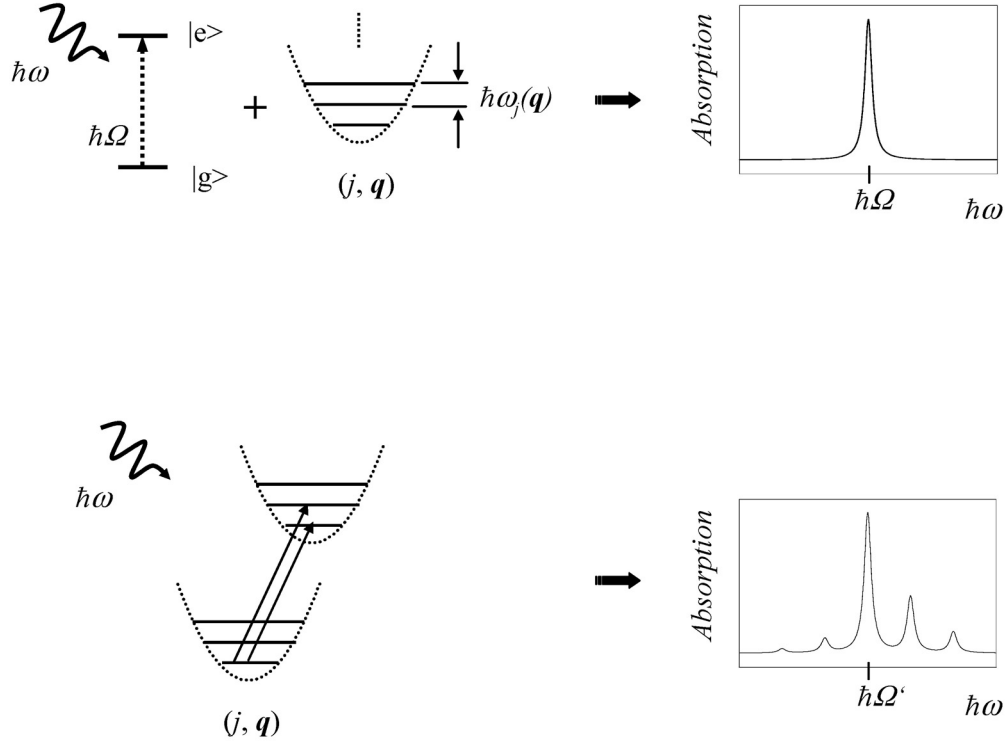


*FIGURE 16. Illustration of the effects of electron-phonon interactions in a shifted oscillator model. Top: limit of vanishing electron-phonon interactions. Bottom: coupled electron-phonon states. In addition to the zero-phonon-line (ZPL), phonon replicas appear as Stokes and anti-Stokes sidebands.*

Explicit numerical calculation of the linear absorption, requires knowledge of the coupling constants. The electron/hole coupling constants  $g_j^{e/h}(\mathbf{q})$  in Eq.(4.6) are given by the corresponding bulk coupling constants  $G_j^{e/h}(\mathbf{q})$ , weighed by a form factor  $F^{e/h}(\mathbf{q})$ , which accounts for the finite extent of electron and hole wavefunctions in a QD. The form factor is the Fourier transform of the electron/hole probability density in real space<sup>70</sup>. Consequently, the form factor gives rise to preferential coupling to phonons, which crystal momentum is on the order of the inverse of the electron/hole localization length, i.e. on the order of the dot radius:

$$g_j^{e/h}(\vec{q}) = G_j^{e/h}(\vec{q}) F^{e/h}(\vec{q}) \quad (4.10)$$

$$F^{e/h}(\vec{q}) = \int d^3r |\Psi_{e/h}(\vec{r})|^2 e^{i\vec{q}\cdot\vec{r}}$$

The generic functional dependences of the bulk coupling constants on phonon momentum are given in Eq.(4.11) for different coupling mechanisms<sup>67</sup>. The respective first proportionality in Eq.(4.11) is exact; the second proportionality assumes a flat/linear dispersion for optical/acoustic phonons, which is justified near the Brillouin center. Note that this is the regime of interest as the form factor restrains coupling to phonons near the  $\Gamma$ -point.

$$G_{LO}^{e/h}(\vec{q}) \sim \frac{\omega_{LO}(\vec{q})}{q} \sim \frac{1}{q}$$

$$G_{DP}^{e/h}(\vec{q}) \sim \frac{q D_{LA}^{e/h}}{\sqrt{\omega_{LA}(\vec{q})}} \sim \sqrt{q} D_{LA}^{e/h} \quad (4.11)$$

$$G_{PZ}^{e/h}(\vec{q})|_{LA/TA} \sim \frac{1}{\sqrt{\omega_{LA/TA}(\vec{q})}} \sim \frac{1}{\sqrt{q}}$$

The effective coupling strength that enters Eq.(4.7) is that of an electron-hole pair confined to a QD; it is given by the difference of the individual electron/hole coupling constants (see Eq.(4.9)). Note that for polar interaction mechanisms, which depend on the particle's charge, electron/hole coupling constants have the same magnitude. As a result, PZ coupling and Fröhlich interaction scale with the spatial overlap of electron and hole wavefunctions. Based on this observation, it has been previously argued that polar coupling strengths can be significantly reduced in QDs<sup>8</sup>. In contrast, the magnitude of DP coupling is different for electrons/holes. Thus, even if electrons and hole wavefunctions perfectly overlap, DP coupling can be operative. As a result of the sensitivity of the electron-phonon coupling strengths in QDs to the electronic wavefunctions, quantitative theoretical results rely on accurate knowledge of the electronic wavefunctions, i.e. band structure-parameters (effective masses and band-gap discontinuities) and dot morphology.

### Spectral diffusion in quantum dots

Similar to molecular systems, QDs have shown to exhibit temporal fluctuations in the transition energy of their optical transitions, i.e. spectral diffusion<sup>75</sup>. The presence of spectral diffusion in QD-systems demonstrates the sensitivity of QDs as mesoscopic systems to fluctuations in the dot environment. Spectral diffusion has been observed in various QD-systems, for different material systems (III-V and II-VI) and growth techniques (chemical synthesis, molecular beam epitaxy, atomic layer epitaxy) and presents thus a rather characteristic feature<sup>9,76,77,78,79</sup>.

The origins of spectral diffusion in QDs have been linked to electric field fluctuations in the microscopic local dot environment, causing fluctuating Stark shifts of the optical transition. Origins of the electric fields themselves may differ for different QD-systems and are not fully understood. In self-assembled QDs, fluctuating electric fields could arise from fluctuating strain fields, which are typically present in these lattice mismatched systems. In contrast, electric field fluctuations in semiconductor nanocrystals have been attributed to carrier trapping following photo-excitation<sup>80</sup>. Carrier trapping causes also the fluorescent blinking behaviour observed in semiconductor nanocrystals. Fluorescence blinking denotes a random flickering between 'on'-states in which the dot emits, and 'off'-states in which the dot does not emit (dark). The 'off'-state corresponds to a state in which a photo-excited carrier is trapped, preventing radiative recombination until the ejected carrier is re-captured. The recently observed correlation between fluorescence blinking and spectral diffusion in single CdSe nanocrystals strongly suggests that spectral diffusion results from a redistribution of local electric fields, which accompanies the QD charge blinking<sup>81</sup>. Note that in this photo-ionization model, spectral diffusion is a light-induced process.

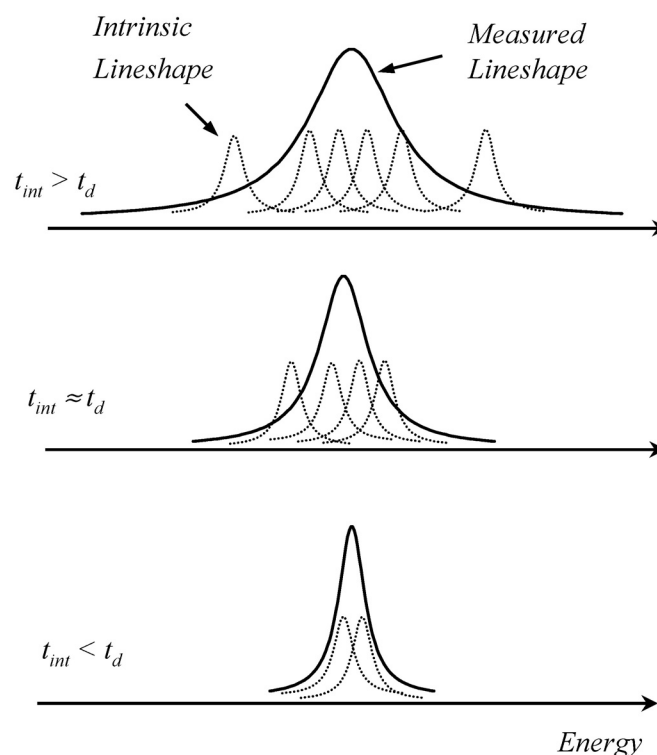


*FIGURE 17. Effects of spectral diffusion. Dotted curves indicate ‘instantaneous spectra’. Solid curves represent the measured spectra resulting from time averaging in the measurement. In order to suppress effects of spectral diffusion the integration time in the measurement has to be shorter than relevant diffusion time scales. Only then, the intrinsic line is measured.*

Spectral diffusion can complicate measurements of the intrinsic homogeneous linewidth, if the frequency excursions associated with spectral diffusion are larger than the intrinsic homogeneous linewidth and if diffusion processes occur on a time scale faster than the integration time of the measurement. Then, as shown schematically in Figure 17, the measured linewidth of the optical transition becomes dependent on the integration time  $t_{int}$ ; in order to suppress effects of spectral diffusion, the integration time used in the experiment has to be smaller than relevant diffusion time scales  $t_d$ . Single dot PL studies require relatively long integration times  $>100\text{ms}$  in order to achieve  $\text{SNR} > 1$  and are thus particularly prone to effects of spectral diffusion. While proving

extremely useful in studying spectral diffusion itself, single dot PL studies are unable to suppress effects of spectral diffusion.

### Summary

Possible mechanisms contributing to the homogeneous linewidth of the bright exciton in CdSe-QDs have been discussed. First, we point to a possible energy relaxation mechanism inherent of the particular fine structure associated with the band-edge exciton in CdSe-QDs. Note again the lowest energy exciton in CdSe-QDs is a dark state. Band-edge luminescence from the dark exciton has been observed in CdSe-nanocrystals revealing that the intrinsic dark exciton, in addition to extrinsic dark states associated with surface traps, significantly affects the energy relaxation dynamics.

For a discussion pure dephasing processes, we followed a recent theoretical study based on the independent Boson model. Manifestations of electron-phonon interactions in the optical spectra are evident from three generic features: the ZPL, which is associated with the purely electronic transition; the ZOPL, which is associated with acoustic phonon assisted optical transitions, and LO-phonon replicas. In the calculation presented, the ZPL acquires a finite width as a result of a phenomenologically introduced excited state lifetime. Note that within the independent Boson model and a linear coupling mechanism, electron-phonon interactions do not contribute to broadening of the ZPL.

Finally, effects of spectral diffusion were discussed. Spectral diffusion can prevent measurements of the intrinsic homogeneous linewidth and therefore has to be eliminated experimentally. While effects of spectral diffusion have been eliminated in measurements of the homogeneous linewidth in III-V based QD-systems<sup>3,4</sup>, previous studies on II-VI based QDs have not been able to do so. As a result, experimental studies on dipole dephasing in II-VI based QDs have been controversial.

## CHAPTER V

## SAMPLE DESCRIPTIONS AND EXPERIMENTAL PROCEDURES

Core/shell CdSe/ZnS nanocrystals

The CdSe nanocrystals investigated in this dissertation were grown in house using high-temperature organometallic synthesis. In a first step, nanocrystals were synthesized in a coordinating solvent (TOPO, Tri-n-octylphosphine oxide) using appropriate reagents. Size selective precipitation after growth provided nearly monodisperse ensembles of nanocrystals<sup>82</sup>. For improved surface quality, these ‘bare’ CdSe-nanocrystals were overcoated in a second step with a ZnS shell. Capping of the CdSe cores with inorganic materials such as ZnS has shown considerable improvement in surface quality and thus photostability of core/shell over ‘bare’ nanocrystals<sup>83,84</sup>. After growth, nanocrystals were stored in chloroform to prevent clustering.

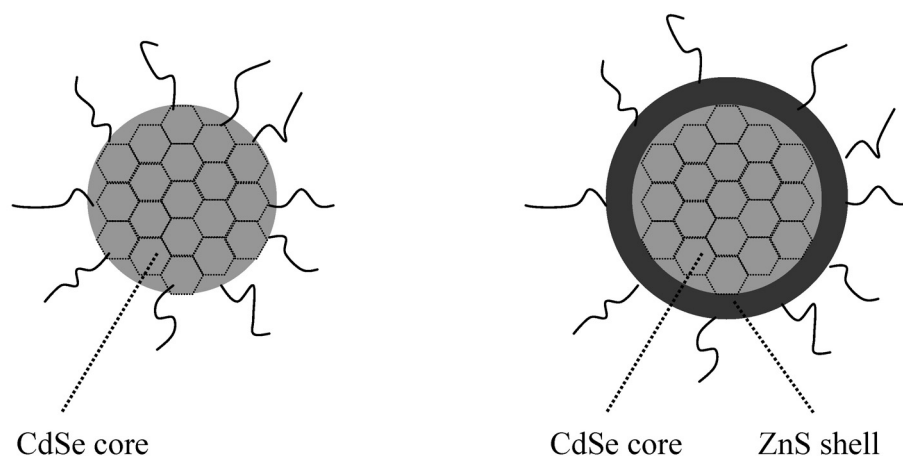


*FIGURE 18. Left: ‘bare’ CdSe nanocrystals. Right: core/shell CdSe/ZnS nanocrystals. The strands represent organic ligands (TOPO). Hexagons represent unit cells of the hexagonal lattice structure.*

Subsequent characterization of the fabricated nanocrystals was carried out using transmission electron microscopy (TEM), PL, and TR-PL<sup>85</sup>. TEM pictures reveal defect free cores and high crystallinity with the wurtzite structure of the parent bulk. Indication of thorough surface passivation is inferred from PL-spectra, which show near unity quantum yield even at room-temperature (RT); no deep trap emission is observed. The RT-PL spectra for the samples used in this study are shown in Figure 19. Mean radii  $R$  of the nanocrystal samples were obtained from TEM and correlated with the RT-PL peak emission of the respective sample providing a rough size calibration (the solid line is a numerical fit with the generic  $1/R^2$ -dependence of the confinement energy:  $E[\text{eV}] = 1.84 - 0.94/(R[\text{nm}])^2$ ). Samples NC1, NC2, NC3, and NC4 are characterized by mean radii of  $R = 4.5, 3.1, 2.4, 2.0$  nm respectively. Size distributions vary from sample to sample and are on the order of 5-10%.

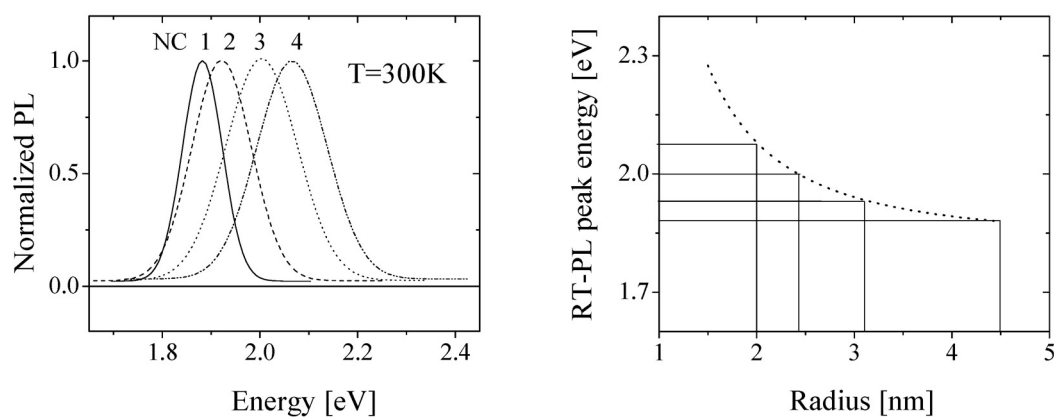


**FIGURE 19.** Left: RT-PL spectra of the samples used. Right: size calibration. Average dot-radii are obtained from TEM graphs and are correlated with the peak of the RT-PL.

Instead of a long microsecond decay in the low-temperature TR-PL as observed for ‘bare’ nanocrystals, the CdSe/ZnS nanocrystals investigated here exhibit a multi-exponential decay, with a dominant contribution from radiative recombination during the first  $\sim 10$  ns<sup>86</sup>. Surface

traps, although still present, are thus significantly reduced thanks to the passivating ZnS-shell. For transmission measurements, small amounts were extracted from the original highly concentrated solution and diluted to the desired concentration by adding chloroform. Polystyrene was added to provide a viscous solution, which was then spin coated onto a sapphire disk to produce smooth films of polymer containing nanocrystals. Unless otherwise mentioned, optical thickness of the films is on the order of  $\alpha L \sim 0.01$  ( $L \sim 100 \mu\text{m}$ ). Using typical nanocrystal absorption cross-sections ( $\sigma \sim 10^{-15} \text{ cm}^2$ ), we obtain a rough estimate for the dot density ( $\sim 10^3/\mu\text{m}^3$ ), corresponding to an inter-dot spacing of  $0.1 \mu\text{m}$ . No degradation of the samples was observed due to illumination and repeated cooling cycles.

#### Self-assembled CdSe/ZnSe quantum dots

The samples investigated here were grown using molecular beam epitaxy (MBE) and were provided by courtesy of Professor Jacek Furdyna<sup>87,88</sup>. While well established for III-V based QD-systems such as InAs/GaAs, controversy remains with regard to the mechanisms involved in self-assembly of CdSe/ZnSe based QDs. Despite their identical lattice mismatch of 7%, effects associated with surface diffusion, bond ionicity and bulk interdiffusion, all of which affect QD formation, can give rise to potential differences in self-assembly of CdSe/ZnSe as opposed to InAs/GaAs QDs. The growth of the CdSe/ZnSe QDs used here shows a sharp transition from layer-by-layer growth to the formation of QD-like islands beyond a certain threshold coverage of CdSe. This transition, characteristic for the Stranski-Krastanow (SK) growth mode, occurs as initially strained two-dimensional layers relax via formation of islands in a highly lattice mismatched system. The onset of island formation of CdSe on [001] ZnSe using MBE occurs at about 2.5-3.0 monolayers of CdSe deposition<sup>87</sup>. Reported dot densities are on the order of  $10-100/\mu\text{m}^2$ . Figure 20, shows a schematic of the epitaxially grown QD-samples. The CdSe-dots are

grown on top of a  $\sim 2 \mu\text{m}$  thick ZnSe buffer, which in turn is grown on a GaAs substrate. A  $\sim 50$  nm thick ZnSe layer is used to cap the CdSe dots in order to prevent dot ripening. For transmission experiments, samples were glued onto a sapphire disk; the substrate was removed using mechanical polishing followed by selective chemical etching.

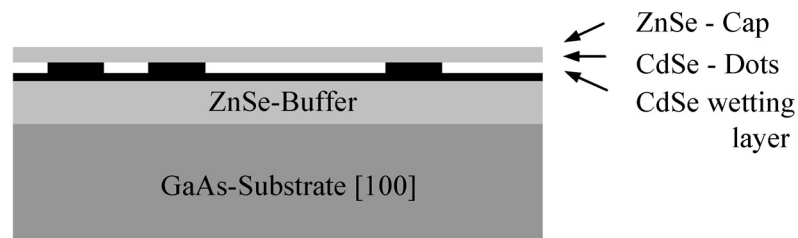


*FIGURE 20. Schematic of the sample structure for MBE-grown self-assembled CdSe/ZnSe QDs. .*

#### GaAs/Al<sub>x</sub>Ga<sub>1-x</sub>As quantum wells

Two different QW-samples were used, both grown by MBE. Sample QW1 is a multiple-QW (MQW) containing 15 periods of 13 nm wide GaAs-wells, separated by 15 nm wide Al<sub>0.3</sub>Ga<sub>0.7</sub>As-barriers. Sample QW2 is a single-QW (SQW) with 17.5 nm wide GaAs-wells and 15 nm wide Al<sub>0.3</sub>Ga<sub>0.7</sub>As-barriers. Another MQW-sample, QW3, grown using metal-organic chemical vapor deposition (MOCVD) was also used to study possible effects associated with sample growth. Sample QW3 contains 8 periods of 13nm wide GaAs-wells and 15 nm wide Al<sub>0.3</sub>Ga<sub>0.7</sub>As-barriers. All samples were obtained from Bell Labs. The samples were glued onto a sapphire disk; mechanical polishing and selective chemical etching were subsequently used to remove the GaAs-substrate to allow for transmission measurements. The low-temperature absorption spectra from sample QW1 and QW2 are shown in Figure 21. Both spectra reveal HH1 and LH1

transition. The HH1 absorption linewidth of 1.8 meV (FWHM) of QW1 reveals inhomogeneous broadening due to well-width fluctuations. Inhomogeneous broadening is almost absent in QW2, which exhibits absorption linewidths of  $\sim 0.6$  meV (FWHM). Previous studies carried out on these samples have confirmed the well known behaviours of exciton localization.

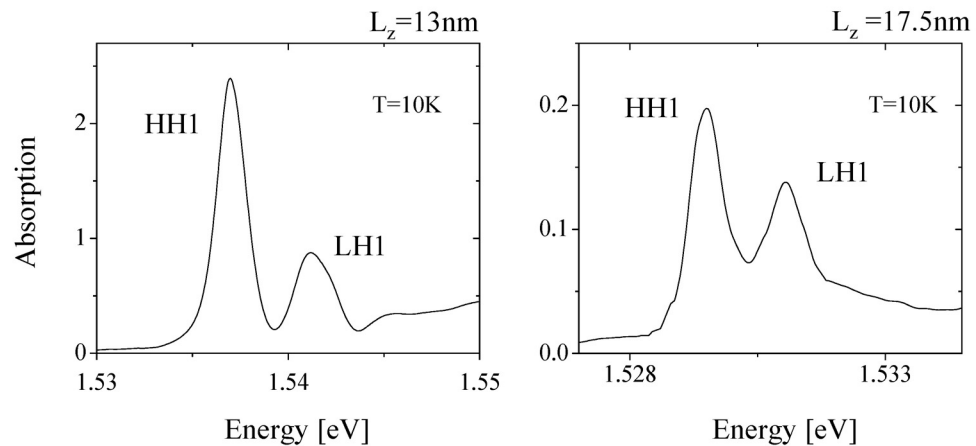


*FIGURE 21. Absorption spectra of the QW-samples used. Left: QW1. Right: QW2. Both spectra show absorption from HH1- and LH1- exciton. Inhomogeneous broadening is almost absent in QW2.*

### High-resolution frequency-domain spectral hole burning

In order to address the deficiencies of previous experiments aimed at measuring the homogeneous linewidth in colloidal and self-assembled CdSe QDs, we developed a novel technique based on spectral hole burning (SHB). SHB-experiments were carried out employing frequency-domain pump-probe spectroscopy. The energy  $E_{\text{pump}}$  of a strong continuous-wave (cw) pump beam was set within the inhomogeneously broadened transition of interest, while the transmission spectrum of a weak cw-probe beam was measured to monitor the changes in the sample absorption induced by the pump (Figure 22). In the SHB-spectrum, we record the normalized differential transmission  $\Delta T/T$  as a function of the pump probe detuning  $\delta = E_{\text{pump}} - E_{\text{probe}}$ .

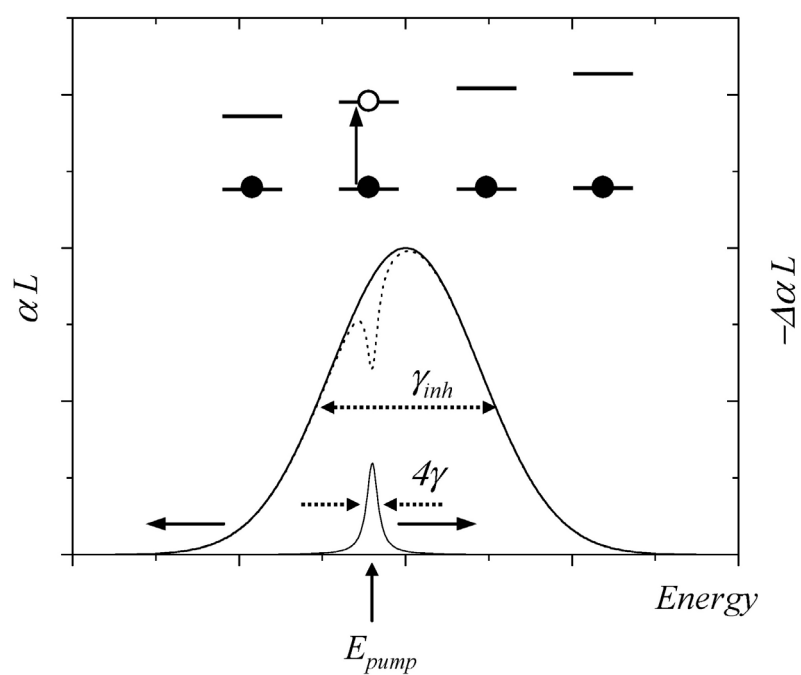
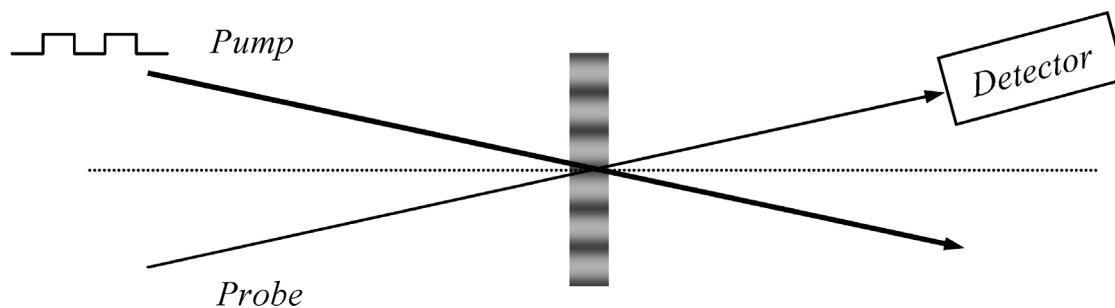


*FIGURE 22. Principle of SHB. The broad solid/dotted line depicts the inhomogeneous absorption profile in the absence/presence of a resonant pump field. The pump gives rise to a spectral hole in the inhomogeneous absorption profile. The difference between the two spectra is measured in the differential absorption spectrum. Only the incoherent contribution, i.e. the spectral hole is shown.*

The normalized differential transmission is the difference between the probe transmission  $T_{\text{on}}$  with the pump beam on, and the probe transmission  $T$  in the absence of the pump, normalized over  $T$ . Applying Beer's law and assuming  $|\Delta\alpha L| \ll 1$ , we obtain:

$$\frac{\Delta T}{T} = \frac{e^{-(\alpha+\Delta\alpha)L} - e^{-\alpha L}}{e^{-\alpha L}} = e^{-\Delta\alpha L} - 1 \approx -\Delta\alpha L \quad (5.1)$$

Thus, we essentially measure the change in absorption  $\Delta\alpha$  induced by the pump. In the following, we discuss the mechanisms giving rise to SHB to third order in the nonlinear optical response for an inhomogeneously broadened collection of two-level systems.

The SHB response comprises a coherent and an incoherent contribution<sup>89</sup>. The incoherent contribution arises from saturation of emitters within the inhomogeneously broadened ensemble, which are resonant with the pump field. Saturation gives rise to a reduced absorption resulting in a spectral hole within the inhomogeneously broadened absorption profile at the pump energy as shown in Figure 22. The spectral hole is revealed in terms of an increased probe transmission at the pump energy. In the third order limit, the spectral hole has a Lorentzian profile with a linewidth given by twice the homogeneous linewidth. The incoherent contribution to the SHB response reveals thus the dipole dephasing time  $T_2$ . The coherent contribution results from wave-mixing of the optical polarization induced by the pump and the electric field associated with the probe. Wave-mixing gives rise to a spatial and temporal modulation of the population inversion, which is referred to as population grating. The pump electric field can diffract off the grating into the probe beam direction within a third order nonlinear optical process giving rise to the coherent contribution<sup>90</sup>. The spatial period  $\Lambda$  and temporal period  $\tau$  of the population grating are respectively given by  $\Lambda = \lambda / (2 \sin(\theta/2))$  and  $\tau = \hbar / \delta$  ( $\lambda$ : pump wavelength;  $\theta$ : angle at which pump and probe field intersect in the sample). Note that the population grating can only follow the beating associated with wave-mixing if the detuning  $\delta$  between pump and probe satisfies  $\delta <$

$\hbar/T_g$ , where  $T_g$  is the grating lifetime. In the third order limit, the coherent contribution gives rise to a ‘coherent spike’ centred around zero detuning with a linewidth given by  $2\hbar/T_g$ . Note that in the absence of spatial diffusion, the grating lifetime is determined by the energy relaxation time of the excited state population  $T_1$ . The coherent contribution to the SHB response can thus provide information on the population relaxation time  $T_1$  and spatial diffusion rates of the optical excitations, if spatial diffusion is present. Note, e.g. that diffusion coefficients for mobile excitons in GaAs-QWs have been determined using a more sophisticated technique based on three-beam FWM<sup>42</sup>.

Third order solution of the OBE for an inhomogeneously broadened ensemble of independent two-level systems is straightforward. The normalized differential transmission as a function of the pump-probe detuning  $\delta = E_{\text{probe}} - E_{\text{pump}}$  is given by (dephasing rate  $\gamma = \hbar/T_2$ ; energy relaxation rate  $\Gamma = \hbar/T_1$ ):

$$\frac{\Delta T}{T} \sim \frac{1}{\gamma\Gamma} \left( \left( 1 + \left( \frac{\delta}{2\gamma} \right)^2 \right)^{-1} + \left( 1 + \left( \frac{\delta}{\Gamma} \right)^2 \right)^{-1} \right) \quad (5.2)$$

where  $\gamma_{\text{inh}} \gg \gamma \gg \Gamma$  ( $\gamma_{\text{inh}}$  : inhomogeneous linewidth) and the absence of spatial diffusion has been assumed. Eq.(5.2) accounts for the incoherent contribution giving rise to the spectral hole (first term), as well as the coherent contribution (second term). Note that close to the lifetime limit characterized by  $\gamma = \Gamma/2$ , one can no longer separate the incoherent from the coherent contribution in the SHB response, i.e. dephasing from energy relaxation<sup>89</sup>.

In order to measure the differential transmission  $\Delta T$  experimentally, phase-sensitive lock-in detection was used. The pump beam intensity was modulated at frequency  $\Omega$  using an acousto-optic modulator (AOM). Two types of measurements were carried out, referred to as degenerate and non-degenerate, depending on whether one or two independent lasers were used to provide

pump and probe. Degenerate or nearly-degenerate measurements provide sub-Hz resolution over a tuning range of a few MHz for ultra-high resolution scans. Non-degenerate measurements provide wide tunability limited by the tuning range of the lasers; spectral resolution depends on operation modes and scanning mechanisms. Non-degenerate measurements were carried out using two tunable cw-ring-dye lasers (Coherent-899, Coherent-699). Kiton Red and Rhodamine 6G were used to cover the relevant wavelength ranges  $\lambda \sim 560\text{-}610\text{nm}$  and  $590\text{-}660\text{nm}$ , allowing for the study of samples NC1-4 and the self-assembled QD-sample. In addition, a NewFocus tunable diode laser was used (tuning range:  $632\text{-}638\text{nm}$ ) for additional measurements on sample NC1. In multi-mode operation, the ring lasers cover the full tuning range of the respective dye gain spectrum with spectral resolution  $\sim 2\text{GHz}$ ; tuning is achieved by adjusting the bi-refrident filter (BRF) inside the laser cavity. Single-mode operation of the ring lasers is achieved using intra-cavity-assemblies (ICA). Stabilization of the ring lasers in single mode operation to their respective reference cavities gives rise to a relative frequency jitter  $\sim 3\text{ MHz}$ , which also determines the spectral resolution in this case. In single-mode operation, reference cavity tuning provides scanning ranges up to  $30\text{GHz}$ . The tunable diode laser, single-mode and mode-hop free provides ease of operation; the laser can be scanned over its entire tuning range using coarse tuning with a resolution of less than  $1\text{ GHz}$ ; fine tuning over  $100\text{ GHz}$  with a step size of  $10\text{ MHz}$  is also provided.

The upper drawing in Figure 23 depicts the generic setup for nearly-degenerate measurements. Pump and probe beam are derived from the same laser. A wavemeter allows to measure the laser output wavelength. Two synchronized RF-generators are used to drive the AOMs. The respective first order beams provide pump and probe. Frequency tuning is achieved by scanning the signal frequency of the RF-generator, which is driving the AOM in the probe beam path. Using this method, effects of laser jitter are eliminated allowing for sub-Hz-resolution<sup>91</sup>.

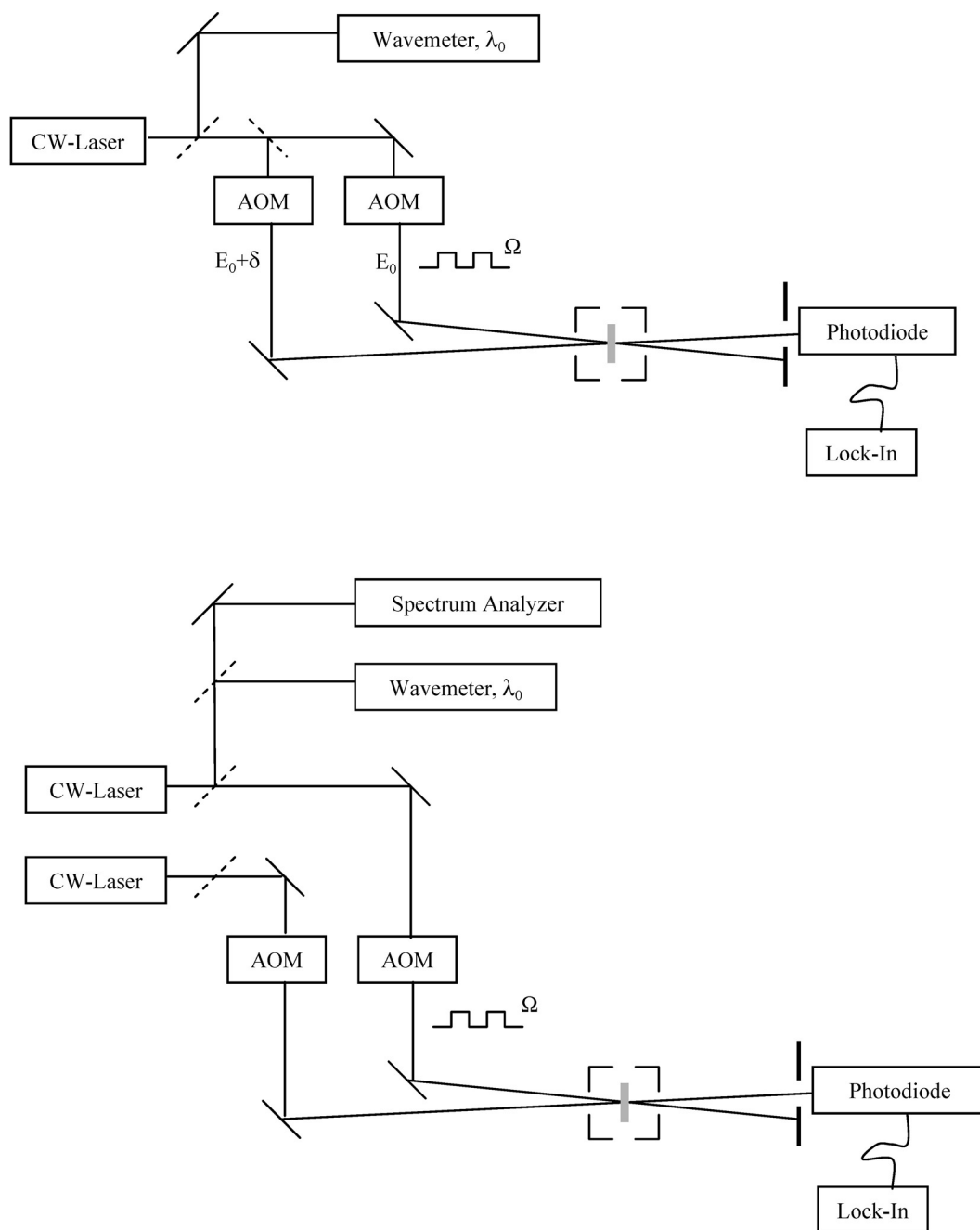


*FIGURE 23. Top/bottom: Experimental setup for degenerate/non-degenerate pump-probe measurements. The wavemeter allows for absolute measurements of the pump/probe wavelength. Using heterodyne beating, a separate spectrum analyzer provides accurate measurement of the pump-probe detuning in the non-degenerate measurements.*

Mixing of the RF-signal driving the AOM in the pump beam path with a TTL-signal of frequency  $\Omega$ , allows to modulate the pump beam intensity with a square waveform at a variable modulation frequency. The lower drawing in Figure 23 shows the setup for non-degenerate pump-probe measurements using two separate laser sources. A spectrum analyzer is used for precision measurements of the detuning, resolution-limited by the relative laser jitter. Adjustment of the RF-power into the AOM provides easy control of pump/probe attenuation. The modulation frequency  $\Omega$  of the pump beam intensity can be tuned variably up to 15MHz, beyond which the AOM response drops significantly. Note that the integration time in the differential transmission measurement is set by the inverse of the modulation frequency  $\Omega$ .

For measurement of the lifetime of the nonlinear optical response, additional studies were carried out using three-beam four-wave-mixing (FWM)<sup>91</sup>. A schematic of the generic setup is shown in Figure 24. In addition to the two fields ( $\mathbf{E}_1$ ,  $\mathbf{E}_2$ ) used in SHB, a third field  $\mathbf{E}_{\text{probe}}$ , counter-propagating with respect to  $\mathbf{E}_1$ , is applied. For measurement of the population lifetime,  $\mathbf{E}_1$  and  $\mathbf{E}_{\text{probe}}$  are degenerate, while the FWM-signal is measured as a function of the detuning of field  $\mathbf{E}_2$  with respect to  $\mathbf{E}_1$  and  $\mathbf{E}_{\text{probe}}$ . Similar to SHB,  $\mathbf{E}_1$  and  $\mathbf{E}_2$  create a population grating; in FWM, the third order nonlinear signal is generated as  $\mathbf{E}_{\text{probe}}$  diffracts off the grating. The FWM signal is thus phase conjugate with respect to  $\mathbf{E}_2$ . The advantage of FWM over SHB is that incoherent and coherent contribution can be, under certain conditions, separately measured and thus distinguished, even if dephasing is close to lifetime limited<sup>92</sup>. In addition, FWM measurements in contrast to SHB are background free. Three-beam frequency-domain FWM, as an extension of SHB, can often provide more information than SHB.

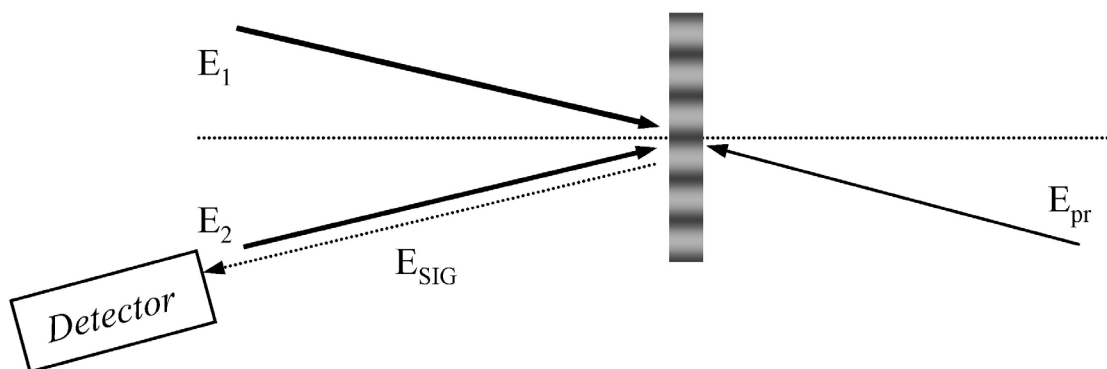


*FIGURE 24. Schematic for three-beam FWM used here for measurements of the SHB-lifetime.*

### Coherent Raman scattering

Similar to the measurement of the SHB response, coherent Raman scattering measurements are carried out using frequency-domain pump-probe spectroscopy. The experimental setup for coherent Raman scattering is thus essentially the same as the one shown in Figure 23 for non-degenerate pump-probe measurements. A Ti:sapphire ring laser (Coherent-899) in single-mode operation (tuning range 760-860nm) provides the pump beam. A NewFocus tunable diode laser (tuning range: 786-816nm) single-mode and mode hop-free allows coarse and fine tuning of the probe beam for low and high-resolution scans as discussed before. In contrast to the dye-lasers used in the SHB study, the Ti:Sapphire ring-laser is not locked to a reference cavity and exhibits thus a slightly broader linewidth. As a result, the relative laser jitter as determined from heterodyne beating is slightly higher and on the order of 10MHz. The relative laser jitter sets the spectral resolution in the experiment. Coherent Raman scattering, in contrast to SHB, probes nonradiative coherences. Similar to the discussion of the SHB response, we now address the coherent Raman scattering response from a collection of non-interacting three-level systems. The

nonlinear optical response is calculated by applying the OBE to the scheme shown in Fig. 25 within a density matrix formalism. We assume that both pump and probe can couple to both dipole transitions. Coherence between the upper to levels can thus be induced optically via the two dipole allowed transitions in a second order process, since both states are coupled to a common ground state.

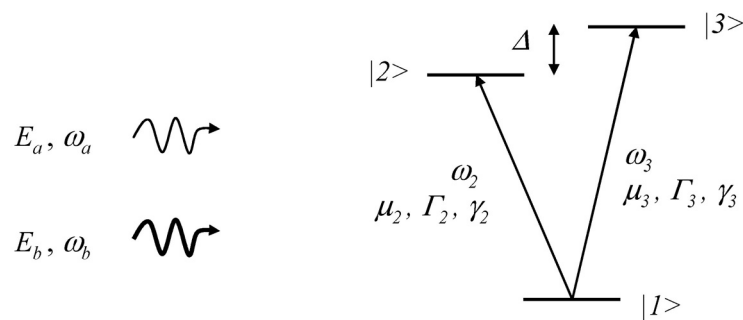


*FIGURE 25. Scenario used to illustrate coherent Raman scattering from a V-type three-level system. The Raman coherence between states  $|2\rangle$  and  $|3\rangle$  can be induced as both states are optically coupled to a common ground state.*

The overall coherent Raman scattering response comprises several contributions. First, two contributions arise from two-level effects associated with the dipole allowed transitions ( $|0\rangle - |1\rangle$ ) and ( $|0\rangle - |2\rangle$ ) as in SHB (incoherent and coherent contribution), if pump and probe act on the same transition. Additional three-level effects can result as will become clear in a discussion of the experimental results. Nevertheless, these contributions are still due to effects related to the dipole coherences. Of interest here is the contribution from the Raman coherence, which is given by the density matrix element  $\rho_{23}$ . Solving the OBE to second order, we obtain:

$$\rho_{23}^{(2)} \propto \left[ \frac{\mu_2 \mu_3 E_a E_b^* e^{i(\omega_b - \omega_a)t}}{(\omega_3 - \omega_2) - (\omega_b - \omega_a) + i\gamma_s} \left( \frac{1}{(\omega_a - \omega_2) + i\gamma_2} - \frac{1}{(\omega_b - \omega_3) - i\gamma_3} \right) \right] + [a \longleftrightarrow b] \quad (5.3)$$

The expression is symmetric with respect to the input fields, demonstrating that the Raman coherence is induced if the pump is resonant with one transition, while the probe is resonant with the respective other transition. The first term in Eq.(5.3) arises if the probe is resonant with transition ( $|1\rangle - |2\rangle$ ), while the pump is resonant with transition ( $|1\rangle - |3\rangle$ ). The second contribution arises if the probe is resonant with transition ( $|1\rangle - |3\rangle$ ) while the pump is resonant with transition ( $|1\rangle - |2\rangle$ ). To third order the contribution from the Raman coherence to the nonlinear optical response  $\sim(\rho_{12}^{(3)} + \rho_{13}^{(3)})$  is given by:

$$\rho_{12}^{(3)} \propto \left[ \mu_2 \mu_3^2 |E_b|^2 E_a^* e^{i\omega_a t} \frac{1}{-(\omega_a - \omega_2) + i\gamma_2} \frac{1}{(\omega_3 - \omega_2) - (\omega_b - \omega_a) - i\gamma_s} \left( \frac{1}{-(\omega_a - \omega_2) + i\gamma_2} + \frac{1}{(\omega_b - \omega_3) + i\gamma_3} \right) \right] \quad (5.4)$$

and  $\rho_{13}^{(3)} = \rho_{12}^{(3)}$  [2 and 3 interchanged]. The expression for the third order response is not symmetric with respect to the input fields since  $|E_b|^2 \gg |E_a|^2$  has been assumed. The expression is however symmetric with respect to the upper states as expected. The effect of the Raman coherence is to generate two resonances in the third order nonlinear optical response, separated by the splitting  $\Delta$  of the upper two states. The linewidth of these Raman sidebands is determined by the decoherence rate  $\gamma_s$  of the Raman transition. In addition to providing information on the non-radiative decoherence rate, coherent Raman scattering allows to study the mechanism involved in the generation of the nonlinear optical response associated with the non-radiative

coherence. This mechanism depends on the system under study and can be quite different from the mechanism which is operative for the generic V-type system shown in Figure 25.

### Quantum beat experiment

Complementary to coherent Raman scattering, time-domain pump-probe measurements were carried out to probe electron spin coherence in GaAs-QWs. Generally, resonant pulsed excitation of a three-level system, in which both dipole allowed transitions are simultaneously addressed, gives rise to a coherent superposition of the system<sup>45</sup>. This requires that the spectral width of the optical pulse exceeds the splitting of the upper states. The pulse can then inject a Raman coherence between the upper two states, which oscillates at frequency  $\Delta/h$  ( $h$ : Planck's constant). Evidence of quantum beats associated with the Raman coherence can be observed e.g. in spontaneous emission from the three-level system. It can be shown in addition, that quantum beats associated with Raman coherence can be observed in the nonlinear optical response. In such measurements, the nonradiative coherence is not only created optically, but it also imposes its signature on the nonlinear optical signal that is detected. The oscillations observed in the optical response present true quantum beats arising from a quantum mechanical superposition, and are not to be confused with polarization beats, which can arise from polarization interference in the sample or interference at the detector<sup>45</sup>.

The quantum beat measurements on electron spin coherence in GaAs-QWs carried out here are based on time-integrated (TI)-pump-probe spectroscopy. In the experiment, we record the differential absorption  $\Delta\alpha L$  ( $\sim\Delta T/T$ ; Eq. (5.1)) as a function of the pump-probe delay<sup>45</sup>. A strong pump field incident at time  $t_0$  injects the electron spin coherence in the QW, subject to a magnetic field applied in Voigt geometry. The evolution of the electron spin coherence is then monitored

by measuring the TI-differential transmission of a probe field arriving at time  $t_1 = t_0 + \tau$  as a function of the pump-probe delay  $\tau$ . Pump and probe pulses are derived from the same laser (mode-locked Ti:Sapphire, Spectra-Physics, “Tsunami”), which emits  $\sim 100$ fs pulses at 82MHz repetition rate. To separate contributions from mobile and localized excitons, we set up an external pulse shaper, which allows to narrow the bandwidth of the laser output to nearly transform limited pulses with  $\Delta\lambda \sim 0.35$  nm and pulse duration  $\Delta t_p \sim 4$  ps. The setup for these degenerate pump-probe measurements is shown in Figure 26. Additional non-degenerate measurements not discussed here, were carried out using one additional spectral filter to control pump/probe spectra independently.

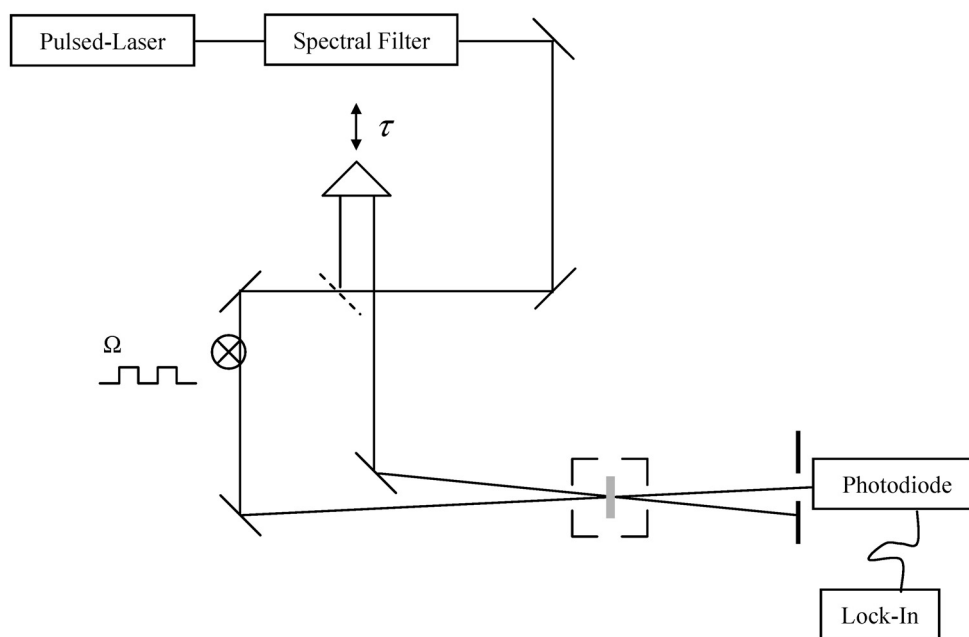


*FIGURE 26. Experimental setup for quantum beat measurements.*

The differential transmission was measured using a photodiode and lock-in detection, which in combination carry out the time integration in the measurement. The pump beam intensity is

modulated using a mechanical chopper. The probe delay could be variably adjusted using a translation stage.

#### Notes on low-temperature measurements

All experiments described above were carried out at low temperature using liquid Helium to cool the samples to desired temperatures. A cold finger cryostat (Janis) was used for measurement above 4.2 K; temperatures as low as 1.8 K could be achieved when pumping at the exhaust port of a Helium flow cryostat (Janis) to reduce the He-vapor pressure.

An Oxford superconducting magnet system (Spectromag SM 4000-8) was used to carry out magnetic field dependent studies on electron spin coherence in GaAs-QWs. Samples were mounted in Voigt geometry. The magnet could be variably ramped to fields as high as 6 T. Preliminary studies were carried out in a cold finger cryostat by attaching a permanent magnet ( $B \sim 0.3$  T) appropriately oriented to the sample holder. Effects related to electron spin coherence could be readily observed in coherent Raman scattering and time-domain pump-probe using this ‘low-tech’ approach. In all measurements, pump and probe fields were focussed onto the samples using far-field optics. Typical focal lengths  $f_{\text{probe}} = 100$  mm-250 mm and  $f_{\text{pump}} \sim 2f_{\text{probe}}$  were used. Appropriate polarization optics allowed for polarization dependent measurements.

## CHAPTER VI

## DIPOLE DEPHASING IN CORE/SHELL CdSe/ZnS-NANOCRYSTALS

The results of our SHB-study on CdSe-nanocrystals are presented. Emphasis is on samples NC1 and NC4, which are respectively the largest ( $R = 4.5$  nm) and smallest ( $R = 2$  nm) species of dots investigated. Unless otherwise mentioned, experiments were carried out at  $T = 10$  K. No significant polarization dependence was observed. This is what we expect, given the random orientation of nanocrystals in the polymer films in which they are embedded (note: the  $c$ -axis defines a preferred direction in the wurtzite crystal structure underlying the CdSe-nanocrystals). Thus, unless otherwise mentioned, cross-linear polarized pump/probe configuration was used to allow for pump scatter rejection and improved signal-to-noise ratios (SNR). Control experiments were carried out with nanocrystals deposited directly on a sapphire disk. Good agreement is obtained with experiments carried out on samples in which nanocrystals are embedded in a polymer host. Due to reduced pump scattering from the polymer films, however, we exclusively present results obtained for nanocrystals embedded in polymer.

Zero-optical-phonon line (ZOPL) and LO-phonon sidebands

In a first step, we measured the nonlinear absorption profile of the ( $1S_{h,3/2} 1S_e$ )-exciton using the setup for degenerate pump-probe measurements. The resulting spectrum is shown for sample NC1 in Figure 27 (bottom) along with the non-resonant PL-spectrum (top). The low-temperature PL shows a blue shift and a narrowing of the inhomogeneous profile with respect to the room-temperature PL as expected due to freeze-out of LO-phonons at low-temperatures<sup>93</sup>. The linewidth of 60 meV (FWHM) obtained from the low-temperature PL-spectrum reveals a size

distribution of  $\sim 6\%$ . The nonlinear absorption profile exhibits the Gaussian lineshape of the PL-spectrum and a similar linewidth. A blue-shift of 10 meV with respect to the PL-spectrum is observed, in fair agreement with previously measured non-resonant Stokes shifts<sup>27</sup> (shift between the linear absorption and non-resonant PL).

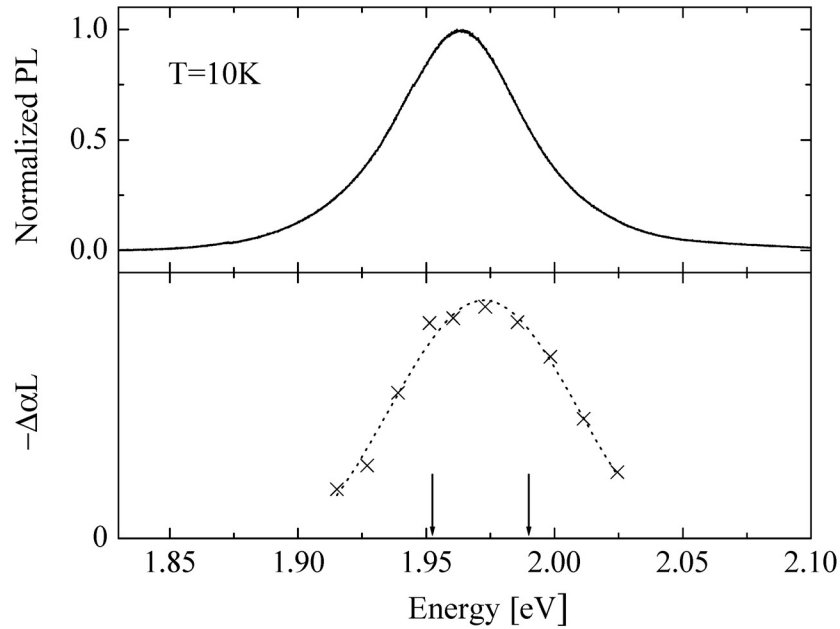


*FIGURE 27. Top/bottom: PL/nonlinear absorption spectrum for sample NC1 at  $T = 10\text{K}$ . Arrows indicate the pump energy positions for the respective SHB-measurements shown in Figure 28.*

Note that the inhomogeneous linewidth exceeds the fine structure splitting within the  $(1S_{h,3/2} 1S_e)$ -exciton. As a result, several dipole allowed transitions within the exciton manifold can in principle contribute to the nonlinear optical signal at a particular energy. To ensure that we are predominantly pumping/probing the first bright exciton  $|\pm 1\rangle^L$  within the  $(1S_{h,3/2} 1S_e)$  manifold, SHB-measurements were carried out with the pump energy set below the peak of the nonlinear absorption profile of the respective sample. For the dot concentrations ( $\sim 10^3/\mu\text{m}^3$ ) and the excitation levels (few  $\text{W}/\text{cm}^2$ ) used,  $|\Delta\alpha L|$  is on the order of  $10^{-4}$ . Throughout the remainder of

this chapter, the SHB-response ( $\Delta T/T$ ) is plotted on a linear scale. Experiments are carried out within the  $\chi^{(3)}$ -regime.

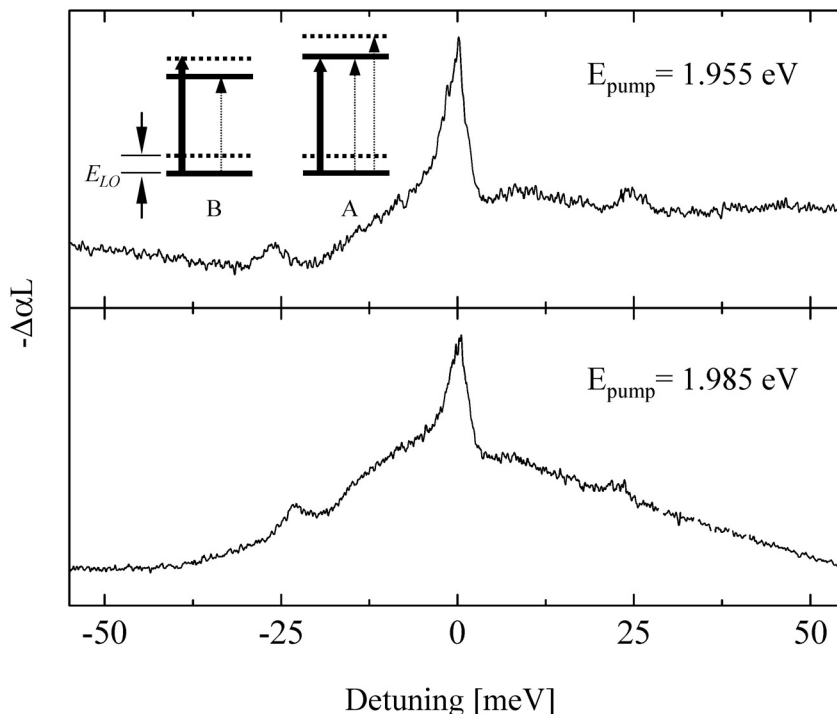


*FIGURE 28.* SHB-spectra from sample NC1 for two different pump energies set within the inhomogeneously broadened absorption of the  $(1S_{3/2} 1S_0)$ -exciton ( $\Omega = 2\text{kHz}$ ). Pump energy positions are indicated by arrows in Fig. 27. The ZOPL and LO-phonon sidebands are clearly observed in both spectra.

Figure 28 shows two SHB-spectra obtained for sample NC1 with the pump energy set below and above the peak of the inhomogeneously broadened nonlinear absorption profile as indicated by the arrows in Figure 27. As the sample absorption is too weak to be accurately measured ( $\alpha L < 0.5\%$ ), the differential transmission spectra were normalized with respect to the incoming laser spectrum rather than the sample transmission. The featureless background reflects thus at most effects of the smoothly varying DOS across the inhomogeneous profile not accounted for in the normalization carried out here. Note that optically thin samples were used to minimize effects

related to inter-dot energy transfer<sup>94</sup>, effects of which were observed in a dot-density dependent study of the SHB-response not discussed here. The following features are evident from both spectra shown in Figure 28. First, a resonance at zero detuning with FWHM  $\sim 4$  meV and asymmetric lineshape, exhibiting a longer tail at negative detuning. Second, two sidebands at positive and negative detuning for  $|\delta| = 25$  meV. Comparison with the energy  $E_{LO}$  of the bulk LO-phonon unambiguously reveals that these sidebands arise from LO-phonon-assisted optical transitions. Surprising is the appearance of LO-phonon sidebands at negative *and* positive detuning at low-temperatures. Note that in the linear absorption, LO-phonon assisted optical transitions are typically revealed as Stokes/anti-Stokes sidebands arising from emission/absorption of LO-phonons accompanying the optical transition. The respective spectral weight of Stokes and anti-Stokes sideband reflects thus thermal occupation of the LO-phonon modes and anti-Stokes lines are absent for  $kT \ll E_{LO}$ . As LO-phonons are frozen out at 10 K, the sidebands observed in the nonlinear absorption as shown in Figure 28 must arise from optical transitions assisted by emission of LO-phonons. Emission of LO-phonons can indeed give rise to LO-phonon sidebands at positive *and* negative detunings in the SHB-response, because the inhomogeneous linewidth exceeds the LO-phonon energy. The inset in Figure 28 depicts relevant mechanisms contributing to the LO-phonon sidebands. Since  $E_{LO}$  is smaller than the inhomogeneous linewidth, note that the pump can select two species of dots out of the inhomogeneous collection of nanocrystals. For dots ‘A’, the pump is resonant with the zero-phonon-transition. A change in the probe absorption results thus at the pump energy, and one-LO phonon energy above it, giving rise to the LO-phonon sideband at positive detuning. For the smaller dots of type ‘B’, the pump is resonant with an LO-phonon assisted transition. A change of the probe absorption one LO-phonon energy below the pump energy results as the probe is resonant with the zero phonon transition of dots ‘B’. Thus a sideband results at negative detuning.

The linewidth of the resonance at zero detuning is on the order of acoustic phonon energies. Similar to LO-phonons, acoustic phonons can assist optical transitions and lead to sidebands in the linear and nonlinear optical response. The spectral feature at zero detuning results from a continuum of acoustic phonon assisted transitions and is referred to as the zero-optical-phonon-line (ZOPL). In contrast to LO-phonons, low-energy acoustic phonons can be thermally excited at 10K. Emission and absorption of acoustic phonons can thus contribute to the ZOPL. This is evident from the asymmetric lineshape of the ZOPL. The ZOPL, in particular the one obtained for  $E_{\text{pump}} = 1.955$  eV, shows a sharp resolution limited feature at zero detuning, which will be addressed in the next section.

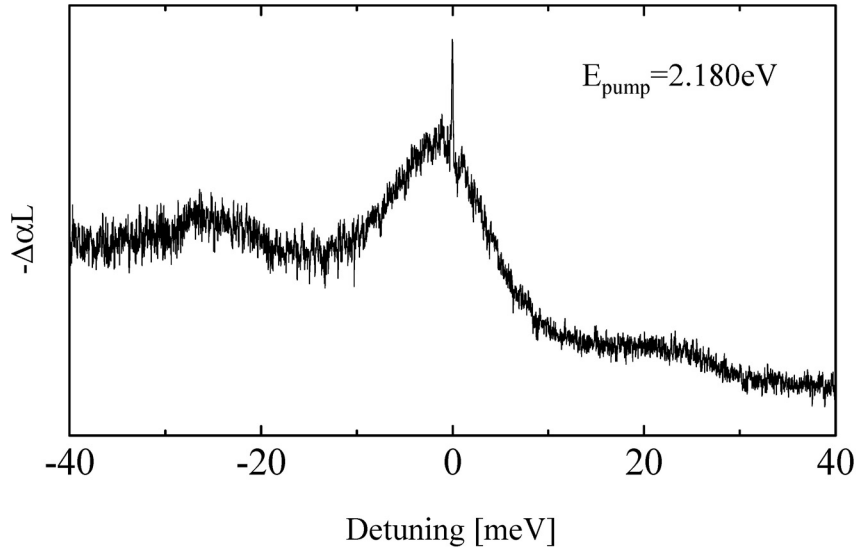


*FIGURE 29. SHB-spectrum from sample NC4 ( $\Omega = 2\text{kHz}$ ). ZOPL and LO-phonon sidebands are significantly broader than those observed for sample NC1. The ZPL is resolved.*

The linewidth of the ZOPL is expected to be correlated with the dot radius due to the form factor, which leads to preferential coupling to acoustic phonons with wavevectors  $|k| \sim 1/R$  as discussed in Chapter IV. Coupling occurs thus to acoustic phonons close to the Brillouin zone center, for

which the acoustic phonon dispersion is linear. An inverse relationship between the ZOPL linewidth and the dot radius is expected on these grounds. Figure 29 shows the SHB-spectrum for sample NC4 ( $R = 2.0$  nm). A sharp resonance is resolved at zero detuning. As we will see, this resonance is also present in sample NC1 and all other sample considered, however, not entirely resolved in the spectra shown in Figure 28. The feature corresponds to the zero-phonon-line (ZPL) and will be discussed in detail in the next section. In addition to the ZPL, ZOPL and LO-phonon sidebands are observed as for sample NC1. Both features, however, are significantly broader than in sample NC1. The ratio of the ZOPL-linewidth obtained from sample NC4 and NC1 is  $\sim 2.5$  in good agreement with the ratio of the inverse dot radii (2.25) confirming our expectation. The SHB-spectra for NC1 and NC4 indicate furthermore, that the linewidth of the LO-phonon sidebands reproduces that of the ZOPL in the respective sample. It is inferred that LO-phonon sidebands arise in fact from a multi-phonon process, which, in addition to optical phonons, does also involve acoustic phonons. This confirms recent theoretical calculations, in which the linewidth of the LO-phonon sidebands has been calculated perturbatively including one-phonon processes only, and exactly within the independent boson model. Broadening of the LO-phonons sidebands in the calculations occurs only if multi-phonon processes are taken into account<sup>70</sup>.

Figure 30 presents a temperature dependence of the SHB-spectra for sample NC1. The ZOPL exhibits spectral broadening with increasing temperature. ZOPL and LO-phonon sidebands begin to merge around 60 K. Note, that the measured spectra are the frequency-domain analogue of a previous three-pulse photon echo study, in which coherent oscillations from LO-phonons have been observed<sup>73</sup>. While suppression of the LO-phonon quantum beats was necessary to separate dephasing due to acoustic phonons in this previous study, the SHB-study here reveals directly in

the frequency-domain the linewidth of the ZOPL. The series of SHB-spectra demonstrates that coupling to acoustic phonons dominates dipole dephasing in CdSe nanocrystals at low temperatures and provides a measure of the temperature broadening of the ZOPL.

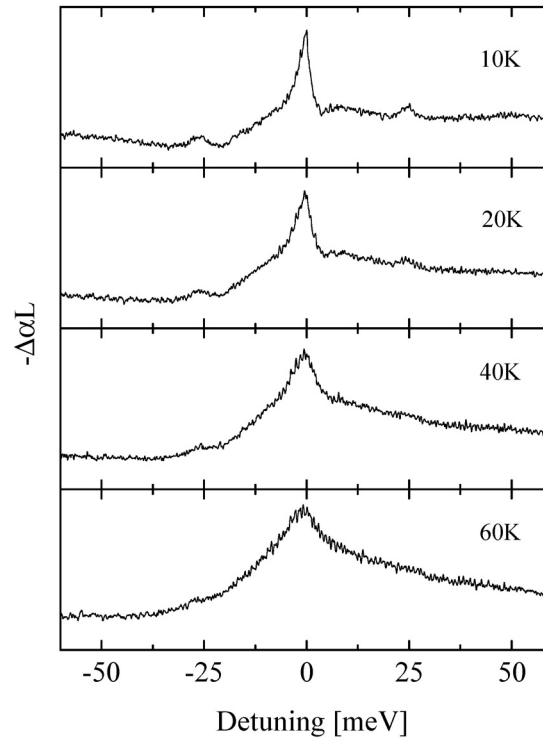


*FIGURE 30. Temperature dependence of the SHB-response from sample NC1 ( $\Omega = 2\text{kHz}$ ).*

#### Zero-phonon-line (ZPL) and confined acoustic-phonon sidebands

The smooth lineshape of the ZOPL for samples NC1 and NC4 indicates coupling to a continuum of acoustic phonons. Discrete acoustic phonon sidebands are yet expected, as a result of resonant reflections of acoustic phonons at the dot boundaries in ‘free-standing’ nanocrystals. Figure 31 shows an expansion of the ZOPL for samples NC1 and NC4. Minimum step size of the coarse tuning was used to obtain maximum resolution. The difference in signal-to-noise (SNR) between

the two spectra indicates much quieter operation of the diode laser, which was used to measure the spectrum from sample NC1. Both spectra reveal a fine structure of the ZOPL, which consists of the aforementioned sharp resonance at zero detuning as well as discrete sidebands at positive and negative detuning. We assign the observed features to ZPL and discrete acoustic phonon sidebands respectively. ZPL and acoustic phonon sidebands exhibit similar linewidths on the order of  $100 \mu\text{eV}$ . This value compares well with the resolution limited ZPL linewidths obtained from single-dot PL-studies<sup>9</sup>.

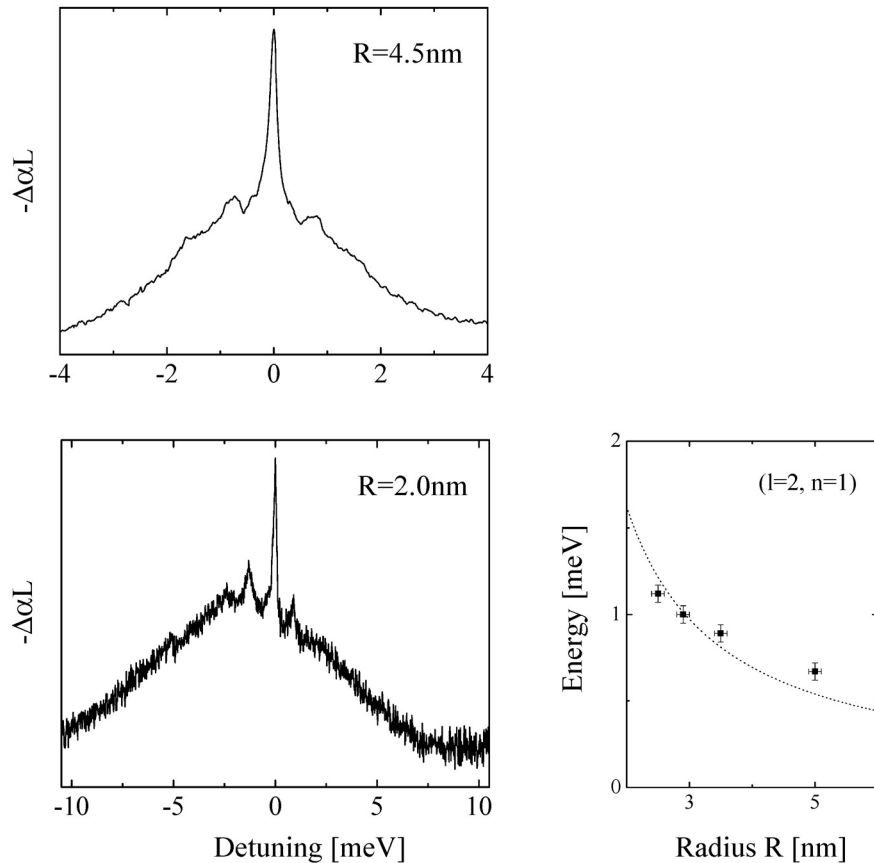


**FIGURE 31.** Fine structure of the ZOPL for sample NC1 and NC4 ( $\Omega = 2\text{kHz}$ ). ZPL and confined acoustic phonon assisted transitions are revealed. The plot on the right depicts the sideband splitting as obtained from the SHB-spectra as a function of the dot radius. The dotted line is the theoretically expected size dependence of the ( $l=2, n=1$ ) acoustic phonon mode energy assuming ‘free’ boundary conditions.

To further investigate confinement of acoustic phonons, we carried out a size dependent study of the acoustic phonon sideband splitting. The results are shown in Figure 31. Plotted on the right is the experimentally observed sideband splitting as a function of the dot radius  $R$ . The dotted line depicts the theoretically expected size dependence of the ( $l = 2, n = 1$ ) confined acoustic phonon mode assuming a spherical dot shape and ‘free’ boundary conditions<sup>65</sup>. The good agreement between theory and experiment allows us to unambiguously assign the observed sidebands to optical transitions assisted by the confined ( $l = 2, n = 1$ ) acoustic phonon mode. The increasing discrepancy between theory and experiment for larger dots is attributed to deviations from a spherical dot shape. Note that TEM images reveal an increasingly prolate dot shape for increasing dot sizes.

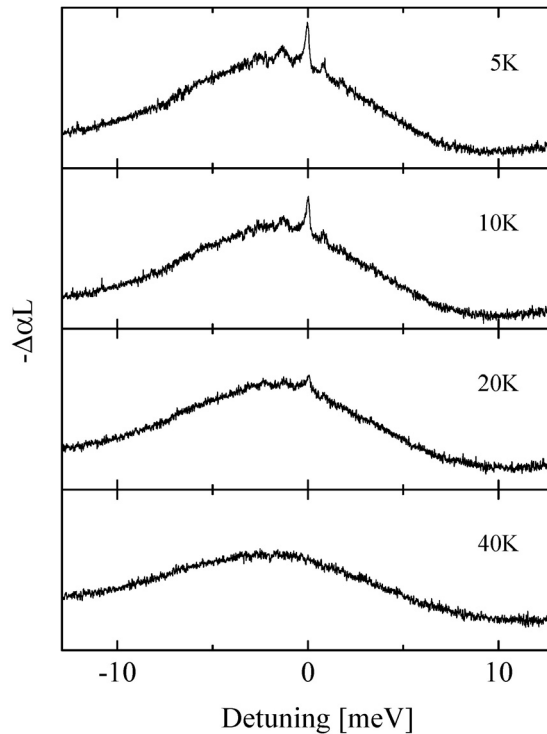


*FIGURE 32. Temperature dependence of the ZOPL from sample NC4 ( $\Omega = 2\text{kHz}$ ). The ZPL and acoustic phonon sidebands disappear around  $T = 20\text{K}$ .*

Figure 32 shows a temperature dependence of the ZOPL for sample NC4. The spectral weight of the ZPL decreases with increasing temperature and eventually disappears for  $T > 20\text{K}$ . The acoustic phonon pedestal exhibits broadening with increasing temperature and dominates the SHB spectrum. Similar observations were made for sample NC1.

### Dipole dephasing and spectral diffusion of the ZPL

In order to probe the effects of spectral diffusion, we carried out a modulation frequency dependent study of the ZPL linewidth. Figure 33 shows the ZOPL from sample NC1 at  $T = 2\text{K}$  obtained for  $\Omega = 1, 10$  and  $100\text{kHz}$ , corresponding to integration times of  $\tau = 1/\Omega = 1\text{ms}$ ,  $100\mu\text{s}$  and  $10\mu\text{s}$  in the SHB-measurement.

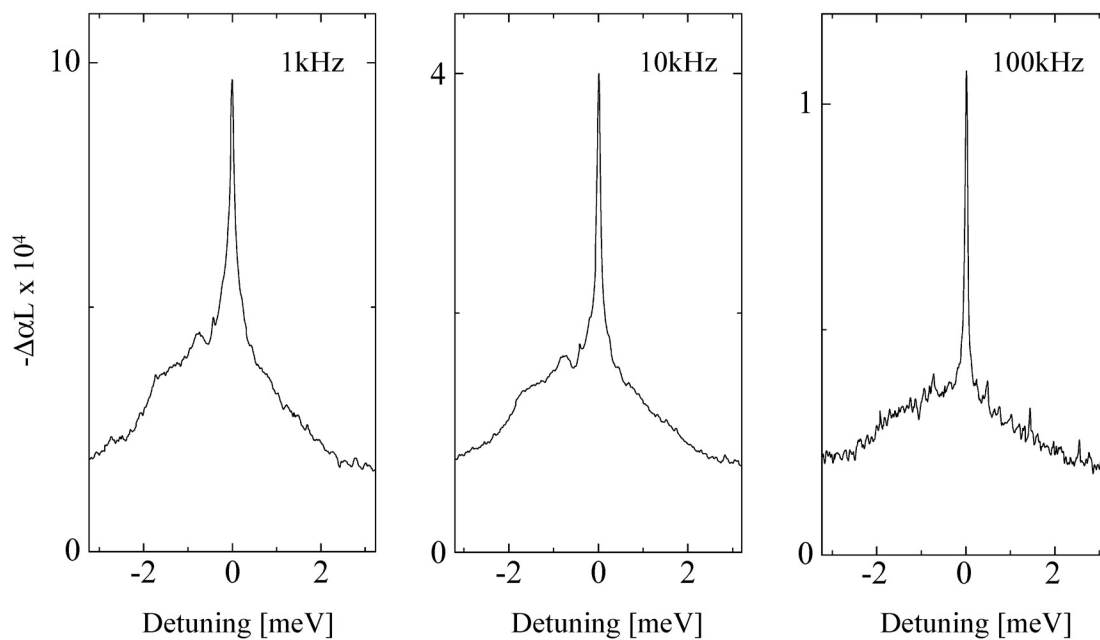


*FIGURE 33.* ZOPL from sample NC1 ( $T = 2\text{K}$ ) at various modulation frequencies  $\Omega$ . The ZPL exhibits a narrowing as  $\Omega$  is increased, revealing the presence of spectral diffusion in the SHB-measurement.

Three observations are made. First, the acoustic phonon sideband at positive detuning is significantly weaker than its counterpart at negative detuning indicating freeze-out of the ( $l = 2$ ,  $n = 1$ ) acoustic phonon at  $T = 2$  K. Second, the magnitude of the nonlinear signal shows a decrease by one order of magnitude as  $\Omega$  is increased from 1 to 100 kHz, indicating a slow decay of the SHB-response. Most importantly, the ZPL shows a spectral narrowing with increasing modulation frequency demonstrating the presence of spectral diffusion. Note that the observed increase in the ZPL/pedestal peak ratios for increasing  $\Omega$  results from the narrowing of the ZPL rather than a change in the spectral weight ratio of the ZPL and the acoustic phonon pedestal.

The modulation frequency dependence of the ZPL-linewidth at  $T = 2$  K is plotted in Figure 34. Also shown is a high-resolution scan of the ZPL at high modulation frequency and low excitation levels at that temperature. The ZPL linewidth exhibits a rapid decrease as the modulation frequency is increased from 1 to 100 kHz, indicating that at the excitation level used ( $I_{\text{pump}} = I_{\text{probe}} = 0.5$  W/cm<sup>2</sup>), effects of spectral diffusion are most pronounced at times scales exceeding 10  $\mu$ s. The ZPL-linewidth approaches an asymptotic value at modulation frequencies exceeding 1 MHz.

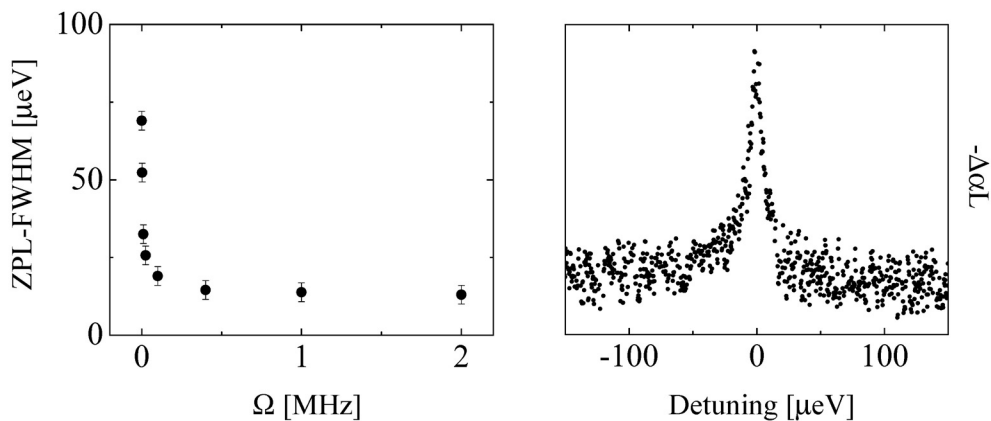


**FIGURE 34.** Left: Modulation frequency dependence of the ZPL-linewidth at  $T = 2$  K and  $I_{\text{pump}} = I_{\text{probe}} = 0.5$  W/cm<sup>2</sup> (sample NCl). Right: high-resolution scan of the ZPL for  $\Omega = 1$  MHz ( $I_{\text{pump}} = 2I_{\text{probe}} = 1.0$  W/cm<sup>2</sup> and  $T = 2$  K).

Figure 35 (left) shows the pump intensity dependence of the ZPL-linewidth for two different integration times used in the SHB-measurement. The ZPL linewidth shows an increase with increasing pump power. Note that the excitation levels used in the measurement are far below the saturation intensity  $I_s$  of the absorbing transition, for which we obtain a rough estimate of  $I_s = \hbar\omega/(\sigma T_1) = 10^5 \text{ W/cm}^2$  ( $\hbar\omega$ : photon energy, absorption cross section  $\sigma \sim 10^{-15} \text{ cm}^2$ ; radiative lifetime  $T_1 \sim 10 \text{ ns}$ <sup>86</sup>). Note also that although a nonlinear optical measurement, excitation levels in SHB are at least two orders of magnitude smaller than typical excitation levels used in single-nanocrystal PL-studies<sup>75</sup>. We conclude that, instead of conventional power broadening beyond the  $\chi^{(3)}$ -limit, the power dependence of the ZPL-linewidth observed here is due to light-induced spectral diffusion<sup>9</sup>. For both integration times used, the ZPL-linewidth remains constant in the region for which  $I_{\text{pump}} < I_{\text{probe}}$ , where light-induced spectral diffusion is limited by the probe beam. In the region where spectral diffusion is predominantly caused by the pump ( $I_{\text{pump}} > I_{\text{probe}}$ ), the ZPL broadening follows a power law behaviour.

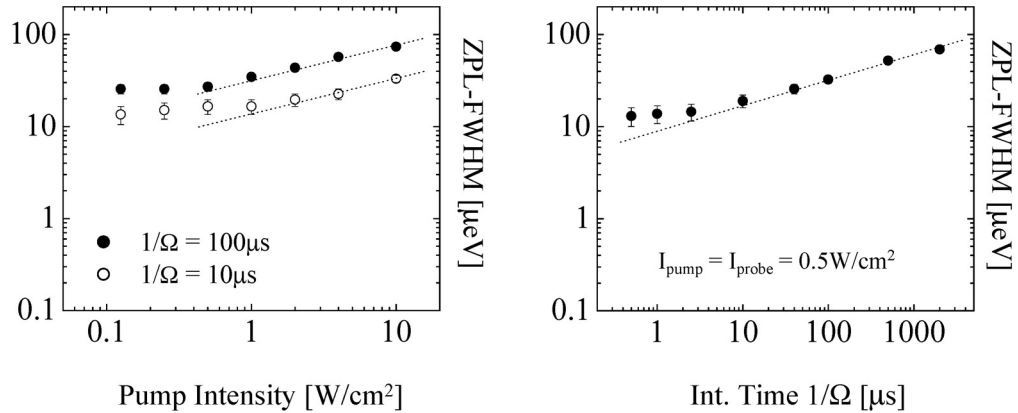


**FIGURE 35.** Left: Pump intensity dependence of the ZPL-linewidth at  $T = 2\text{K}$  ( $I_{\text{probe}} = 0.5 \text{ W/cm}^2$ ) for two different integration times. Power broadening is due to light-induced spectral diffusion. Right: same data as shown in Figure 34, however plotted as a function of the integration time  $1/\Omega$ .

The modulation frequency dependence of the ZPL linewidth as shown in Figure 34 is redrawn in Figure 35 (right) as a function of the integration time  $\tau = 1/\Omega$ . As for the intensity dependence, the log-log scale reveals a power law behaviour for  $1/\Omega > 10 \mu\text{s}$ . For integration times  $< 10 \mu\text{s}$  no significant decrease of the ZPL linewidth is observed if the integration time is further decreased. We infer that broadening of the ZPL due to spectral diffusion is suppressed in this region. Thus, the measured linewidth approaches the intrinsic linewidth of the optical transition at integration times  $< 10 \mu\text{s}$  at the given excitation level.

Combining the results of the modulation frequency- and pump intensity- dependence of the ZPL- linewidth, we conclude that we are able to suppress the effects of spectral diffusion at low enough number of QD-photo-excitations during the acquisition time used in the measurement. The number of photo-excitations during a measurement cycle is proportional to the integration time and the excitation level. Resulting from a light-induced process, line broadening caused by spectral diffusion depends on the product of the excitation level and the integration time, i.e. the average number of excitations of a nanocrystal during the acquisition time of the experiment<sup>95</sup>. Effects of spectral diffusion are thus suppressed in a regime, in which the number of photo-excitations within the acquisition time of the measurement is on the order of/lower than one. In this case, series of carrier trapping events accompanied by spectral shifts of the optical transition energy during the acquisition time are eliminated from the experiment. Clearly, this regime can not be realized in single-QD measurements. In contrast, note that in the SHB-measurements carried out here, average numbers of photons incident on a nanocrystal during the integration time range on the order of 0.01-100. Taking e.g.  $I_{\text{pump}} = 1 \text{ W/cm}^2$  and  $\tau = 10 \mu\text{s}$ , which marks the onset of suppression of spectral diffusion as shown in Fig. 35, the average number of photons incident on of a single nanocrystal (absorption cross section  $\sigma = 10^{-15} \text{ cm}^2$ ) is on the order of 0.1.

In the asymptotic limit in which light-induced spectral diffusion is suppressed in the experiment, we measure a FWHM of  $(12 \pm 2) \mu\text{eV}$ . This linewidth reflects the *intrinsic* homogeneous broadening of the ZPL.

The data discussed in this section were obtained for nanocrystals of batch NC1. The same qualitative and quantitative behaviours were observed for samples NC2-4. In the size range investigated, we thus measure dephasing rates of  $\gamma = (3.0 \pm 0.5) \mu\text{eV}$  corresponding to dephasing times of the zero-phonon-transitions as long as 200 ps. In contrast to previous single-dot PL studies, we are able to measure the intrinsic homogeneous linewidth in an asymptotic limit, in which effects of light-induced spectral diffusion are negligible.

#### Lifetime of the SHB-response

Along with the narrowing of the ZPL discussed in the previous section, a decrease of the SHB-signal was observed for increasing modulation frequency. The resulting deterioration in SNR prevented us in fact from carrying out measurements with modulation frequencies significantly higher than 1 MHz. The observation indicates that the nonlinear mechanism underlying the SHB response features a surprisingly long lifetime. To determine the lifetime and gain insight into the physical mechanism giving rise to the SHB-response, we carried out additional studies employing nearly degenerate FWM<sup>91</sup>. Figure 36 shows the FWM response obtained at  $T = 10 \text{ K}$  for sample NC1. The observed resonance reveals the coherent contribution of the nonlinear optical response. Note that a similar feature can be observed directly in SHB and has been confirmed for all samples investigated. The coherent feature observed in the FWM-response exhibits a non-Lorentzian lineshape, which is also evident from the highly non-exponential decay of the Fourier transform of the FWM-response in Figure 37. Note, that the relaxation time of the nonlinear response exceeds the radiative lifetime of the bright exciton by over two orders of magnitude.

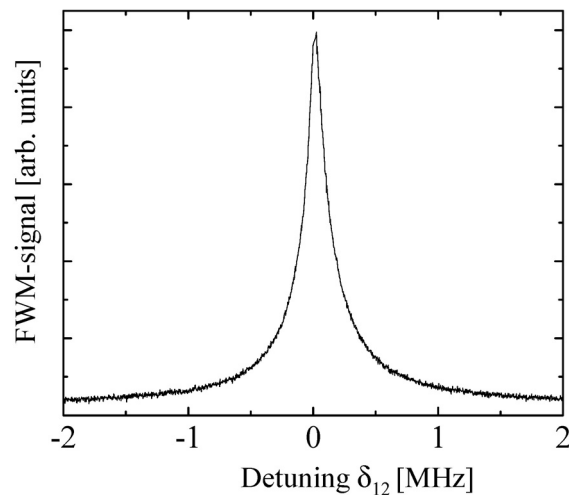


*FIGURE 36. Coherent contribution to the three-beam FWM-response from sample NC1 ( $T = 10\text{K}$ ). The linewidth of the coherent FWM-response reveals a distribution of SHB-lifetimes exceeding the radiative lifetime of the bright exciton ( $\sim 10\text{ ns}$ ) by over two orders of magnitude.*

To elucidate our observations, we consider an energy level diagram as shown schematically in Figure 37, in which  $|g\rangle$  and  $|x\rangle$  denote the ground state and the bright exciton respectively. In addition, a distribution of dark states  $|d\rangle$  is included, to account for dark states, intrinsic or extrinsic. Being the only dipole allowed transition present, resonant optical interaction occurs via the bright exciton. Although not coupled to optical fields, the dark states  $|d\rangle$  can significantly modify the relaxation dynamics of optical excitations induced via the bright exciton. Saturation of the bright exciton is determined by the population difference between states  $|x\rangle$  and  $|g\rangle$ . Optical nonlinearities caused by saturation can thus arise from population of the excited state  $|x\rangle$  and/or depletion of the ground state  $|g\rangle$ . Depletion occurs if the excitation is prevented from returning to the ground state  $|g\rangle$ . This is the case if relaxation into long-lived dark states  $|d\rangle$  occurs at a rate faster than radiative recombination into the ground state. Then, the lifetime associated with the nonlinear response is determined by the time it takes for nanocrystals in  $|d\rangle$  to recover. In

contrast, the lifetime associated with the nonlinear response due to population in  $|x\rangle$  is determined by the lifetime of the bright exciton. The Fourier-transform of the FWM-response shown in Figure 37, features time scales on the order of microseconds and is thus primarily due to nanocrystals in  $|d\rangle$ . No contribution to the FWM response was observed from radiative decay.

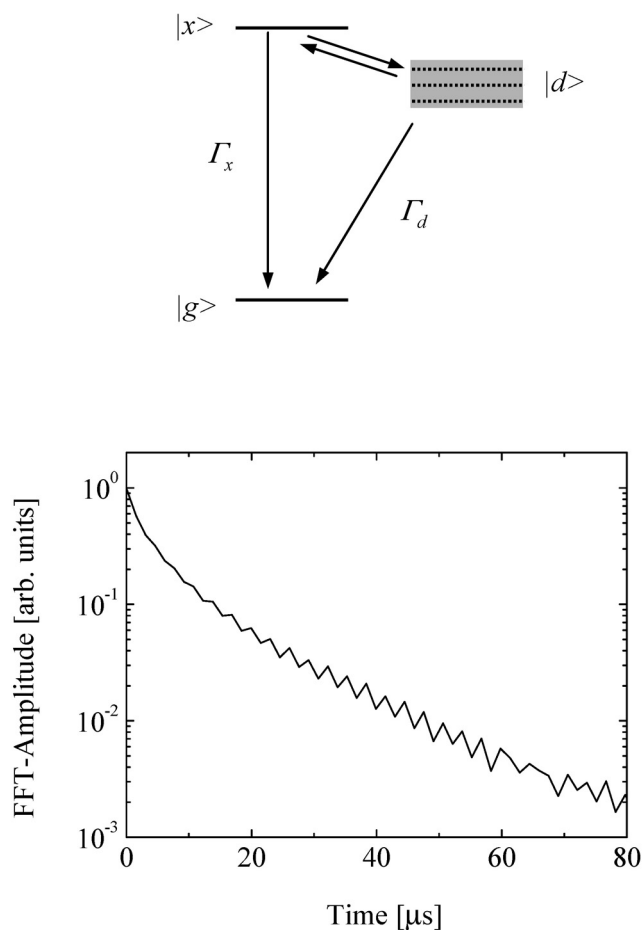


*FIGURE 37. Top: energy level diagram to model the bright exciton and possible effects of dark states. Bottom: Fourier-transform of the FWM-response shown in Figure 36.*

Note that continuous-wave nonlinear optical measurements are particularly sensitive to long-lived excitations as e.g. the third order nonlinear response scales with the lifetime of the relevant excitation giving rise to the optical nonlinearity. In this regard, the fact that we only observe

effects from the dark states in the coherent contribution observed in the FWM-response does not rule out relaxation via radiative recombination. In fact, TR-PL shows a significant contribution from radiative combination in core/shell nanocrystals in addition to a long tail in the microsecond range, which is due to dark states (intrinsic or extrinsic)<sup>86</sup>.

Applying the OBE to the energy level diagram shown in Figure 37, we have calculated the third order nonlinear optical polarization for the FWM response for an inhomogeneously broadened system<sup>20</sup>:

$$P^{(3)} \propto \mu^4 \frac{E_1 E_2^* E_{pr} \exp(-i\omega_s t)}{(\delta + i\Gamma) (\delta + i\Gamma_x) (\omega_s - \omega_2 + 2i\gamma)} + c.c \quad (6.1)$$

where  $\mu$  and  $\gamma$  are the dipole moment and intrinsic decoherence rate for the bright exciton respectively (effects of spectral diffusion are not included);  $\Gamma_x$  and  $\Gamma_d$  is the population decay rate for  $|x\rangle$  and the recovery rate for nanocrystals in  $|d\rangle$  respectively. In the limit that  $\Gamma_d \ll \Gamma_x$  the FWM response as a function of the detuning  $\delta$  is characterized by a Lorentzian with linewidth  $2\Gamma_d$ . Note we have only included a single state for  $|d\rangle$  in the calculation. For a distribution of  $|d\rangle$  along with a distribution of recovery rates  $\Gamma_d$  a non-Lorentzian lineshape is expected, consistent with the experimental results shown in Figure 36. The FWM-response reveals thus recovery times of the surface traps and the lifetime of the intrinsic dark exciton. The observed recovery times show good agreement with the integration times at which spectral diffusion is suppressed. This correlation confirms the previously established connection between spectral diffusion and charge trapping and demonstrates that once effects of carrier trapping are eliminated from the SHB measurement, so is spectral diffusion.

### Summary

Spectral diffusion and carrier trapping known to occur in CdSe-nanocrystals manifest in SHB in terms of a modulation frequency dependent ZPL-linewidth and a persistent SHB-response, lifetimes of which far exceed the radiative lifetime of the bright exciton. The correlation between spectral diffusion and carrier trapping is confirmed in a comparison between the SHB-lifetime, which is representative of trap recovery times, and the integration times at which spectral diffusion is suppressed. The SHB-study reveals that effects of light-induced spectral diffusion are negligible for experimental conditions, in which the average number of photo-excitations/dot within the acquisition time of the measurement is less than one. In contrast to single-dot measurements, SHB can meet this condition and therefore allows for measurements of the *intrinsic* homogenous linewidth. Within the size range investigated ( $R = 2$  to  $4.5$  nm), dipole dephasing times are independent of the dot size and on the order of 200 ps. In addition to the ZPL, acoustic- and LO- phonon-assisted transitions are directly observed in the frequency-domain SHB-spectra. In particular, discrete acoustic phonon modes are revealed. Discussion of the possible mechanisms giving rise to decoherence of the ZPL will be given by the end of the next chapter in a joint summary of our studies on dipole dephasing in CdSe nanocrystals and self-assembled CdSe-QDs.

## CHAPTER VII

## DIPOLE DEPHASING IN SELF-ASSEMBLED CdSe/ZnSe QUANTUM DOTS

The results of our SHB-study of self-assembled CdSe/ZnSe QDs are presented. Unless otherwise mentioned, experiments were carried out at  $T = 10$  K. Cross-linear polarized pump/probe configuration was used to allow for rejection of pump scatter and thus improved SNR. With  $I_{\text{pump}} \sim \text{few W/cm}^2$ , measurements were carried out in the  $\chi^{(3)}$ -regime ( $\Delta T/T \sim 10^{-5}$ ). The SHB-response reveals features similar to those obtained from CdSe/ZnS nanocrystals. Emphasis is thus on differences between these two types of QD-systems as observed in SHB.

Zero-optical-phonon line (ZOPL) and LO-phonon sidebands

Figure 38 shows the low-temperature PL-spectrum for excitation in the wetting layer along with the nonlinear absorption profile of the band-edge exciton. Note that in contrast to nanocrystals, for which the band-edge energy is mainly determined by the dot radius, alloying of Cd and Zn can contribute to the blue shift of the band-edge luminescence in epitaxially grown CdSe/ZnSe QDs. The periodic structure at the high-energy side of the inhomogeneously broadened PL-spectrum reveals a series of ‘humps’ with equidistant spacing of  $(26 \pm 1 \text{ meV})$ , which is in fair agreement with the energy  $E_{\text{LO}}$  of the bulk LO-phonon. The observed progression is due to LO-phonons and is characteristic for excitation in the wetting layer. It is indicative of efficient capture of the photo-excited electron-hole pairs into the CdSe-dots via emission of LO-phonons. Since the LO-phonon progression masks the linewidth of the PL, we deduce the inhomogeneous broadening of the CdSe-QDs from a Gaussian fit to the nonlinear absorption profile. The nonlinear absorption does not reveal a significant ‘Stokes’-shift with respect to the PL-spectrum.

The shaded region marks the interval of pump energy positions used in the SHB-measurements. No significant dependence on the pump energy was observed even outside this shaded region. Nevertheless, carrying out the SHB-measurements in the low-energy part of the nonlinear absorption spectrum ensures that contributions from higher excited states to the SHB-response are minimized.

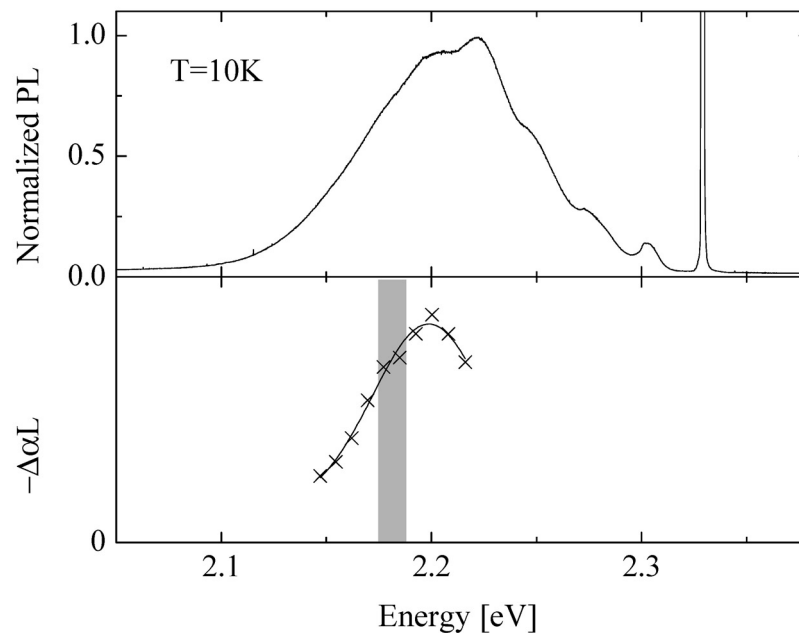


**FIGURE 38.** Top/bottom: PL/nonlinear absorption spectrum. The PL-spectrum shows a LO-phonon progression characteristic for excitation in the wetting layer (excitation at  $E = 2.33\text{eV}$ , scatter of excitation source is visible in the spectrum). The shaded region shown with the nonlinear absorption profile marks the interval of pump energy positions used in the SHB-measurements.

Figure 39 shows the SHB-response as a function of the pump-probe detuning. Note that due to the weak sample absorption, normalization was carried out with respect to the laser spectrum incident on the sample. The overall slope of the SHB-response is thus most likely reminiscent of this artificial normalization and not of importance here. As for chemically grown CdSe-nanocrystals, we observe three features: LO-phonon sidebands, acoustic-phonon pedestal and

ZPL. The LO-phonon sidebands exhibit the same broadening as the acoustic phonon pedestal indicative of a multi-phonon process involving acoustic- and LO- phonons as explained in Chapter VI. An expansion of the ZOPL is shown in the inset of Figure 39. As opposed to ‘free-standing’ nanocrystals, discrete acoustic phonon sidebands are absent in SHB from self-assembled CdSe/ZnSe QDs. Due to matching elastic properties of CdSe and ZnSe, resonant reflections of acoustic phonons do not occur at the CdSe/ZnSe interface and the electronic states couple to the 3D continuum of acoustic phonons of the overall structure. The asymmetric lineshape of the ZOPL is indicative of acoustic phonon freeze-out at low temperature.

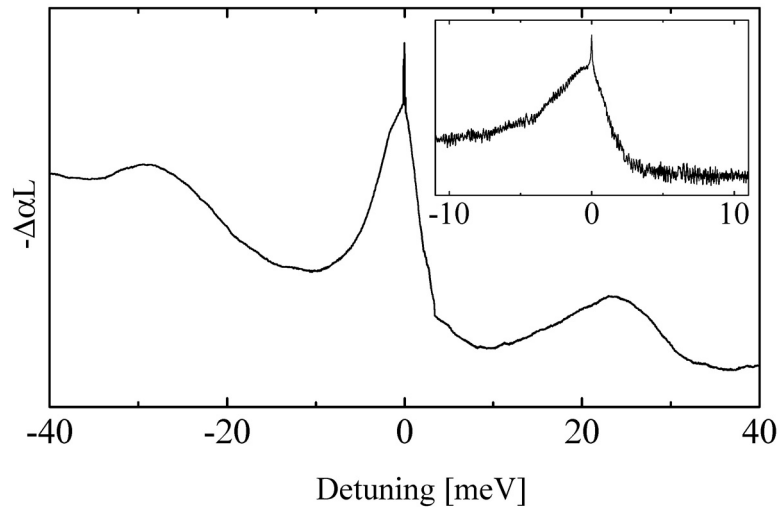


*FIGURE 39.* SHB-response at  $T = 10$  K ( $\Omega = 2$  kHz). The spectrum reveals LO-phonon- and acoustic phonon- assisted transitions and the ZPL. The inset shows an expansion of the ZOPL. Acoustic phonon assisted transitions give rise to a broad pedestal. Effects of acoustic phonon confinement are not observed.

Figure 40 shows a temperature dependence of the ZOPL. Similar to CdSe nanocrystals, the ZPL persists up to  $\sim 25$  K. The acoustic phonon pedestal exhibits spectral broadening with increasing temperature. The series of spectra demonstrates that coupling to acoustic phonons dominates dipole dephasing in self-assembled CdSe/ZnSe QDs at low temperatures.

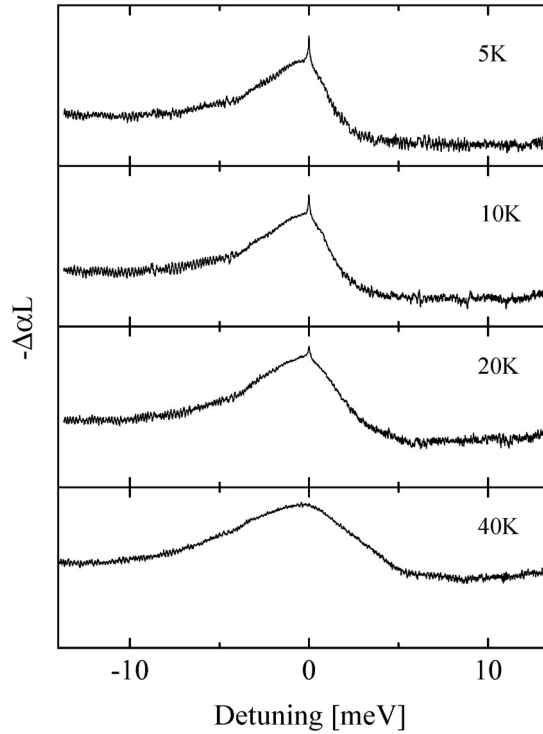


*FIGURE 40. Temperature dependence of the ZOPL ( $\Omega = 2\text{kHz}$ ).*

#### Dipole dephasing and spectral diffusion of the ZPL

In Figure 41, we show a series of SHB-spectra of the ZOPL obtained at different modulation frequencies,  $\Omega = 0.03, 0.3$  and  $3.0$  MHz. Similar to the results obtained for CdSe-nanocrystals, we observe a decrease of the SHB- signal with increasing modulation frequency, indicative of a long lifetime of the SHB-response. Furthermore, we observe a narrowing of the ZPL as the modulation frequency is increased. Note, that the accompanying changes in ZPL/acoustic-phonon pedestal peak ratios are mainly caused by narrowing of the ZPL. We infer that spectral diffusion is also present in CdSe/ZnSe self-assembled QD-systems. Detailed microscopic origins for spectral diffusion in self-assembled QDs are still poorly understood with carrier trapping or fluctuations in the strain field being possible mechanisms.

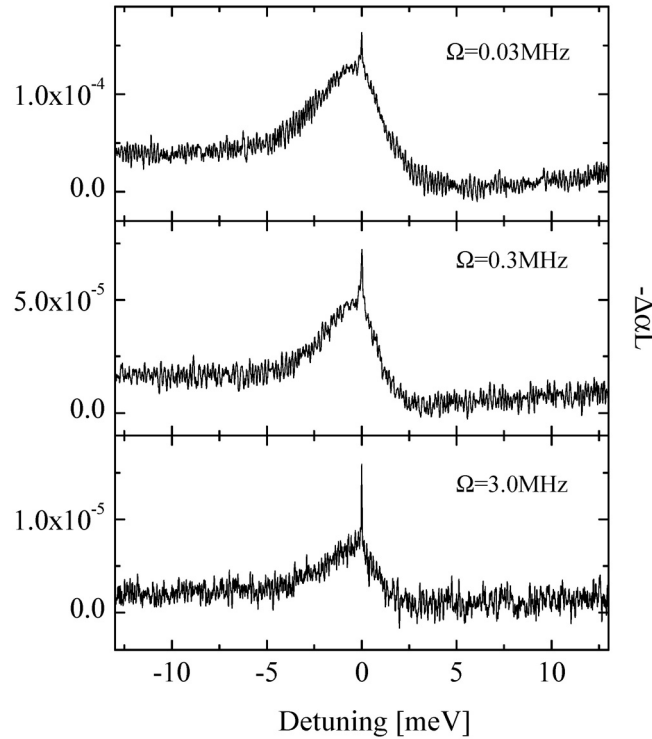


*FIGURE 41. Modulation frequency dependence of the ZOPL spectrum ( $T = 10K$ ).*

Figure 42 shows high-resolution spectra of the ZPL at modulation frequencies  $\Omega = 0.03, 0.3$  and  $3.0$  MHz. Effects of spectral diffusion manifest in an asymmetric lineshape. The ZPL exhibits a longer tail at negative detuning. The lineshape asymmetry diminishes with increasing modulation frequency and is almost absent in the spectrum obtained for  $\Omega = 3\text{MHz}$ , indicating that effects of spectral diffusion are mostly suppressed at that modulation frequency and the given excitation level. The linewidth of the ZPL exhibits a decrease with increasing modulation frequency. At the given excitation level, effects of spectral diffusion are most prominent for modulation frequencies  $\Omega < 2\text{MHz}$ . Combining the power dependence shown in the inset with the modulation frequency dependence of the ZPL linewidth, shows that effects of spectral diffusion are suppressed for  $I_{\text{pump}} < 5\text{W/cm}^2$  and  $\Omega > 3\text{MHz}$ .

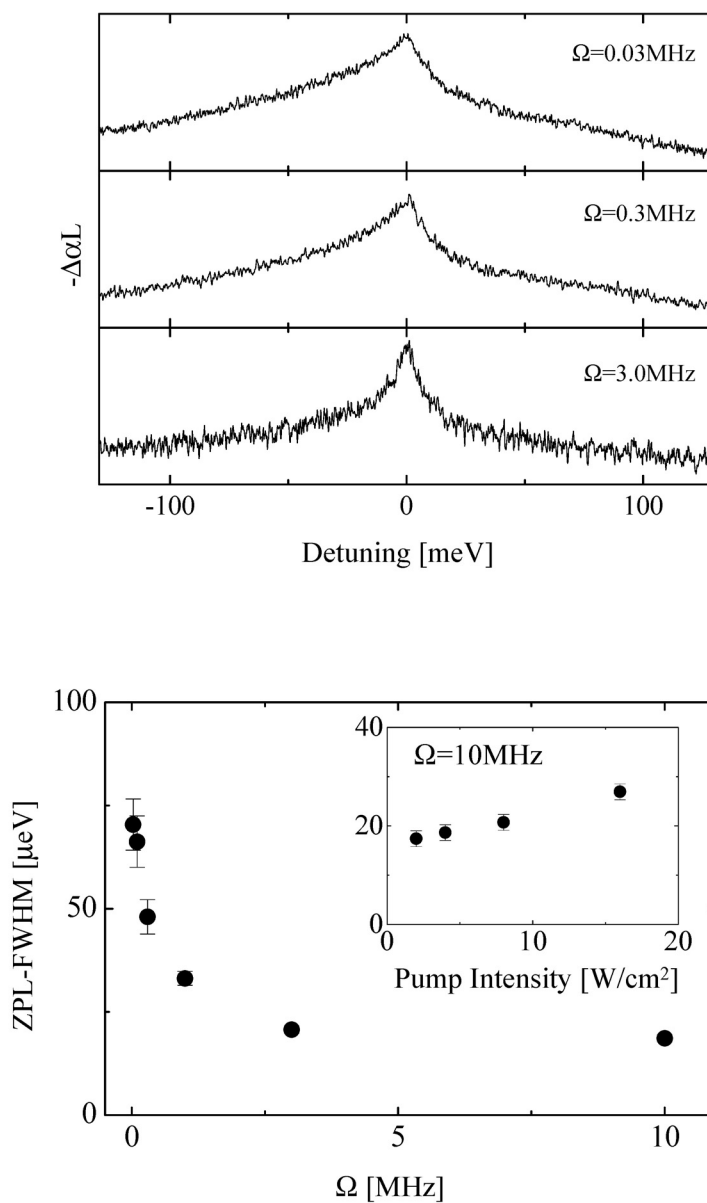


*FIGURE 42. Modulation frequency dependence of the ZPL ( $T = 10\text{K}$ ).*

Despite the similar behaviours observed for self-assembled QDs and nanocrystals, a discussion of spectral diffusion and its possible origins is omitted here, due to the lack of studies on the photo-physical behaviour of self-assembled QDs.

In Figure 43 we present the results of a temperature dependent study of the ZPL in a regime where spectral diffusion is suppressed. The figure on the left, shows a sequence of high-resolution SHB-spectra at various temperatures. The temperature dependence of the dephasing rate  $\gamma$  is obtained from the linewidth of the ZPL and shown on the right. Extrapolation of the experimental data yields a dephasing rate of  $3.5 \mu\text{eV}$  at zero temperature.

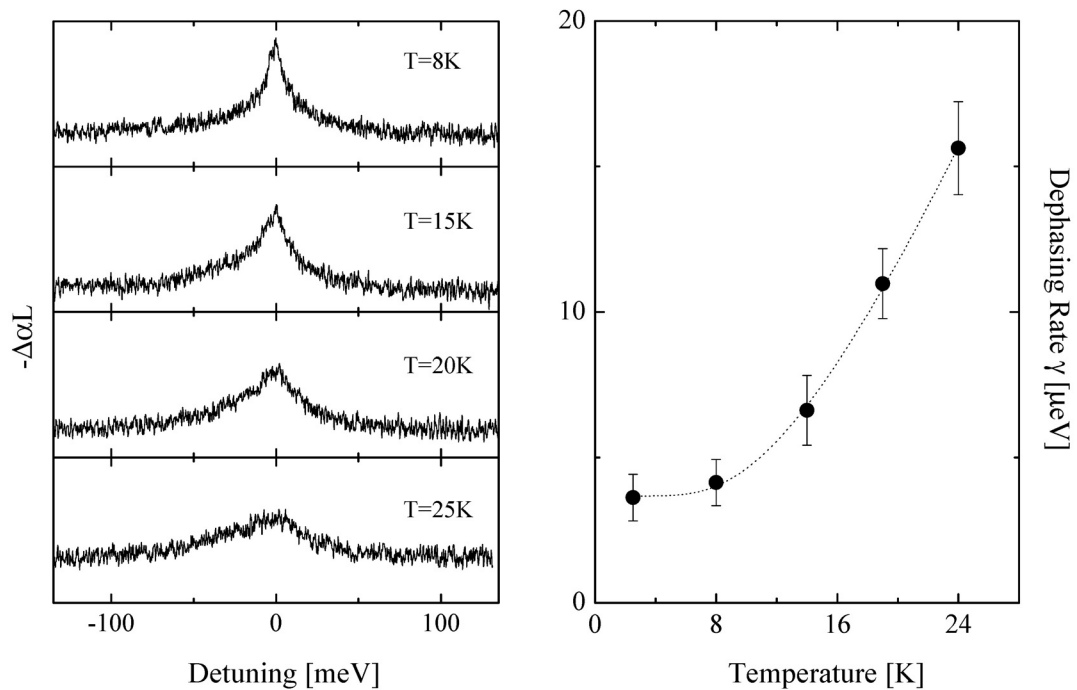


**FIGURE 43.** Temperature dependence of the ZPL. Effects of spectral diffusion are mostly suppressed at the low excitation level and the short integration time used in the measurement ( $I_{\text{pump}} = 10I_{\text{probe}} = 4 \text{ W/cm}^2$ ,  $\Omega = 3 \text{ MHz}$ ).

Within the framework of the independent boson model and a linear coupling mechanism, electron-phonon interactions in a QD can lead to phonon-assisted transitions that involve absorption or emission of phonons, yet without resulting in a spectral broadening of the ZPL. To explain the observed broadening of the ZPL as well as its temperature dependence, we involve

the fine structure of the band-edge exciton in CdSe/ZnSe QDs. As discussed in Chapter II, exchange interaction leads to a splitting between bright and dark states in the heavy-hole exciton manifold, with the dark states lying energetically below the bright state in CdSe-QDs. Spin relaxation of the bright exciton to the dark exciton via emission of acoustic phonons could lead to decoherence of the ZPL, as suggested in an earlier theoretical study<sup>96</sup>. Note that this process can provide a decoherence mechanism for the zero-phonon-transition even at zero temperature. A numerical fit based on acoustic phonon emission alone, however, cannot account for the observed temperature dependence. Note that thermal activation into higher lying states via absorption of acoustic phonons presents a likely additional decoherence channel. Given the limited temperature range over which the ZPL persists ( $< 30$  K), we have not been able to extract relevant physical parameters including bright-dark splitting and the thermal activation energy from the temperature dependence. Nevertheless, the strong temperature dependence of the ZPL linewidth indicates significant contribution of electron-phonon interactions to decoherence of the ZPL.

In a collaboration with Serguei V. Goupalov, we have been able to gain a more detailed understanding of the relative contribution from acoustic phonon-assisted transitions and the ZPL to the ZOPL. A two-level system is used to model the bright exciton, which couples to a continuum of acoustic phonons via deformation potential coupling. Apart from excluding piezoelectric coupling and coupling to LO-phonons here, the basic assumptions of the model are thus essentially the same as those of a previous theoretical study<sup>70</sup>, the results of which were outlined in a discussion of electron-phonon interactions in Chapter IV. While ZPL broadening is not accounted for, the model is able to predict the relative spectral weight of the ZPL and the acoustic phonon pedestal. The calculation follows the steps outlined in reference 96. The linear absorption cross-section is obtained from Kubo's formula,

$$\sigma(\omega) \propto \int_0^{\infty} dt \left[ \text{Re}[U(t)] \cos(\omega - \omega_0)t - \text{Im}[U(t)] \sin(\omega - \omega_0)t \right] \quad (7.1)$$

where  $\omega_0$  is the transition frequency of the two-level system in the absence of electron-phonon interactions;  $U(t)$  is given by  $U(t) = e^{K(t)}$ , where  $K(t)$  has the form:

$$K(t) = -\gamma_{\text{ZPL}}t + \frac{1}{V} \sum_{\mathbf{q}} \frac{|A_{\mathbf{q}}|^2}{\omega_{\mathbf{q}}^2} \left[ (\cos \omega_{\mathbf{q}}t - 1) \coth \frac{\hbar \omega_{\mathbf{q}}}{2T} - i (\sin \omega_{\mathbf{q}}t - \omega_{\mathbf{q}}t) \right] \quad (7.2)$$

ZPL broadening is added phenomenologically and  $\gamma_{\text{ZPL}}$  is taken from the experiment. The sum runs over all longitudinal acoustic modes with wavevectors  $\mathbf{q}$ , and frequencies  $\omega_{\mathbf{q}}$ ;  $T$  denotes temperature,  $V$  is the normalization volume. Electron-phonon interactions enter via the Huang-Rhys factors  $|A_{\mathbf{q}}|^2/\omega_{\mathbf{q}}^2$  and depend sensitively on the bulk electron/hole deformation coupling constant and the form factor, which is determined by the dot size and shape. Deformation coupling constant of  $D_e = 11$  eV and  $D_h = 8.9$  eV were used in the numerical simulation<sup>97</sup>.

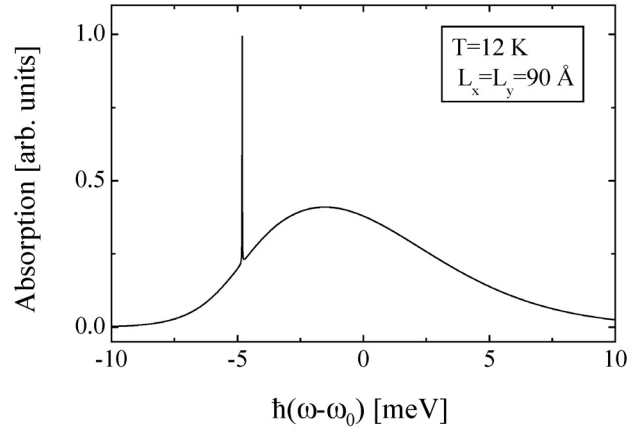


**FIGURE 44.** Calculated linear absorption spectrum for a single CdSe-QD. Although broadening of the ZPL is not included in the model, the relative contribution  $\eta$  from the ZPL and the acoustic phonon assisted transitions to the ZOPL is well reproduced.

Figure 44 shows the numerical results of the linear absorption spectrum of a single CdSe-QD embedded in ZnSe. For ease of calculation, a square shape confining potential is taken for in-plane motion ( $L_x = L_y = 9$  nm); confinement along the growth direction is determined by the square well potential of the wetting layer ( $L_z = 1.1$  nm). A polaron shift of  $\sim 5$  meV is revealed. The asymmetric lineshape of the acoustic phonon pedestal indicates that optical transitions assisted by emission rather than absorption of phonons dominate at low temperature. Comparison of the spectral weight ratio  $\eta$  defined as the ratio between the spectrally integrated area associated with the ZPL and the acoustic phonon pedestal respectively, shows good agreement with experiment. The theoretically and experimentally obtained values on the order of  $\eta \sim 0.01$  indicate that most of the oscillator strength of the electronic transition is distributed over the acoustic-phonon assisted transitions. The numerical calculation shows a rapid decrease of the relative ZPL contribution with increasing temperature, with the ZPL disappearing near  $T = 30$  K (not shown) in good agreement with the experiment. Additional calculations based on this model were carried out for InGaAs self-assembled QDs, for which ultralong dipole dephasing times have been previously observed<sup>3,4</sup>. In contrast to CdSe self-assembled QDs, spectral weight ratios of  $\eta \sim 1$  are calculated for InGaAs self-assembled QDs ( $T \sim 10$ K) in good agreement with experimental results. Coupling to acoustic phonons is thus significantly weaker in the III-V based InGaAs QDs.

### Summary

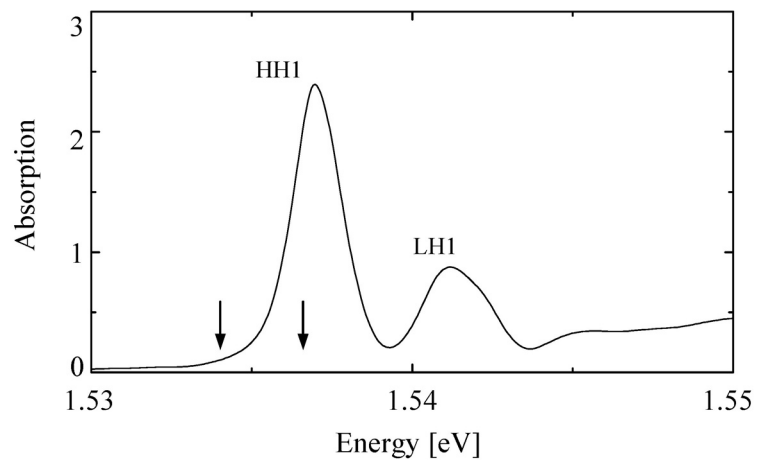
Using high-resolution frequency-domain SHB, we are able to reveal the characteristic features of electron-phonon interactions in the nonlinear optical absorption spectra from self-assembled CdSe/ZnSe QDs. The spectra show LO-phonon assisted transitions in form of LO-phonon sidebands, acoustic phonon assisted transitions in form of a broader pedestal at zero detuning, and

a sharp ZPL, associated with the purely electronic transition. The spectra reveal significantly enhanced coupling to acoustic-phonons in CdSe QDs over that in InGaAs QD systems. Our ability to suppress effects of spectral diffusion in the experiment, allows us to measure the intrinsic dephasing rate associated with the ZPL. Measured dephasing times are on the order of 200 ps. Thus, despite significantly increased coupling to acoustic phonons, dephasing of the ZPL is comparable to that in InGaAs QDs. A temperature dependent study of the ZPL linewidth clearly reveals that electron-phonon interactions contribute to dephasing of the ZPL. Spin relaxation of the bright exciton to the intrinsic dark exciton, as well as thermal activation to higher excited states are tentatively attributed to dephasing of the zero-phonon-transition in CdSe QDs. The good qualitative and quantitative agreement between self-assembled and chemically grown CdSe QDs as observed in SHB, shows that decoherence of the ZPL is insensitive to the detailed fine structure of the band-edge exciton and effects of acoustic phonon confinement. The possible ZPL-dephasing mechanisms discussed here, apply thus also to dephasing of the zero-phonon-transition in CdSe-nanocrystals.

## CHAPTER VIII

COHERENT RAMAN SCATTERING FROM ELECTRON SPIN COHERENCE  
IN GaAs-QUANTUM WELLS

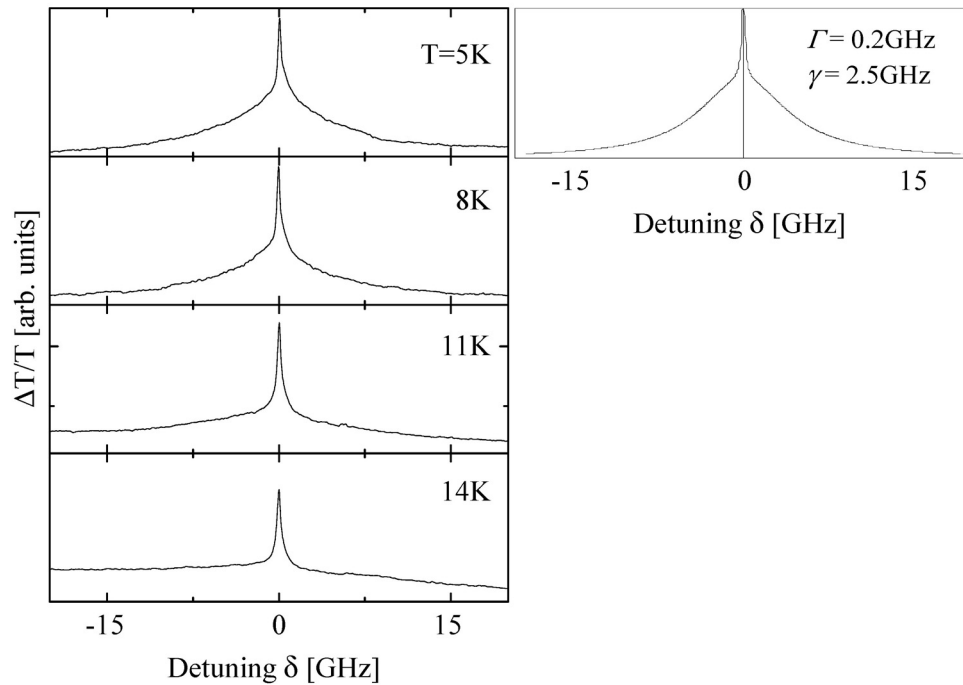
The results of our frequency-domain study on electron spin coherence are presented. Data are exclusively shown for sample QW1, which clearly exhibits effects of exciton localization. An independent study carried out on sample QW3 shows similar results, demonstrating general validity of our results independent of the particular growth technique. Figure 45 shows the absorption from QW1. The arrow below the HH1-exciton resonance marks the pump energy for coherent Raman measurements carried out on localized excitons. To measure the coherent Raman scattering response from mobile excitons the pump energy was set well into the resonance. Unless otherwise mentioned measurements were carried out in the  $\chi^{(3)}$ -regime ( $I_{\text{pump}} \sim \text{W/cm}^2$ ).



*FIGURE 45.* Linear absorption from sample QW1 at  $T = 10$  K. The arrow below/at the HH1-exciton absorption resonance indicates the pump energy position for measurements of the coherent Raman scattering from localized/mobile excitons respectively.

Coherent Raman scattering from localized excitons

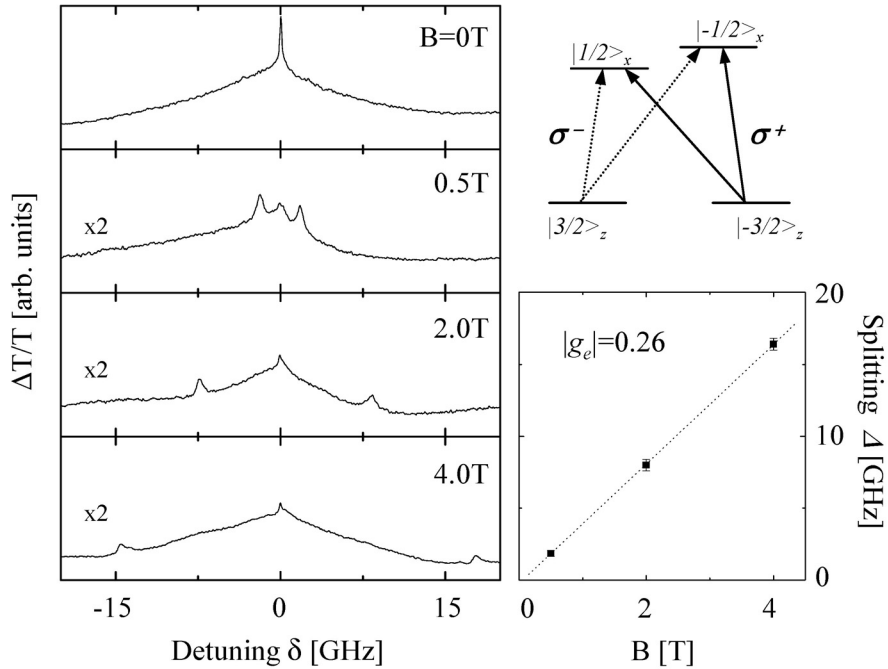
Figure 46 shows a series of SHB-spectra from localized excitons for co-circularly polarized pump and probe fields ( $\sigma^+$ ) and various temperatures. For  $T < 10$  K, the coherent and incoherent contribution of the SHB-response manifest in form of a sharp resonance and a broader pedestal respectively.



*FIGURE 46. Left: SHB-response from localized HHI-excitons at various temperatures. Right: SHB-response as obtained from third order solution of the OBE and using the parameters as obtained from the measurement.*

The coherent resonance features a linewidth of  $\sim 0.4$  GHz (FWHM). As spatial diffusion is negligible for localized excitons, the linewidth of the coherent resonance is a direct measure of the exciton lifetime ( $T_1 = 1/(\pi\Delta\nu) = 1/(2\pi\Gamma) = 0.8$  ns). Within the temperature range investigated, the linewidth of the coherent resonance remains constant.

The spectral hole exhibits a linewidth of  $\sim 10$  GHz at  $T = 5$  K corresponding to a dipole dephasing time of  $T_2 = 1/(2\pi\gamma) = 60$  ps. The graph to the right is a numerical fit as obtained from Eq.(5.2), with  $T_1$  and  $T_2$  taken from the experiment at  $T = 5$  K. The linewidth of the spectral hole exhibits a rapid increase with increasing temperature indicative of thermal activation of the localized excitons to delocalized states. For  $T > 15$ K the spectral hole is barely observed as the majority of excitons has become delocalized. Coherent Raman scattering experiments on localized excitons presented in the following were thus carried out at temperatures  $T < 10$  K.



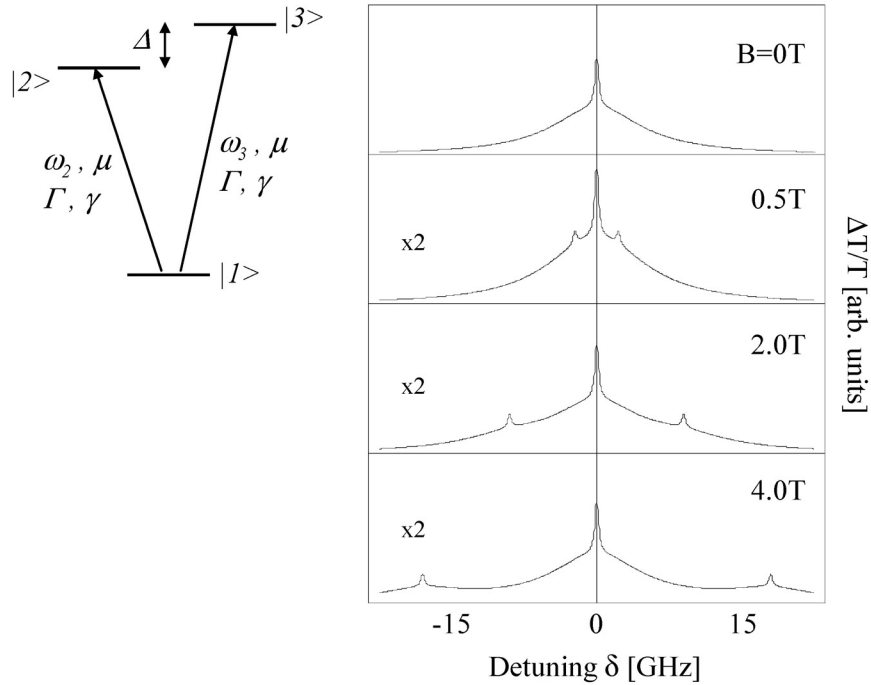
**FIGURE 47.** Left: coherent Raman scattering from localized excitons at various field strengths for co-circularly polarized pump and probe fields ( $T = 8$  K). Right: level diagram and selection rules for the HHI-exciton in the presence of in-plane magnetic fields. Sideband splitting as a function of the field.

Figure 47 shows the coherent Raman scattering response from localized excitons for different strengths of the magnetic field applied in Voigt geometry. Pump and probe are co-circularly

polarized ( $\sigma^+$ ). The coherent Raman scattering response is plotted in terms of the normalized differential transmission ( $\Delta T/T$ ) as a function of the pump-probe detuning. At zero field, the measured spectrum presents essentially the SHB-response from  $\sigma^+$ -excitons as discussed above. Upon application of in-plane magnetic fields, two sidebands emerge symmetrically at positive and negative detuning. The sideband splitting  $\Delta$  increases linearly with increasing field strength. A linear fit reveals a g-factor of  $g = 0.26$ , which is in very good agreement with previously measured electron g-factors in GaAs-quantum wells with  $L_z = 13$  nm well-width and Al-concentration of 30% in the barriers<sup>55</sup>. The observed sidebands are thus coherent Raman resonances arising from the electron spin coherence. The sidebands exhibit similar linewidths as the coherent contribution at zero detuning inferring that dephasing of the electron spin coherence is lifetime limited. The broadening of the sidebands with increasing field, and in particular the different splitting for the respective Raman sideband at positive and negative detuning observed for  $B = 4$  T indicates effects of inhomogeneous broadening of the electron g-factor.

As shown in the level diagram in Figure 47, both CB electron spin states are optically coupled to a common VB state for circular polarization of the optical fields in a QW subject to in-plane magnetic fields. For a chosen polarization e.g.  $\sigma^+$ , the HH1-exciton level structure reduces thus effectively to a three-level V-type system. Figure 48 presents numerical solutions of the OBE for an inhomogeneously broadened ensemble of independent V-type systems. The level structure and the relevant physical parameters used in the calculation are also shown. Inhomogeneous broadening of localized excitons results e.g. from size variations of the islands associated with the interfacial steps. Numerical results are obtained by spectrally integrating the expression for the third order response ( $\rho_{12}^{(3)} + \rho_{13}^{(3)}$ ) presented in Chapter V (Eq.(5.4)) over  $\omega = (\omega_2 + \omega_3)/2$  (the electron g-factor has been assumed to be constant over the inhomogeneous profile and the

inhomogeneous linewidth is taken to be larger than the Zeeman splitting for the field strengths considered here). It is further assumed that both dipole transitions are identical ( $\Gamma_1 = \Gamma_2 = \Gamma$ ,  $\gamma_1 = \gamma_2 = \gamma$  and  $\mu_1 = \mu_2 = \mu$ ). Population relaxation and dipole dephasing rates used in the calculation were taken from the spectra obtained for the zero-field case and  $T = 5$  K. We further set  $\gamma_s = \Gamma$  for lifetime limited electron spin coherence as inferred from the measurement. The numerical calculation reproduces all the features observed in the experiment, demonstrating that the V-type atom-like energy level structure provides a suitable model to describe the nonlinear optical response from electron spin coherence associated with localized excitons.



**FIGURE 48.** Third order numerical solution of the OBE for an inhomogeneously broadened system of V-type three-level systems. Relevant parameters,  $\gamma$ ,  $\Gamma$ , and  $g_e$  are taken from experiment.

Figure 49 shows the polarization dependence of the coherent Raman scattering response at  $B = 0$ , 2 and 4 T. The series of spectra reveal the selection rules for optical excitation of the electron spin coherence in coherent Raman scattering. Note that coherent Raman sidebands are observed for cross-linear and co-circular polarization only. The co-circular configuration has been discussed above. For a discussion of the cross-circular case note that at zero field and in a single-particle picture (i.e. correlations between  $\sigma^+$  and  $\sigma^-$  - excitons are absent), the HH1-exciton consists in essence of two independent two-level systems, which can be separately addressed with  $\sigma^+/\sigma^-$  polarized optical fields. On these grounds, we do not expect a SHB-response for cross-circular pump-probe configuration and this is in fact what we observe in the corresponding spectrum for  $B = 0$  T and  $\sigma^+/\sigma^-$  polarized optical fields. In contrast, a broad pedestal emerges in  $\sigma^+/\sigma^-$  configuration at finite fields. The linewidth of the pedestal increases with increasing fields. To understand the emergence of the pedestal, consider the appropriate energy level diagram shown in Figure 49 for circular polarized fields. Keeping in mind that Zeeman splittings are smaller than or comparable with the homogeneous linewidth for the field strengths applied here, the energy level structure in combination with the selection rules shows that three spectral holes can arise, each centered around  $\delta = -\Delta$ , 0, and  $+\Delta$  in the cross-circular case. The observed pedestal is the sum of these spectral holes. In addition to homogeneous broadening, the linewidth of the pedestal is thus determined by the Zeeman splitting, which explains the increase of the broad pedestal with increasing field strength. Note that this type of SHB is different from the SHB associated with a two-level effect as pump and probe address two different transitions. A similar argument applies for the co-circular case for which the spectral holes at  $\delta = -\Delta$ , and  $+\Delta$  arise from depletion of the relevant VB-state.

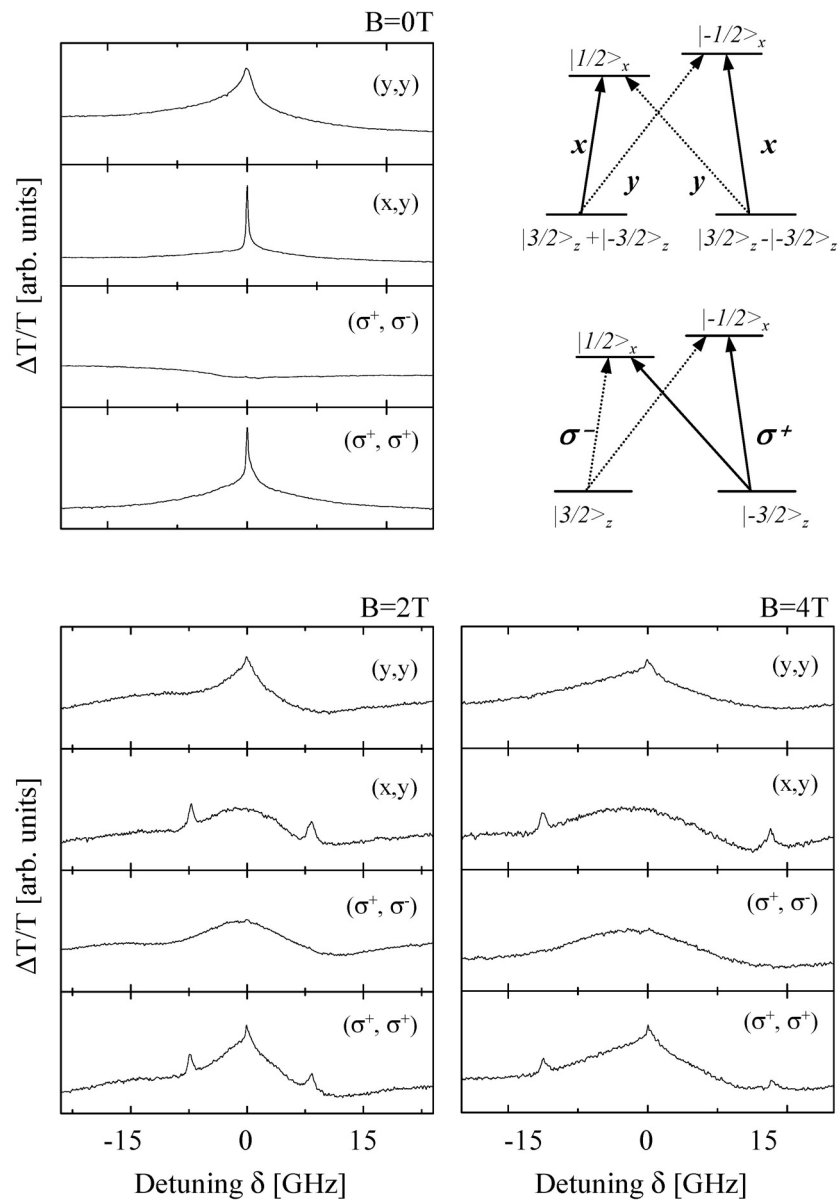


*FIGURE 49. Polarization dependence of the coherent Raman scattering response at  $B = 0, 2,$  and  $4 T$ . Appropriate level diagrams are shown to explain the selection rules.*

In order to understand the observations made for co-and cross- linear pump-probe configuration, an appropriate basis transformation is carried out for the VB-states. The resulting level structure along with the selection rules is shown Figure 49. For co-linear configuration, i.e. (y y), only two-

level effects are involved and signatures of electron spin coherence are absent. For cross-linear configuration, the four-level system represents essentially two three-level systems. In contrast to the co-circular case, however, in which both pump and probe can couple to both transitions within the three-level system, pump and probe can not couple to the same transition here. This explains why coherent Raman sidebands from the electron spin coherence are generated in cross-linear configuration, while the coherent signal associated with two-level effects (population grating) is absent. Again, two spectral holes at  $\delta = -\Delta$ , and  $+\Delta$  can also be induced via depletion of the VB-state and a broad pedestal is in fact observed in the cross-linear case similar to the one observed for cross-circular polarization. Note that the same level scheme applies in the limit of vanishing fields. The coherent resonance observed at  $B = 0$  T for cross-linear configuration arises thus from electron spin coherence and not population pulsation.

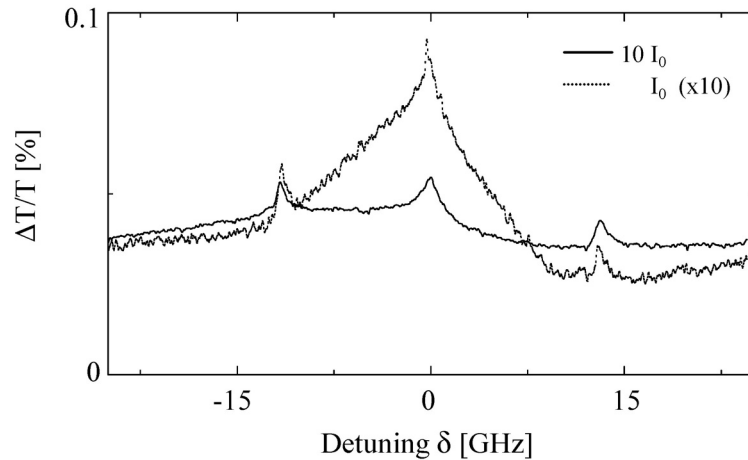


*FIGURE 50. Effects of excitation level on coherent Raman scattering*

The successful observation of coherent Raman resonances from electron spin coherence demonstrates our ability to generate a reduction in the absorption by optically inducing a Raman

coherence. The premise of EIT is thus met. Figure 50 provides the order of magnitude of the induced transparency, which we are able to generate at the Raman sidebands at the given excitation levels. Changes in absorption are on the order of 0.1% and thus weak compared to transparencies achieved in atomic systems. Note however that while increased excitation levels lead to excitation induced dephasing (EID)<sup>98</sup> as inferred from the broadening of the spectral hole, the Raman coherence does not show saturation or power broadening at the excitation levels used.

### Coherent Raman scattering from mobile excitons

The coherent Raman scattering response from mobile excitons is shown in Figure 51 for different polarization configurations and  $B = 1$  T. The spectra shown are representative for the entire range of field strengths investigated ( $B < 6$  T) including the zero field case.

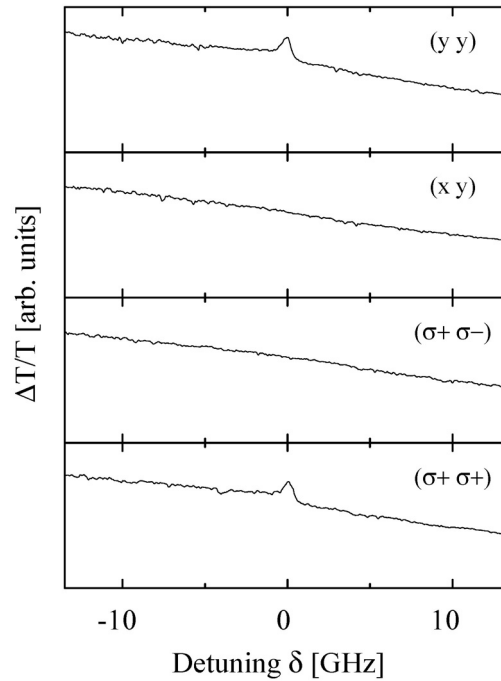


*FIGURE 51. Coherent Raman scattering from mobile excitons for various polarization configurations and  $B = 1$  T ( $T = 10$  K). Signatures of electron spin coherence are absent.*

Note first, that in contrast to localized excitons, a spectral hole is not observed due to the much greater dipole decoherence rate for mobile excitons. Instead, a sloped flat background is revealed, which arises from a blue shift of the HH1-absorption dominating the nonlinear optical response from mobile excitons. Most importantly, signatures of electron spin coherence are absent for all polarization configurations used. The vanishing of the coherent Raman resonance for mobile excitons demonstrates that the mechanisms underlying the nonlinear optical response differ greatly for mobile and localized excitons.

For a more detailed analysis, we incorporate the effects of in-plane magnetic fields into the N-exciton basis in a phenomenological description of mobile excitons. The level diagram shown on the left in Figure 52, depicts once more the relevant single particle states for a description of the HH1-exciton for  $\sigma^+$ -polarized fields. The level diagram on the right shows the HH1-exciton energy level structure in the many-body picture accounting for the presence of in-plane magnetic fields. Since all N-exciton states involve the same valence band state ( $|-3/2\rangle_z$ ), the relevant excitonic states are labelled with respect to the x-projection of the electron spin:  $|g\rangle$  is the ground state,  $|\pm\rangle$  are the one-exciton states with electron spin  $s_x = \pm 1/2$ , and  $|+-\rangle$  is the two-exciton state featuring opposite electron spins. In the many-particle picture, the electron spin coherence corresponds to a coherent superposition of states  $|+\rangle$  and  $|-\rangle$  and is thus associated with the density matrix element  $\rho_{+-}$ . Using  $|a\rangle$  to denote the two-exciton state, the relevant density matrix elements contributing to the nonlinear optical response are  $\rho_{g-}$ ,  $\rho_{+a}$ ,  $\rho_{g+}$ , and  $\rho_{-a}$ . Pairing up the density matrix elements according to  $(\rho_{g-}, \rho_{+a})$  and  $(\rho_{g+}, \rho_{-a})$  defines two optical pathways involving transitions ( $|g\rangle - |-\rangle$  and  $|+\rangle - |a\rangle$ ) and ( $|g\rangle - |+\rangle$  and  $|-\rangle - |a\rangle$ ) respectively.

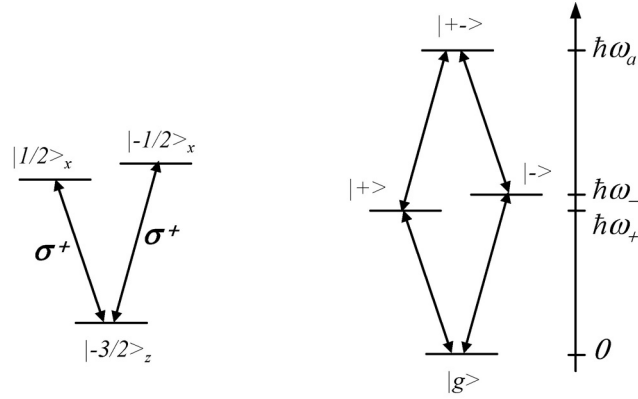


**FIGURE 52.** Energy-level structure of the HHI-exciton in Voigt geometry. Left/right: single- / many-particle picture.

It can be shown quite generally that contributions from the electron spin coherence cancel each other to third order in the nonlinear optical response in a level scheme as shown on the right in Figure 52. To illustrate this, we write down the differential equations for  $\rho_{g^-}$  and  $\rho_{+a}$  as obtained from the Liouville equation applied to the N-exciton level scheme. Note that source terms other than the one associated with the Raman coherence (e.g. such as the inversion of the relevant transition) are not included in the following equations:

$$\begin{aligned} \partial_t \rho_{g^-}^{(3)} &= i\omega_- \rho_{g^-}^{(3)} + i \frac{\mu_{g^+} E}{\hbar} \rho_{+^-}^{(2)} + (\dots) \\ \partial_t \rho_{+a}^{(3)} &= i(\omega_a - \omega_+) \rho_{+a}^{(3)} - i \frac{\mu_{-a} E}{\hbar} \rho_{+^-}^{(2)} + (\dots) \end{aligned} \quad (8.1)$$

The key to an understanding of the coherent Raman scattering response from mobile excitons is hidden in the sign with which the contribution from the electron spin coherence enters the expression for  $\rho_{g^-}$  and  $\rho_{+a}$  respectively. As the sign is opposite for the contribution in the optical pathway associated with ( $|g\rangle - |- \rangle$  and  $|+\rangle - |a\rangle$ ) respectively, effects of the electron spin coherence cancel. The same statement holds for the optical pathway involving ( $|g\rangle - |+\rangle$  and  $|- \rangle -$

$|a\rangle$ ). Exact cancellation takes place, if the two transitions in each pair are identical, which occurs for a non-interacting excitonic system. Although electron spin coherence is induced, effects thereof are absent in the third order nonlinear optical response due to cancellation of the contribution arising from the electron spin coherence to the third order nonlinear optical response.

### Summary

The coherent Raman scattering study on electron spin coherence in GaAs quantum wells reveals fundamentally different behaviours for localized and mobile excitons. While coherent Raman resonances arising from electron spin coherence are revealed for localized excitons, similar signatures of electron spin coherence are absent in the nonlinear optical response from mobile excitons. We gain insight into the experimentally observed phenomena by applying the OBE to appropriate N-exciton level schemes, which account for the nonlinear optical mechanisms, that are operative for localized and mobile excitons respectively. The absence of coherent Raman resonances for mobile excitons in particular is understood by including many-body effects in an energy level diagram based on N-exciton states. It can be shown that although optically created, effects of electron spin coherence are not observed in the third order nonlinear optical response, due to a cancellation of the Raman coherence term involved in the different optical pathways present in the N-exciton level scheme. Note that signatures of electron spin coherence remain absent even if the pump or probe intensity were increased beyond the  $\chi^{(3)}$ -regime. More insight into a power dependence will be gained from the time-resolved measurements. The model based on N-exciton eigenstates does also apply to localized excitons. We argue that for localized excitons, the two-exciton state  $|+-\rangle$  is no longer accessible due to strong on-site Coulomb repulsion between the holes (Pauli exclusion). Thus, only the ground state and the 1-exciton states are relevant in a description of localized excitons. The energy level diagram based on N-exciton

eigen-states reduces thus effectively to a V-type system in a description of localized excitons. This is why good agreement could be obtained between the coherent Raman spectra obtained from localized excitons and numerical results obtained by applying the OBE to a V-type system. In accordance with the observations made for mobile excitons, note that the Raman sidebands observed for excitons below the line center disappear for  $T > 15$  K as excitons become delocalized at these temperatures.

## CHAPTER IX

QUANTUM BEATS FROM FROM ELECTRON SPIN COHERENCE  
IN GaAs-QUANTUM WELLS

The results of our time-domain study on electron spin coherence in GaAs-QWs are presented. Experiments were carried out on samples QW1 and QW2. Both samples reveal the same characteristics. The TI- differential transmission was measured at  $T = 10$  K and is plotted on a linear scale throughout this chapter. To separate contributions from mobile and localized excitons we used the external pulse shaper to narrow the bandwidth of the optical pulses from a mode-locked Ti:sapphire laser ( $\sim 120$  fs pulses at 82 MHz repetition rate). The resulting optical pulses are nearly transform-limited with a bandwidth of 0.35 nm and a pulse duration around 4 ps. The center wavelength of the filtered spectrum was set by selecting different regions of the original laser spectrum.

Quantum beats from localized excitons

Figure 53 shows the TI- normalized differential transmission from sample QW1 as a function of the pump-probe delay for  $B = 0$  and 2 T. The laser spectrum is set below the HH1-absorption as shown in the inset. Thus, localized excitons are predominantly excited in the measurement. Pump and probe fields are co-circularly polarized ( $\sigma^+$ ). In the absence of magnetic fields, the pump-probe response exhibits an initial fast decay followed by a long-lived component. The contributions are respectively associated with coherent and incoherent relaxation processes. As opposed to SHB, dephasing / energy relaxation processes manifest in the coherent / incoherent part of the nonlinear optical response.

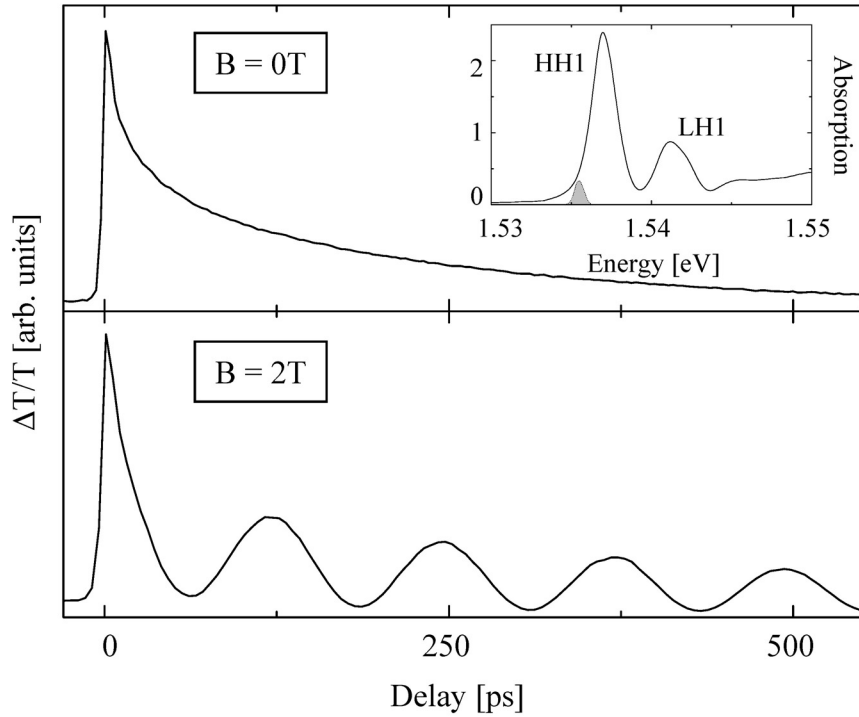


*FIGURE 53.* Time-integrated normalized differential transmission from sample QW1 for  $B = 0$  T and 2 T. The laser spectrum is set below the HH1-exciton resonance, i.e. localized excitons are predominantly excited.  $I_{\text{pump}} = 10 I_{\text{probe}} = 8$  W/cm<sup>2</sup>.

Upon application of in-plane magnetic fields we observe pronounced long-lived oscillations as shown for  $B = 2$  T in Figure 53. Field-dependent measurements show that the oscillation period scales linearly with the magnetic field. We reveal a g-factor of  $|g_e| = 0.26$  in good agreement with the electron g-factor obtained from the sideband splitting in coherent Raman scattering. We assign thus the observed oscillations to absorption quantum beats originating from the electron spin coherence.

In Figure 54, we show the results of a probe- and pump- intensity dependent study of the TI-pump-probe response from localized excitons. At low intensities, the overall differential transmission, and in particular the amplitude of the quantum beats, which is shown in the

respective insets, scales linearly with the pump intensity and is nearly independent of the probe intensity. Note that in the  $\chi^{(3)}$ -regime, the differential transmission scales linearly with the pump and the probe intensity. Therefore, the *normalized* differential transmission increases linearly with the pump intensity but is independent of the probe intensity. The probe/pump intensity dependence shows therefore that quantum beats associated with electron spin coherence from localized excitons are observed within a third order nonlinear optical process. Indications of saturation appear for excitation levels exceeding  $\sim 1 \text{ W/cm}^2$  and are observed for both, the pump and the probe intensity dependence.

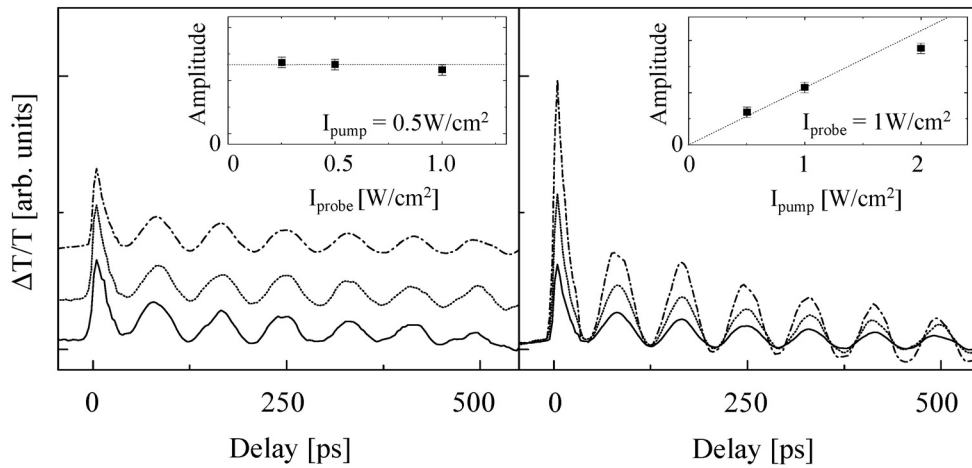


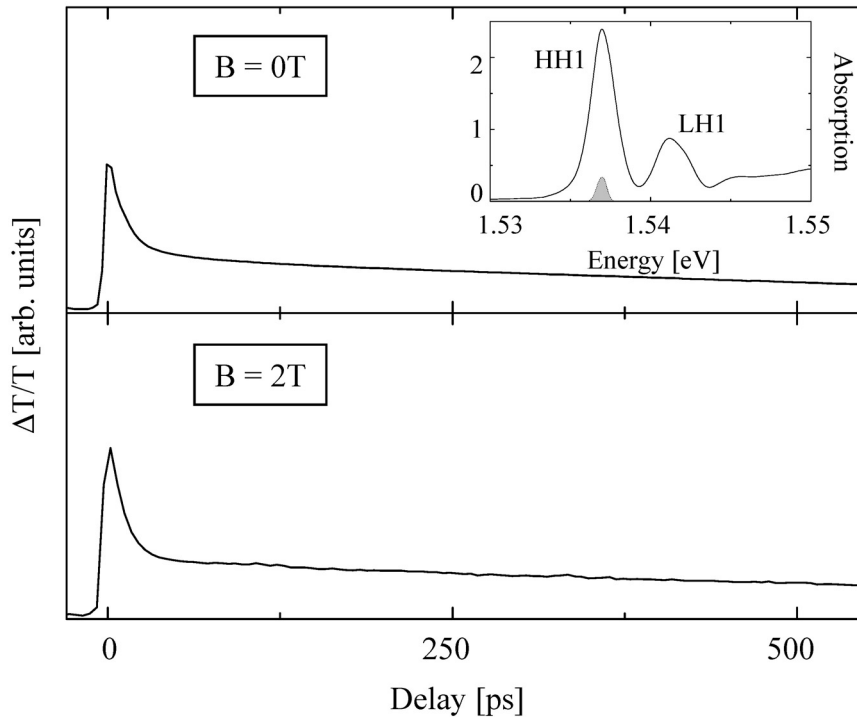
**FIGURE 54.** Left: probe intensity dependence:  $I_{probe} = 0.25, 0.5, 1 \text{ W/cm}^2$ ,  $I_{pump} = 0.5 \text{ W/cm}^2$ . The baselines are shifted for display clarity. Right: pump intensity dependence:  $I_{pump} = 0.5, 1, 2 \text{ W/cm}^2$ ,  $I_{probe} = 1 \text{ W/cm}^2$ . Solid, dotted and dashed curves correspond to increasing intensities for either pump or probe.  $B = 3 \text{ T}$ .

The measurements presented here provide first time evidence of electron spin coherence in TI-differential transmission measurements. Note that we also observed quantum beats from *exciton* spin coherence (results are not presented here), if magnetic fields were applied along the growth direction (Faraday geometry) confirming the results of a previous study<sup>99</sup>. Interestingly, this previous study did not show indication of quantum beats associated with electron spin coherence

if magnetic fields were applied in the plane of the quantum wells used. Note that in these measurements, no particular attention was paid to the spectral position/bandwidth of the input spectrum of the laser pulses employed. In the next section, we reveal how quantum beats from electron spin coherence do ‘mysteriously’ disappear - and - re-appear.

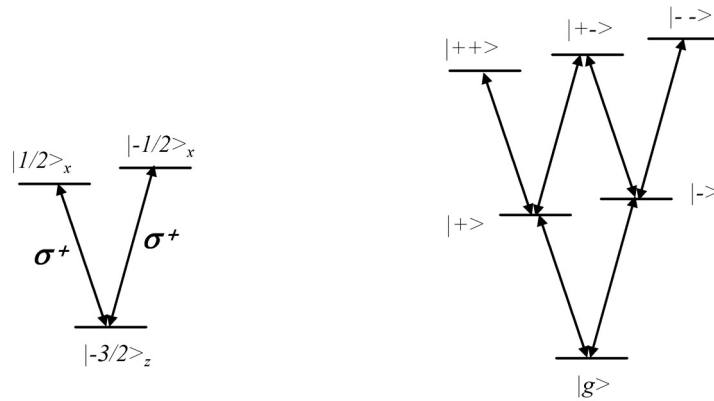
### Quantum beats from mobile excitons

Figure 55 shows the TI-differential transmission as a function of the pump-probe delay for co-circularly polarized fields and with the spectrum centered at the HH1-exciton to predominantly excite mobile excitons. At zero-field the trace reveals a fast initial decay followed by a long lived component, the latter being due to relaxation of a quasithermal exciton population<sup>100</sup>.



**FIGURE 55.** Time-integrated normalized differential transmission from sample QW1 for  $B = 0T$  and  $2T$ . The laser spectrum is centered at the HH1-exciton resonance, i.e. mobile excitons are predominantly excited.  $I_{pump} = 10 I_{probe} = 8 W/cm^2$ .

Upon application of magnetic fields in Voigt geometry, we observe to our surprise, that in contrast to localized excitons, coherent oscillations originating from the electron spin coherence are absent. Just as in coherent Raman scattering, signatures of electron spin coherence vanish thus in the third-order nonlinear optical response from mobile excitons in the TI-differential transmission measurement. Despite this similarity, note that there is a fundamental difference between the time- and the frequency- domain measurement with regard to the nonlinear optical mechanism generating the electron spin coherence. Whereas joint action of pump and probe is involved in optically creating the electron spin coherence in coherent Raman scattering as discussed in Chapter VIII, the electron spin coherence is created by the pump pulse alone in the time-domain measurement. This is possible as the selection rules for exciting the HH1-exciton are appropriately modified in the presence of in-plane magnetic fields. The relevant single-particle states for the HH1-exciton and  $\sigma^+$ -polarized fields are shown one more time in Figure 56 (left).



*FIGURE 56. Level structure of the HH1-exciton in Voigt geometry also showing appropriate selection rules for e.g.  $\sigma^+$ -polarized light. Left: single-particle picture. Right: many-particle picture including one-exciton and two-exciton states.*

Both transitions are addressed for  $\sigma^+$ -polarized light. Note that for the magnetic field strengths considered, the bandwidth of the laser spectrum exceeds the Zeeman splitting of the electron spin states. A single  $\sigma^+$ -polarized pulse can thus induce the electron spin coherence. Once optically injected by the pump field, the evolution of the electron spin coherence is monitored by the probe pulse. In order to understand the vanishing of the electron spin coherence in the third order nonlinear optical response from mobile excitons, we invoke the N-exciton level diagram as shown on the right in Figure 56. To third order in the nonlinear optical response only the one-exciton states and the two-exciton state  $|+ \rightarrow\rangle$ , which we denote  $|a\rangle$ , are involved. Applying the OBE to this level scheme in a phenomenological density matrix formalism we obtain:

$$\begin{aligned}\partial_t \rho_{g^-}^{(3)} &= i\omega_- \rho_{g^-}^{(3)} + i \frac{\mu_{g^+} E_{probe}}{\hbar} \rho_{+-}^{(2)} + (\dots) \\ \partial_t \rho_{+a}^{(3)} &= i(\omega_a - \omega_+) \rho_{+a}^{(3)} - i \frac{\mu_{-a} E_{probe}}{\hbar} \rho_{+-}^{(2)} + (\dots)\end{aligned}\tag{9.1}$$

In contrast to Eq.(8.1), only the probe field enters the expression for the electric field due to the time-ordering in the time-domain measurement. Nevertheless, as discussed in Chapter VIII, the contribution from the electron spin coherence to the third order coherences associated with transitions ( $|g\rangle - |-\rangle$ ) and ( $|+\rangle - |a\rangle$ ) cancels in the overall nonlinear optical response. Although generated, contributions from the electron spin coherence cancel in the third order nonlinear optical response associated with  $\rho_{g^-}^{(3)}$  and  $\rho_{+a}^{(3)}$  (a similar argument holds for transitions ( $|g\rangle - |+\rangle$ ) and ( $|-\rangle - |a\rangle$ )). Exact cancellation occurs in the limit that the transitions between  $|g\rangle$  and the one-exciton states are identical with the respective transitions between the one-exciton states and the two-exciton state  $|+ \rightarrow\rangle$ , i.e. in the non-interacting boson limit. The particular behaviour of the electron spin coherence associated with mobile excitons is a result of weak underlying exciton-exciton interactions, which allow for the creation of the two-exciton state  $|+ \rightarrow\rangle$ .

In contrast, localized excitons present a prototype example for which the one-exciton states are strongly interacting. Note that the same hole state is involved in the creation of the two-exciton state  $|+ -\rangle$ . As a result of Pauli exclusion, strong on-site repulsion between holes prevents the formation of state  $|+ -\rangle$  for localized excitons. The N-exciton level diagram shown in Figure 56 collapses thus to a tree-level system (including the vacuum and the one-exciton states only) in a description of localized excitons. As discussed in Chapter VIII, the atom-like characteristics observed for localized excitons are expected based on this level scheme.

A probe- and pump- intensity dependence of the TI-pump-probe response from mobile excitons is shown in Figure 57. To our surprise we observe that coherent oscillations emerge as we increase the probe intensity. The measured beat period agrees well with the one observed for localized excitons confirming that the coherent oscillations are due to electron spin coherence. The amplitude of the quantum beats rises linearly with the probe intensity and becomes sub-linear at higher probe intensities. A linear dependence of the quantum beat amplitude on the probe intensity in the normalized differential transmission means that the corresponding nonlinear polarization scales with the third order of the probe field. Despite the striking difference in the probe intensity dependence, the quantum beat amplitude still scales linearly with the pump intensity. As for localized excitons, the electron spin coherence forms thus in the second order of the pump field.

The observed probe intensity dependence is highly unusual. In a transient pump-probe measurement as carried out here, the optical nonlinearity is typically induced by the pump and not the probe. For most nonlinear optical processes, increasing the probe intensity leads to saturation of the normalized differential transmission. Indications thereof are indeed present in the probe-intensity dependence shown in Figure 57. While the amplitude of the emerging quantum beats

rises with increasing probe intensity as discussed, note that signal strength of the overall normalized differential transmission decreases (i.e. the initial coherent contribution as well as the long-lived component). Our observations are confirmed in similar measurements on sample QW2, which consists of a single-QW. Confirmation of our results in a single-QW, demonstrates that the unusual probe intensity dependence shown in Figure 57 is not due to propagation effects or strong absorption at the exciton line center in the multiple-QW sample QW1.

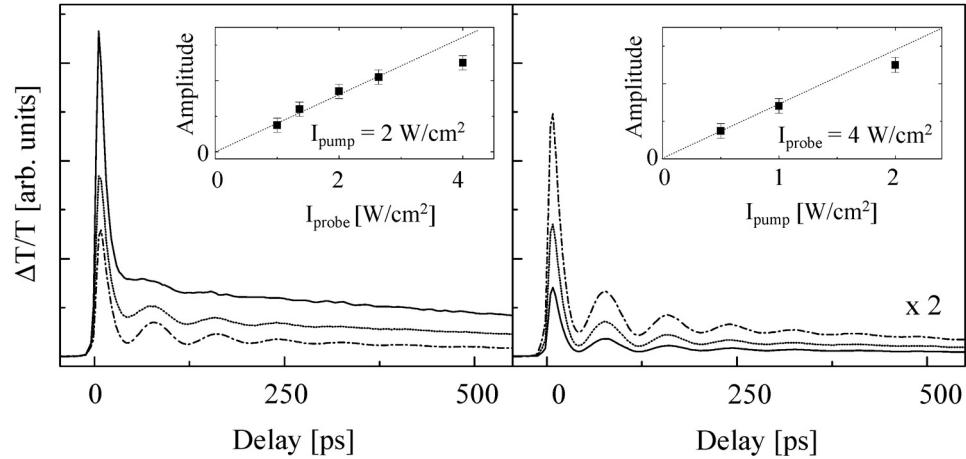


**FIGURE 57.** Left: probe intensity dependence:  $I_{probe} = 1, 2, 4 \text{ W/cm}^2$ ,  $I_{pump} = 2 \text{ W/cm}^2$ . Right: pump intensity dependence:  $I_{pump} = 0.5, 1, 2 \text{ W/cm}^2$ ,  $I_{probe} = 4 \text{ W/cm}^2$ . Solid, dotted and dashed curves correspond to increasing intensities for either pump or probe. The probe intensity dependence reveals a highly unusual  $\chi^{(5)}$ -nonlinearity.

To understand the emergence of quantum beats from electron spin coherence associated with mobile excitons in a fifth-order process higher-order correlations need to be included. An order-by-order perturbation analysis shows that the two-exciton states  $|+ +\rangle$  and  $|- -\rangle$ , which are included in the many-body HH1-exciton level diagram in Figure 56, contribute to a nonlinear optical polarization to third order in the probe field and thus give rise to a  $\chi^{(5)}$ -nonlinearity. It is

the strong exciton-exciton interaction inherent in these two-exciton states, which leads to the emergence of quantum beats in  $\chi^{(5)}$ -nonlinearity.

### Polarization dependence

Figure 58 shows the results of a polarization dependent study of the TI-pump-probe response from localized and mobile excitons in sample QW2. Traces were measured in a  $\chi^{(3)} / \chi^{(5)}$ -regime for localized/mobile excitons such that quantum beats from electron spin coherence are observed. For both exciton species, quantum beats are observed for co- and cross-circular polarization configuration. The oscillations in the cross-circular case exhibit a  $\pi$ -phase shift with respect to the oscillations in co-circular configuration. Quantum beats are absent for co- and cross-linear polarization configuration. The observed polarization dependence in the time-domain pump-probe measurements is thus distinctively different from that in coherent Raman scattering.

The polarization dependence does reflect the differences of the underlying nonlinear optical mechanism which is operative in the respective measurement. Note again, that the electron spin coherence is optically injected by the pump field alone in the time-domain measurement. Considering e.g. the single-particle level diagram for linearly polarized fields as shown in Figure 58, note that the electron spin coherence can not be induced by a single linearly polarized pump pulse, since the two electron spin states are respectively coupled to two different hole states. Quantum beats are thus absent for linear polarization of the pump. In contrast, the electron spin coherence is optically injected using circularly polarized pump fields.

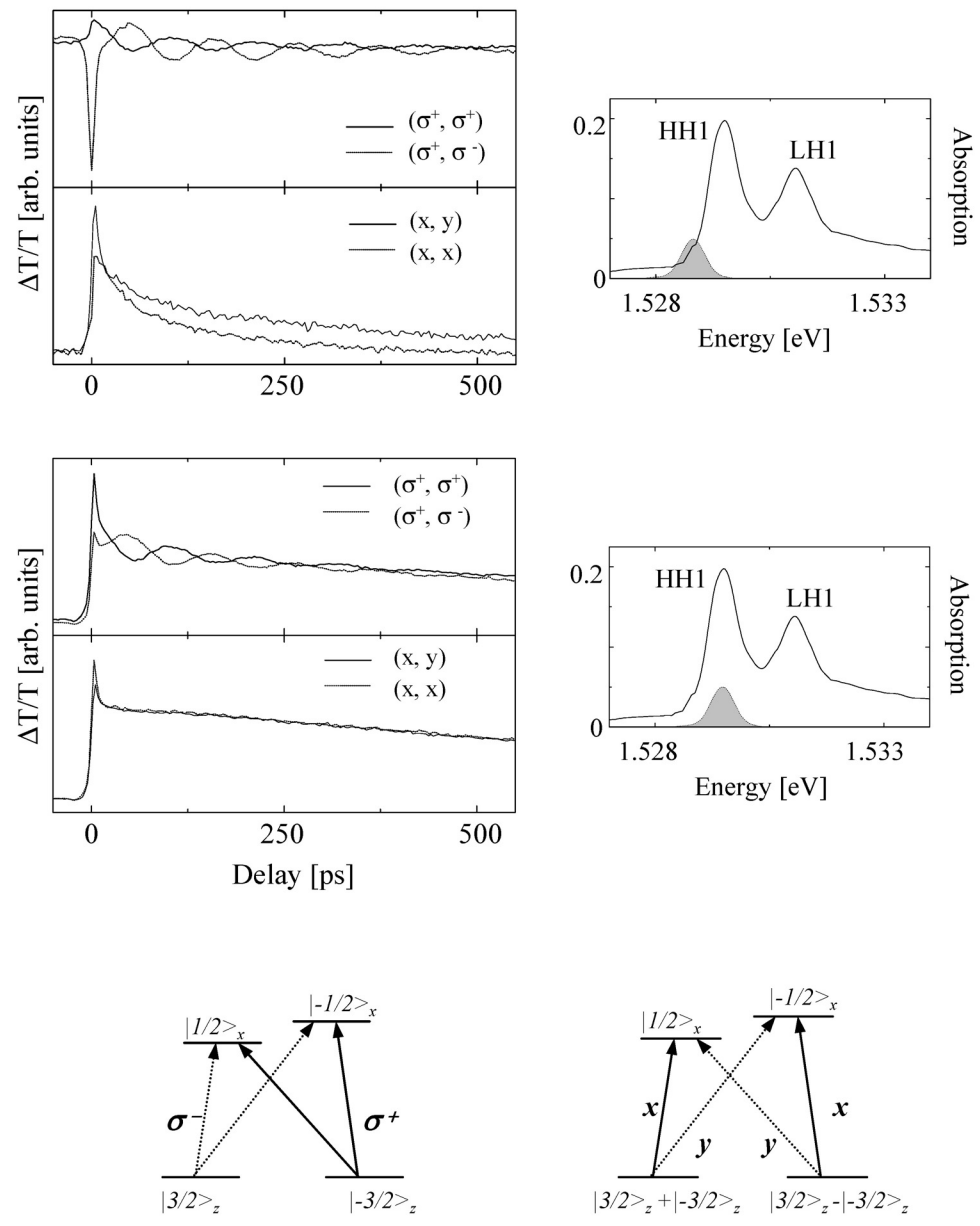


**FIGURE 58.** Polarization dependence carried out on sample QW2. Top: localized excitons. Center: mobile excitons.  $I_{pump} = 0.5, 1, 2 \text{ W/cm}^2$ ,  $I_{probe} = 4 \text{ W/cm}^2$ . Bottom: the relevant single-particle level diagrams for circularly and linearly polarized fields.

### Summary

The time-domain pump-probe measurements confirm the results obtained in coherent Raman scattering in a sense that signatures of electron spin coherence are observed for localized but not for mobile excitons within a  $\chi^{(3)}$ -regime. The results of frequency- and time- domain experiments are understood following a phenomenological approach, in which excitonic nonlinearities are modelled by applying the OBE to an energy level diagram based on N-exciton states. For localized excitons, strong on-site repulsion prevents formation of higher-order correlations. Only the vacuum state and one-exciton states are thus of importance in a description of localized excitons. Consequently, localized excitons behave essentially like atomic systems. In contrast, the weak exciton-exciton interactions underlying extended optical excitations such as mobile excitons allow the formation of higher-order correlations. The vanishing of the electron spin coherence in the third order nonlinear optical response results from cancellation of the Raman coherence term in the different optical pathways associated with one-exciton and two-exciton coherences. Signatures of electron spin coherence associated with mobile excitons, emerge in an unusual  $\chi^{(5)}$ -nonlinearity in the TI- differential transmission experiment. Our observations can be explained by invoking two-exciton states, in which the electron spin has the same orientation. We argue that the strong exciton-exciton interactions inherent in these states, generates quantum beats from electron spin coherence in a fifth-order nonlinear optical process.

## CHAPTER X

## SUMMARY AND FUTURE WORK

Summary

Spurred by observations of remarkably long dipole dephasing times in QD-systems, dephasing in semiconductors QDs remains to this point an area of intense research. Most of the breakthroughs made in recent years are related to III-V based QD-systems. In contrast, previous studies on dipole dephasing in II-VI based QD-systems have provided controversial results, mainly due to varying quality of the samples employed as growth of II-VI based QDs is still in its earlier stages, but also due to deficiencies in the measurement techniques employed. Previous studies lack in particular the ability to eliminate effects of spectral diffusion, which are masking the intrinsic homogeneous linewidth.

In the first part of this dissertation, we resolve the controversy surrounding dipole dephasing in CdSe-QDs by carefully addressing effects of spectral diffusion in nonlinear optical measurements of the homogeneous linewidth in high-quality chemically and epitaxially grown CdSe-QDs. Having developed a novel technique based on high-resolution frequency-domain SHB, we are able to experimentally suppress effects of spectral diffusion and therefore to measure *intrinsic* dipole dephasing rates. For both QD-systems investigated, effects of electron-phonon interactions manifest in the SHB response in the form of acoustic- and LO- phonon assisted optical transitions. In addition, we observe a pronounced ZPL associated with the zero-phonon-transition. Good qualitative and quantitative agreement is obtained for both QD-systems establishing that the observed behaviours are independent of the particular growth technique employed and thus of general nature. For both QD-systems we observe in particular:

- similar coupling strengths underlying interaction with acoustic- and LO- phonons
- dipole dephasing times of the ZPL around 200ps
- presence of spectral diffusion
- long ( $\mu$ s)-lifetime of the SHB response indicating the presence of dark states
- correlation between relevant diffusion time scales and the SHB-lifetime, establishing a connection between carrier trapping and spectral diffusion.

Similar dipole dephasing times are measured in both QD-systems, despite effects of acoustic phonon confinement in CdSe-nanocrystals. In addition, a size dependent study on CdSe-nanocrystals does not reveal a size-dependence of the ZPL linewidth. We conclude, that neither confinement of acoustic phonons nor the magnitude of the fine structure splitting of the band-edge exciton significantly affect dipole dephasing of the bright exciton at absolute zero temperature. We argue instead that dipole dephasing is limited by spin relaxation from the bright exciton to the intrinsic dark exciton, a mechanism, which is still operative at absolute zero temperature. This mechanism is inherent of band-edge excitons in CdSe-QDs, in which the dark exciton constitutes the lowest energy state. Note, that this mechanism is absent e.g. in interface fluctuation GaAs-QDs for which the bright exciton constitutes the lowest energy state within the band-edge exciton manifold<sup>71,101</sup>. For increasing temperature we include thermal activation to higher lying states as a likely additional dephasing channel.

Further insight was gained into the role of electron-phonon interactions on dipole dephasing in QDs by theoretical calculations of the electron-acoustic phonon interaction in CdSe-QDs. It is revealed that coupling to acoustic phonons is significantly enhanced in CdSe- over InGaAs- QDs. Note that despite this enhancement, dephasing of the ZPL in CdSe-QDs is comparable to that in InGaAs-QDs.

In the second part of the dissertation we exploited the electron spin coherence as a vehicle to explore coherent optical phenomena characteristic of many-body correlations in semiconductors. In a comparison between localized and mobile excitons in GaAs-QWs, we are able to contrast atom-like behaviours with those characteristic of extended optical excitations in semiconductors. A comparison between the frequency- and time- domain studies further shows that different nonlinear mechanisms generate the electron spin coherence in the respective measurement. The reader is referred to the respective summaries in Chapter VIII and IX for more details. Note that the observations made were facilitated by the remarkable robustness of the electron spin coherence. In this regard, electron spin coherence opens up a new domain for exploring and understanding the interplay between quantum coherences and many-body interactions in semiconductors. While providing fundamental insight into the role of many-body correlations on excitonic nonlinearities, the studies presented provide novel means to optically manipulate the electron spin coherence.

#### Future Work

A comparison of dipole decoherence in III-V and II-VI based QDs as carried out here, can potentially elucidate the role of electron-phonon interactions, and should further stimulate theoretical efforts to account for decoherence of the ZPL induced by electron-phonon interactions. Recent theoretical studies have in fact shown broadening of the ZPL as a result of quadratic coupling to phonons, which was included in an extension of the independent boson model<sup>102</sup>. Additional calculations of the spin-flip rate from the bright to the dark exciton could provide further insight into the mechanisms, which set an absolute limit to dipole dephasing in CdSe-QDs.

Despite the remarkably long dephasing times revealed in CdSe-QDs, carrier trapping and related effects thereof such as spectral diffusion can severely compromise the use of this type of QD-system in applications of coherent control. Note that spectral diffusion, although present to different degrees, has been observed in most QDs and is not unique to the QD-systems investigated here. Given the facts, progress needs to be made in two areas. The first one addresses material science related aspects, i.e. improvements in dot-growth. The goal here clearly is to minimize extrinsic effects, which are detrimental to practical applications. Note, that the inherently large surface to volume ratios set a natural limit to these efforts. Alternative paths are thus aimed at circumventing the limitations set by QD-growth. Recently, it has been observed that the radiative decay channels in nanocrystals can be promoted, if nanocrystals are deposited on rough metallic films. It has been shown that radiative decay can compete with non-radiative decay processes in this case, resulting in significant changes in the dynamical optical behaviour such as fluorescence blinking and spectral diffusion<sup>103</sup>.

Our studies on dipole dephasing in CdSe-nanocrystals were initially motivated by the possibility to implement the strong coupling regime of cavity-QED in a composite silica microsphere/CdSe-nanocrystal semiconductor microcavity<sup>104,105</sup>. While strong coupling could indeed be achieved in such a system as demonstrated by our SHB study, note that spectral diffusion processes severely compromise this scheme. Alternatively, future work in Wang Lab aims at exploiting electron spin coherence in nanocrystals in cavity-QED schemes to implement quantum logic gates<sup>106</sup>. Generally, given the successful demonstrations of EIT in recent years, a trend is currently solidifying aimed at exploiting non-radiative coherences for coherent optical control using macroscopic systems. Applications thereof are two-fold. First, storage of *classical* light pulses using slow-light is of tremendous interest for realizations of the all-optical network. Slow-light

has been successfully demonstrated in atomic systems<sup>107</sup>. Since most photonic devices are based on semiconductor systems, efforts to realize EIT in semiconductors present a necessity if practical applications are ever to result from EIT. The coherent Raman scattering study on localized excitons in GaAs-QWs presents a precursor of future observations of EIT based on electron spin coherence in semiconductors. The experimentally observed transparencies ( $\sim 0.1\%$ ) however, are too small to be exploited for practical applications. To further pursue this approach, future studies in Wang Lab will investigate coherent Raman scattering from QDs.

Photon-photon interactions enabled by EIT are also of great interest in quantum information processing, e.g. for the generation of entangled photon-pairs and for quantum logic operations. Generation of *non-classical* photon pairs has indeed been demonstrated recently using EIT-related nonlinear optical processes<sup>108,109</sup>. Possible applications, such as quantum state memories could enable quantum communication over long distances for quantum networking.

Future experiments will continue to try and harness EIT for classical signal processing in optical networks, and quantum-state manipulation in quantum information. While recent observations capitalize on the long coherence times in atomic vapours, solid-state devices are undoubtedly preferred for practical applications because of their low cost and the possibility of integration with existing technologies. Future research will thus address the possibilities to implement EIT in solid-state systems. The studies on electron spin coherence carried out in this dissertation present another stepping stone on this path, which is expected to see further improvement in material growth and fundamental insight into nonlinear optical phenomena in many-body systems.

## BIBLIOGRAPHY

- <sup>1</sup> C.H. Bennett and D.P. DiVincenzo, *Nature* **404**, 247, (2000).
- <sup>2</sup> D.P. DiVincenzo, *Science* **270**, 255 (1995).
- <sup>3</sup> P. Borri, W. Langbein, S. Schneider, U. Woggon, R.L. Sellin, D. Ouyang, and D. Bimberg, *Phys. Rev. Lett.* **87**, 157401 (2001).
- <sup>4</sup> D. Birkedal, K. Leosson, and J.M. Hvam, *Phys. Rev. Lett.* **87**, 227401 (2001).
- <sup>5</sup> D.D. Awschalom and J.M. Kikkawa, *Phys. Today* **52**, No. 6, 33 (1999).
- <sup>6</sup> F. Bloch, *Phys. Rev.* **70**, 460 (1946).
- <sup>7</sup> L. Allen and J.H. Eberly, *Optical Resonance And Two-Level Atoms*, Dover Publications, Inc., New York, 1987.
- <sup>8</sup> S. Schmitt-Rink, D.A.B. Miller, D.S. Chemla, *Phys. Rev. B* **35**, 8113 (1987).
- <sup>9</sup> S. A. Empedocles, D.J. Norris, and M.G. Bawendi, *Phys. Rev. Lett.* **77**, 3873 (1996).
- <sup>10</sup> K. Takemoto, B.-R. Hyun, and Y. Masumoto, *Solid State Comm.* **114**, 521 (2000).
- <sup>11</sup> A. Hundt, T. Flissikowski, M. Lowisch, M. Rabe, and F. Henneberger, *phys. stat. sol. (b)* **224**, 159 (2001).
- <sup>12</sup> A.P. Heberle, W.W. Rühle, and K. Ploog, *Phys. Rev. Lett.* **72**, 3887 (1994).
- <sup>13</sup> J.M. Kikkawa and D.D. Awschalom, *Phys. Rev. Lett.* **80**, 4313 (1998).
- <sup>14</sup> L.J. Sham, *J. Phys. Cond. Matter* **5**, A51 (1993).
- <sup>15</sup> D.D. Awschalom, D. Loss, N. Samarth, (Eds.), *Semiconductor Spintronics and Quantum Computation*, Springer-Verlag, Berlin Heidelberg New York, 2002.
- <sup>16</sup> S.E. Harris, *Phys. Today* **50**, 36 (1997).
- <sup>17</sup> M.C. Phillips and H. Wang, *Phys. Rev. Lett.* **89**, 186401 (2002).
- <sup>18</sup> M.C. Phillips, H. Wang, I. Rumyantsev, N.H. Kwong, R. Takayama, and R. Binder, *Phys. Rev. Lett.* **91**, 183602 (2003).
- <sup>19</sup> P.C. Ku, C.J. Chang-Hasnain, and S.L. Chuang, *Electron. Lett.* **38**, 1581 (2002).
- <sup>20</sup> P. Palinginis, S. Tavenner, M. Lonergan, H. Wang, *Phys. Rev. B* **67**, R201307 (2003).

- <sup>21</sup> P. Palinginis, H. Wang, S.V. Goupalov, D. Citrin, M. Dobrowolska, and J.K. Furdyna, submitted to Phys. Rev. B.
- <sup>22</sup> P. Palinginis and H. Wang, Appl. Phys. Lett. **78**, 1541, (2000).
- <sup>23</sup> P. Palinginis and H. Wang, submitted to Phys. Rev. B.
- <sup>24</sup> P. Palinginis, H. Wang, Phys. Rev. Lett. **92**, 37402 (2004).
- <sup>25</sup> Th. Oestrich, K. Schoenhammer, and L.J. Sham, Phys. Rev. Lett. **74**, 4698 (1995).
- <sup>26</sup> S. Schmitt-Rink, D.S. Chemla, and D.A.B. Miller, Adv. in Phys. **38**, 89 (1989).
- <sup>27</sup> Al.L Efros, M. Rosen, M. Kuno, M. Nirmal, D.J. Norris, and M. Bawendi, Phys. Rev. B **54**, 4843 (1996)
- <sup>28</sup> J. Puls, M. Rabe, H.-J. Wünsche, and F. Henneberger, Phys. Rev. B **60**, R16303 (1999).
- <sup>29</sup> Y. Masumoto and T. Takagahara, (Eds.), *Semiconductor Quantum Dots, Physics, Spectroscopy and Applications*, Springer-Verlag Berlin Heidelberg New York, 2002.
- <sup>30</sup> Y. Yu and M. Cardona, *Fundamentals of Semiconductors, Physics and Materials Properties*, Springer-Verlag, Berlin Heidelberg New York, 1996.
- <sup>31</sup> J.M. Luttinger, Phys. Rev. **102**, 1030 (1956).
- <sup>32</sup> D.S. Chemla, Helv. Phys. Acta **56**, 607 (1983).
- <sup>33</sup> R.J. Elliot, Phys. Rev. **108**, 1384 (1957).
- <sup>34</sup> D.S. Chemla, J. Shah, Nature **411**, 549 (2001).
- <sup>35</sup> E. Blackwood, M.J. Snelling, R.T. Harley, S.R. Andrews, and C.T.B. Foxon, Phys. Rev. B **50**, 14246 (1994).
- <sup>36</sup> E.L. Ivchenko, phys. stat. sol. (a) **164**, 487 (1997).
- <sup>37</sup> C. Weisbuch, R. Dingle, A.C. Gossard, and W. Wiegmann, Solid State Commun. **38**, 709 (1981).
- <sup>38</sup> Y. Masumoto, S. Shionoya, and H. Kawaguchi, Phys. Rev. B **29**, 2324 (1983).
- <sup>39</sup> A. Ourmazd, D.W. Taylor, J. Cunningham, and C.W. Tu, Phys. Rev. Lett. **62**, 933 (1989).
- <sup>40</sup> J. Hegarty, L. Goldner, and M.D. Sturge, Phys. Rev. B **30**, 7346 (1984).
- <sup>41</sup> J. Hegarty and M.D. Sturge, J. Opt. Soc. Am. B **2**, 1143 (1985).

- <sup>42</sup> H. Wang, D.G. Steel, *Appl. Phys. A* **56**, 512 (1991).
- <sup>43</sup> H. Wang, M. Jiang, and D.G. Steel, *Phys. Rev. Lett.* **65**, 1255 (1990).
- <sup>44</sup> T. Takagahara, *Phys. Rev. B* **32**, 7013 (1985).
- <sup>45</sup> J. Shah, *Ultrafast Spectroscopy of Semiconductors and Semiconductor Nanostructures*, Springer-Verlag, Berlin Heidelberg New York, 1999.
- <sup>46</sup> M. Lindberg, S.W. Koch, *Phys. Rev. B* **38**, 3342 (1988).
- <sup>47</sup> V.M. Axt and A. Stahl, *Z. Phys. B* **93**, 195 and 205 (1994).
- <sup>48</sup> K. Victor, V.M. Axt, G. Bartels, A. Stahl, K. Bott, and P. Thomas, *Z. Phys. B* **99**, 197 (1994).
- <sup>49</sup> Th. Oestreich, K. Schoenhammer, L.J. Sham, *Phys. Rev. Lett.* **74**, 4698 (1994).
- <sup>50</sup> Th. Oestreich, K. Schoenhammer, L.J. Sham, *Phys. Rev. B* **58**, 12920 (1998).
- <sup>51</sup> M. Combescot, R. Combescot, *Phys. Rev. Lett.* **61**, 117 (1988).
- <sup>52</sup> K. Bott, O. Heller, D. Bennhardt, S. T. Cundiff, P. Thomas, E.J. Mayer, G.O Smith, R. Eccleston, J. Kuhl, and K. Ploog, *Phys. Rev. B* **48**, 17418 (1993).
- <sup>53</sup> H. Wang, J. Shah, T.C: Damen, and L.N. Pfeiffer, *Sol. State Comm.* **91**, 869 (1994).
- <sup>54</sup> G. Platero, M. Altarelli, *Phys. Rev. B* **39**, 3758 (1988).
- <sup>55</sup> R.M. Hannak, M. Oestreich, A.P. Heberle, and W.W. Rühle, *Sol. State Comm.* **93**, 313 (1995).
- <sup>56</sup> A. Fasolino, G. Platero, M. Potemski, J.C. Maan, K. Ploog, G. Weimann, *Surf. Sci.* **267**, 509 (1992).
- <sup>57</sup> S.A. Crooker, D.D. Awschalom, J.J. Baumberg, F. Flack, and N. Samarth, *Phys. Rev. B* **56**, 7574 (1997).
- <sup>58</sup> H. Benisty, C.M. Sotomayor-Torres, and C. Weisbuch, *Phys. Rev. B* **44**, 10945 (1991).
- <sup>59</sup> M. Nirmal, D.J. Norris, M. Kuno, M.G. Bawendi, Al. L. Efros, and M. Rosen, *Phys. Rev. Lett.* **75**, 3728 (1995).
- <sup>60</sup> C.H. Henry and K. Nassau, *Phys. Rev. B* **1**, 1628 (1970).
- <sup>61</sup> M.G. Bawendi, P.J. Carroll, W.L. Wilson, and L.E. Brus, *J. Chem. Phys.* **96**, 946 (1992).
- <sup>62</sup> K. Leung, S. Pokrant, K.B. Whaley, *Phys. Rev. B* **57**, 12291 (1998).
- <sup>63</sup> M. Nirmal and L. Brus, *Acc. Chem. Res.* **32**, 407 (1998).

- <sup>64</sup> H. Lamb, Proc. London Math. Soc. **13**, 187 (1882).
- <sup>65</sup> L. Saviot, B. Champagnon, E. Duval, I.A. Kudriavtsev, A.I. Ekimov, J. Non-Cryst. Sol. **197**, 238 (1997).
- <sup>66</sup> E. Roca, C. Trallero-Giner, M. Cardona, Phys. Rev. B **49**, 13704 (1994).
- <sup>67</sup> T. Takagahara, J. Lumin. **70**, 129 (1996).
- <sup>68</sup> K. Huang and A. Rhys, Proc. Roy. Soc. **A204**, 406 (1950).
- <sup>69</sup> C.B. Duke and G.D. Mahan, Phys. Rev. **139**, A1965 (1965).
- <sup>70</sup> B. Krummheuer, V.M. Axt, and T. Kuhn, Phys. Rev. B **65**, 195313 (2002).
- <sup>71</sup> T. Takagahara, Phys. Rev. B **60**, 2638 (1999).
- <sup>72</sup> A. Vagov, V.M. Axt, and T. Kuhn, Phys. Rev. B **66**, 165312 (2002).
- <sup>73</sup> R.W. Schönlein, D.M. Mittelman, J.J. Shiang, A.P. Alivisatos, and C.V. Shank, Phys. Rev. Lett. **70**, 1014 (1993).
- <sup>74</sup> T.D. Krauss and F.W. Wise, Phys. Rev. Lett. **79**, 5102 (1997).
- <sup>75</sup> S.A. Empedocles, R. Neuhauser, K. Shimizu, and M.G. Bawendi, Adv. Mater. **11**, 1243 (1999).
- <sup>76</sup> L. Marsal, L. Besombes, F. Tinjod, K Kheng, A. Wasiela, B. Gilles, J.-L. Rouviere, H. Mariette, J. Appl. Phys. **91**, 4936 (2001).
- <sup>77</sup> H.D. Robinson, B.B. Goldberg, Phys. Rev. B **61**, R5086 (1999).
- <sup>78</sup> K. Leosson, J.R. Jensen, J.M. Hvam, W. Langbein, phys. Stat.sol (b) **221**, 49 (2000).
- <sup>79</sup> V. Türck, S. Rodt, O. Stier, R. Heitz, R. Engelhardt, U.W. Pohl, D. Bimberg, R. Steingrüber, Phys. Rev. B **61**, 9944 (1999).
- <sup>80</sup> S.A. Empedocles, M.G. Bawendi, Science, **278**, 2114 (1997).
- <sup>81</sup> R.G. Neuhauser, K.T. Shimizu, W.K. Woo, S.A. Empedocles, M.G. Bawendi, Phys. Rev. Lett. **85**, 3301 (2000).
- <sup>82</sup> C.B. Murray, D.J. Norris, and M.G. Bawendi, J. Am. Chem. Soc. **115**, 8706 (1993).
- <sup>83</sup> M.A. Hines and P. Guyot-Sionnest, J.Phys. Chem. **100**, 468 (1995).

- <sup>84</sup> B.O. Daboussi, J. Rodriguez-Viejo, F.V. Mikulec, J.R. Heine, H. Mattoussi, R. Ober, K.F. Jensen, and M.G. Bawendi, *J. Phys. Chem.* **101**, 9463 (1997).
- <sup>85</sup> X. Fan, PhD dissertation (2000).
- <sup>86</sup> X. Fan, M.C. Lonergan, Y. Zhang, and H. Wang, *Phys. Rev. B* **64**, 115310 (2001).
- <sup>87</sup> S. Lee, I. Daruka, C.S. Kim, A.-L. Barabasi, J.L. Merz, and J.K. Furdyna, *Phys. Rev. Lett.* **81**, 3479 (1998).
- <sup>88</sup> C.S. Kim, M. Kim, J.K. Furdyna, M. Dobrowolska, S. Lee, H. Rho, L.M. Smith, H.E. Jackson, E.M. James, Y. Xin, and N.D. Browning, *Phys. Rev. Lett.* **85**, 1124 (1999).
- <sup>89</sup> M.D. Levenson, *Introduction to Nonlinear Laser Spectroscopy*, Academic, New York, 1984.
- <sup>90</sup> Murray Sargent III, *Phys. Rep.* **43**, 223 (1978).
- <sup>91</sup> D.G. Steel and S.C. Rand, *Phys. Rev. Lett.* **55**, 2285 (1985).
- <sup>92</sup> D.G. Steel and J.T. Remillard, *Phys. Rev. A* **36**, 4330 (1987).
- <sup>93</sup> S. Nomura and T. Kobayashi, *Phys. Rev. B* **45**, 1305 (1992).
- <sup>94</sup> C.R. Kagan, C.B. Murray, and M.G. Bawendi, *Phys. Rev. B* **54**, 8633 (1996).
- <sup>95</sup> S.A. Empedocles and M.G. Bawendi, *J. Phys. Chem. B* **103**, 1826 (1999).
- <sup>96</sup> S.V. Goupalov, R.A. Suris, P. Lavallard, and D. Citrin, *IEEE J. Sel. Topics Quantum Electron.* **8**, 1009 (2002).
- <sup>97</sup> A. Blacha, H. Presting, and M. Cardona, *phys. stat. Sol. (b)* **126**, 11 (1984).
- <sup>98</sup> H. Wang, K. Ferrio, D.G. Steel, Y.Z. Hu, R. Binder, and S.W. Koch, *Phys. Rev. Lett.* **71**, 1261 (1993).
- <sup>99</sup> S. Bar-Ad and I. Bar-Joseph, *Phys. Rev. Lett.* **66**, 2491 (1991).
- <sup>100</sup> A. Vinattieri, J. Shah, T.C. Damen, D.S. Kim, L.N. Pfeiffer, M.Z. Maialle, and L.J. Sham, *Phys. Rev. B* **50**, 10868 (1994).
- <sup>101</sup> X. Fan, T. Takagahara, J.E. Cunningham, and H. Wang, *Solid State Commun.* **108**, 857 (1998).
- <sup>102</sup> E.A. Muljarov and R. Zimmermann, arXiv:cond-mat/0312510 v1 (2003).
- <sup>103</sup> K.T. Shimizu, W.K. Woo, B.R. Fisher, H.J. Eisler, and M.G. Bawendi, *Phys. Rev. Lett.* **89**, 117401 (2002).

- <sup>104</sup> T.A. Brun and H. Wang, *Phys. Rev. A* **61**, 32307 (2000).
- <sup>105</sup> X. Fan, P. Palinginis, S. Lacey, H. Wang, and M.C. Lonergan, *Optics Lett.* **25**, 1600 (2000).
- <sup>106</sup> A. Imamoglu, D.D. Awschalom, G. Burkard, D.P. Divincenzo, D. Loss, M. Sherwin, and A. Small, *Phys. Rev. Lett.* **83**, 4204 (1999).
- <sup>107</sup> D.F. Phillips, A. Fleischhauer, A. Mair, R.L. Walsworth, and M.D. Lukin, *Phys. Rev. Lett.* **86**, 783 (2001).
- <sup>108</sup> A. Kuzmich, W.P. Bowen, A.D. Boozer, A. Boca, C.W. Chou, L.-M. Duan, and H.J. Kimble, *Nature* **423**, 731 (2003).
- <sup>109</sup> C.H. van der Wal, M.D. Eisaman, A. Andre, R.L. Walsworth, D.F. Phillips, A.S. Zibrov, and M.D. Lukin, *Science* **301**, 196 (2003).